Dressed Coherent States of the Anharmonic Oscillator with Damping

A thesis presented

by

Daphna Genai Enzer

to

The Department of Physics

in partial fulfillment of the requirements

for the degree of

Doctor of Philosophy

in the subject of

Physics

Harvard University

Cambridge, Massachusetts

May 1996

Abstract

The master equation is solved for a driven, one-electron cyclotron oscillator which is anharmonic because of special relativity, and damped via synchrotron radiation to thermal equilibrium with a reservoir. The quantum mechanical dressed states of the anharmonic oscillator which emerge have many interesting properties. They are never completely stable, and loss rates are related to their angular probability distributions in phase-space. Perturbations from equilibrium exhibit partial revivals which give a characteristic spreading time for the distributions. This calculation is subject to experimental verification insofar as one electron in a Penning trap is accurately described. In fact, the damping, drive, and noise parameters which should allow 1 part in 10^9 cyclotron frequency measurements are identified.

To my parents.

For their love and support,

and for passing on to me their thirst for knowledge.

Contents

Acknowledgments

Thanks to my advisor, Gerald Gabrielse, for the guidance, flexibility, and helpful insight he provided at all stages of my graduate study. Thanks also to him for originating 3 of the computer codes utilized in this work. Thanks to my other committee members Jene Golovchenko and Mara Prentiss for all the useful advice they have provided in the years since my oral exam.

Thanks goes to Ching-Hua Tseng for years of training and learning from each other, as we improved detection techniques for single trapped electrons, and constantly searched for the tiny wrench to SMA connectors in the microwave source. Much of this theoretical work arose out of questions and conversations from that period, some of which included Robin Kaiser.

A special thanks to Adam Lupu-Sax, first, for giving me access to 5 times more cpu time than our SparcStation20 provided, and second, for generously sharing his code to evolve classical probability distributions in a vector field.

From my experimental period, I would like to thank Kamal Abdullah, Steve Peil, and Tasha Fairfield, with whom I ventured into the first dilution refrigerator experience of our laboratory, Harvard machinists Louis DeFeo, Richard Anderson, Stan Cotreau, and Dave Osier who put up with my 0.0001" specs on trap electrodes and made many emergency "house calls", and NIST collaborator Fred Walls for extensive telephone advice helping me measure the phase-noise of the microwave source he provided to us. In addition, I have had the pleasure of interacting with others in the group not mentioned elsewhere, in the form of discussion, collaboration, learning, teaching, and lively lunch-time conversation: postdoctoral fellows Luis Orozco, Ben Brown, Wolfgang Quint, and Timothy Roach, and students Joseph Tan, Loren Haarsma, Jesse Wen, Anton Khabbaz, David Hall, Carla Levy, and

Peter Yesley.

I would like to thank Kate Kirby for helpful conversations, and from my earlier days, I thank Ruth Hubbard, my inspirational high-school math teacher. I also thank Marianne Dunne and the Interpreters at the Museum of Science for fun and exciting Saturdays this year and for valuable perspective. I heartily thank all my friends and family for their infinite support, especially Dan and Sherri Garretson, Dan Sodickson, Daniel Savin, and some non-Dan's too: Randi Haakenaasen, Robin Wasserman, Kendra Moulton and Roxane Hope (both from afar, but always nearby in spirit), my parents, my siblings, their spouses, my grandmother, and my wonderful in-laws.

I would like to give special thanks to all those who helped me during my whirlwind thesis writing stage: Paul Janzen for his unrelenting knowledge and advice about Unix, David Phillips for providing a flawless shell within which to write, as well as additional LaTeX advice, Lisa Lapidus, Steve Peil and Ching-Hua Tseng for reading the thesis and providing comments, Jan Ragusa for always knowing Jerry's schedule, always having more pens, finding a graduation ticket for me, and for her cheerful optimism, Christie Moody for more support and another graduation ticket, everyone in the lab for putting up with my desperate requests for the computers, and last but by no means least my husband Dan Reisenfeld for everything imaginable. Dan provided unmeasureable amounts of emotional as well as scientific support: from bringing meals, to helping with re-writes, view-graphs and posters, to providing invaluable scientific insight over the years. Thanks.

List of Figures

Chapter 1

Introduction

1.1 Overview

Anharmonic quantum oscillators are the simplest extensions of the well understood harmonic oscillator and are useful models for nonlinear physical systems. The one-electron cyclotron oscillator is the simplest of damped anharmonic oscillators, its anharmonicity arising from special relativity [1], and its damping arising from synchrotron radiation. Anharmonicity is known to cause collapse, revival, and other interference phenomena for initially localized states [2–9]. In addition, dissipation is known to play an important role in the destruction of quantum coherence and the reproduction of classical behavior [3–5]. The final element needed to complete the physical description of such nonlinear systems is a drive, generally expected to produce stable excitations of a classical anharmonic oscillator.

In this work, the master equation is solved to investigate the quantum stability and revival characteristics of an excited state of the one-electron oscillator when a drive, anharmonicity, and damping to equilibrium with a thermal reservoir are all included. Several unexpected features emerge including partial revivals of an initial

harmonic coherent state in a driven system, and persistent loss from even a large resonant excitation. The degree of instability in the excited state is shown to have a strong dependence on angular spread of the dressed coherent state Q-function, and is qualitatively interpreted in terms of classical phase-space stability diagrams. Many of these unexpected effects are attributed to the uniquely quantum mechanical one-electron cyclotron oscillator property of having large anharmonic shifts relative to damping widths for the lowest energy levels.

This general quantum mechanical system is experimentally realizable as a single trapped electron cyclotron oscillator [1]. Anharmonic shifts introduced by special relativity are tiny compared to the cyclotron frequency but are clearly observed and have a significant impact on precision measurements. Part-per-billion measurements of the cyclotron frequency and the anomaly frequency (equal to the difference between the spin and cyclotron frequencies) are needed for the next generation of electron magnetic moment measurements. Comparisons of the experimentally determined magnetic moment with theory provide the best test of QED. The most recent experiments report a fractional accuracy of 4 parts in 10^9 [10, 11], cavity shifts and damping widths within the hyperbolic Penning trap presenting a major obstacle to improvements. A cylindrically shaped Penning trap cavity, with recently characterized microwave resonances [12–14], should provide a clean environment for magnetic moment measurements improved to 1 ppb or better. We present master equation solutions of the electron cyclotron oscillator to find the damping, drive, and noise parameters necessary for ppb frequency measurements. This should greatly facilitate the experimenters' task by directing the path of investigation through a large parameter-space.

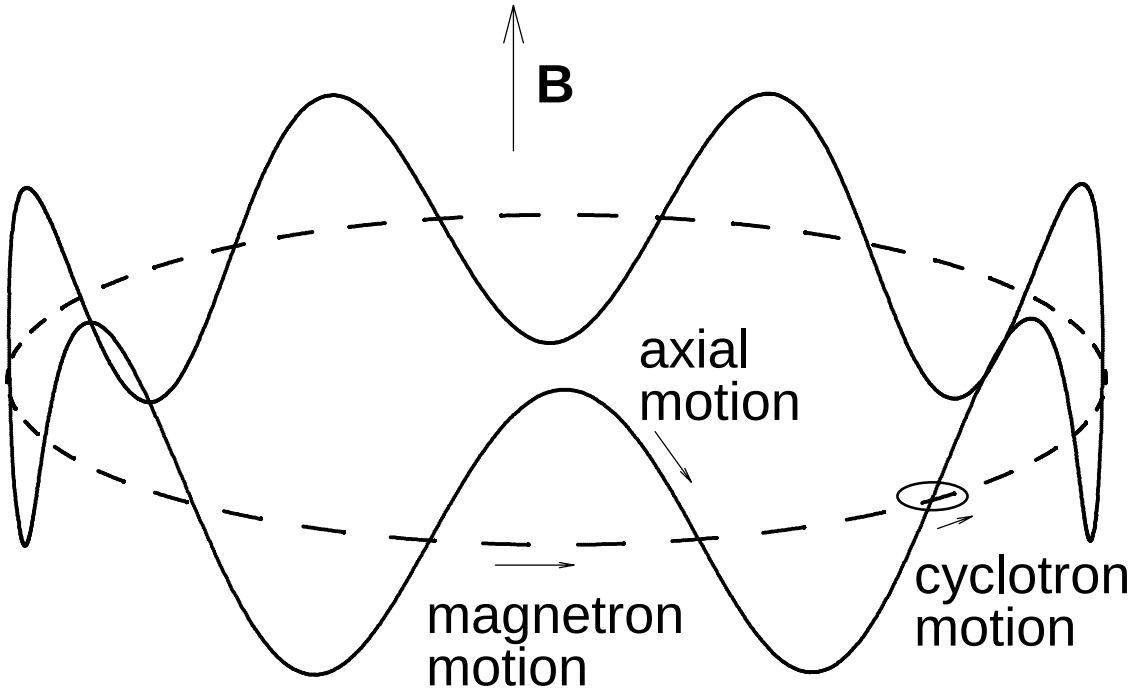

Figure 1.1: The three independent motions in an ideal Penning trap: the axial oscillation parallel to the magnetic field, the slow $\mathbf{E} \times \mathbf{B}$ magnetron drift in the plane perpendicular to the field, and the fast cyclotron motion (shown as a small circle) in the same plane.

1.2 One Electron in a Penning Trap

The environment for the physical realization of this study is one electron in a Penning trap. An ideal Penning trap is an electric quadrupole field superimposed on a spatially homogeneous magnetic field. A charged particle bound in such a trap has three independent oscillatory degrees of freedom: the slightly modified cyclotron motion at ω_c' in the plane perpendicular to the magnetic field, the axial motion at ω_z parallel to the magnetic field, and the magnetron $\mathbf{E} \times \mathbf{B}$ drift motion at ω_m, also in the radial plane perpendicular to the magnetic field (see Fig. 1.1). For a trapped

electron, the three oscillation frequencies are typically separated by factors of more than a thousand,

$$\omega_c'/2\pi \simeq 150\text{GHz} \tag{1.1}$$

$$\omega_z/2\pi \simeq 60\text{MHz} \tag{1.2}$$

$$\omega_m/2\pi \simeq 12\text{kHz}, \tag{1.3}$$

being experimentally fixed by the trap magnetic field, the strength of the static trap potential, and the trap size. A detailed description of these three motions may be found in [15], but the basic features are highlighted here.

The axial oscillation is the only directly detected motion: The cyclotron frequency is too fast, and the magnetron motion contains less information about the electron. A typical axial detector, which also resistively damps the axial motion, is a cold 4.2 K tuned circuit resonant with the axial frequency. Johnson noise from the detection resistor couples to the cyclotron motion via special relativity, and is the subject of Chapter 6. Cyclotron excitations are experimentally detected as relativistic shifts in the axial frequency.

In this work we focus upon the cyclotron oscillator. We entirely ignore the magnetron drift motion. This slow rotation is essentially decoupled from the others, and can be experimentally cooled so its radius is very small. Other than the noise coupling discussed in Chapter 6, we also ignore the axial motion, assuming an ideal detector measures the cyclotron excitation. Most of the calculation, therefore, deals with one free electron in a magnetic field and with cyclotron frequency ω_c (which must be interpreted as the modified ω_c' when applied to an electron in a Penning trap).

In Chapter 2 the classical relativistic equation of motion for an electron in a

magnetic field is derived and interpreted. Variables are chosen to facilitate comparisons with the quantum model introduced and discussed in Chapter 3. The quantum treatment in Chapter 3 utilizes raising and lowering operators to explore features of the undamped anharmonic oscillator with and without a drive. Dissipation via coupling to a finite temperature reservoir is then introduced, using both a density operator and a Monte Carlo wave-function approach. The two approaches are shown analytically and computationally to agree. In addition, the choice of measurement operators for the anharmonic oscillator is discussed in regard to the question of whether the emitted photon frequency is resolvable or not. In Chapter 4, the solutions to the master equation show persistent instability even when resonantly driven. Partial revivals of an initially harmonic coherent state are seen, as the Q-function evolves into a dressed coherent state of the anharmonic oscillator. Chapter 5 discusses implications for making part-per-billion cyclotron frequency measurements, and Chapter 6 treats the effect of stochastic cyclotron frequency fluctuations, originating from coupled axial energy fluctuations or from a fluctuating driving force.

Chapter 2

Classical Cyclotron Motion

This chapter is an introduction to the classical motion of a relativistic electron in a Penning trap. It not only builds an essential framework for the ensuing quantum mechanical analysis, but also provides insight into understanding some of the unexpected phenomena we report in later chapters.

The classical relativistic motion for an electron of charge $-e$ and rest mass m in a uniform magnetic field $\mathbf{B} = B\hat{\mathbf{z}}$ is governed by the Lorentz force

$$d(m\gamma\mathbf{v})/dt = -(e/c)\mathbf{v} \times \mathbf{B} - e\mathbf{E}_{\text{drive}} + \mathbf{F}_r, \tag{2.1}$$

where $\mathbf{v}$ is the electron velocity and γ is the usual relativistic factor, $\gamma = 1/\sqrt{1 - \left(\frac{\mathbf{v}}{c}\right)^2}$. The terms $\mathbf{E}_{\text{drive}}(\text{t})$ and $\mathbf{F}_r$ are due to an external electric driving field and radiation damping, respectively. The motion is in a circle [16] with angular frequency

$$\omega = \frac{eB}{\gamma mc} = \frac{\omega_c}{\gamma}, \tag{2.2}$$

where we take the cyclotron frequency ω_c to be the unshifted value which pertains to low electron speeds. Special relativity makes the oscillator slightly anharmonic.

An increase in cyclotron energy increases the relativistic factor γ and thus decreases the resonant frequency. (Similarly, relativity couples axial noise to the cyclotron frequency as discussed in Ch. 6.)

In free space, the motion would be brought to thermal equilibrium with the 4.2 K environment by synchrotron radiation at the spontaneous emission rate $\gamma_c = \gamma_{\rm fs}$, where

$$\gamma_{\rm fs} = \frac{4r_0\omega_c^2}{3c}, \tag{2.3}$$

$r_0 \simeq 2.8 \times 10^{-13}$ cm is the classical electron radius, and c is the speed of light. For a cyclotron frequency near 150 GHz, the free space damping time is $\gamma_{\rm fs}^{-1} \simeq 90$ ms. In a Penning trap cavity environment, the spontaneous emission rate γ_c can be either enhanced or inhibited [17–19], by tuning the cyclotron frequency relative to microwave resonances of the cavity.

We use the dipole approximation for the microwave driving force, valid because the $\mathbf{k}\cdot\boldsymbol{\rho}$ term in the microwave driving field is $\sqrt{2E_c/mc^2} \leq 0.008$, where 0.008 pertains to the maximum observed cyclotron excitation $E_c = 16.2$ eV [19]. As is usually done, we write the field $\mathbf{E}_{\rm drive}(\rm t)$ as the sum of co-rotating and counter-rotating components and neglect the non-resonant counter-rotating components. Then the driving electric field is

$$\mathbf{E}_{\rm drive}(t) = E_0\left[\hat{\mathbf{x}}\cos(\omega_d t) + \hat{\mathbf{y}}\sin(\omega_d t)\right]. \tag{2.4}$$

2.1 Relativistic Motion

Combining the B-field term and the radiation damping term with Eq. 2.1 gives the equation of motion found in [15],

$$\frac{d}{dt}\left[\gamma \mathbf{v}(t)\right] = \omega_c \hat{\mathbf{z}} \times \mathbf{v}(t) - \frac{1}{2}\gamma_c \mathbf{v}(t) - \frac{e}{m}\mathbf{E}_{\text{drive}}(t). \tag{2.5}$$

Using similar notation to [15] with complex velocity $v(t) = v_x(t) + iv_y(t)$ and rotating frame $\gamma v(t) = u(t)e^{i\omega_d t}$, the equation of motion can be written to second order in $|u|^2/c^2$ as

$$\dot{u}(t) + i\left\{\omega_d - \omega_c\left[1 - \frac{1}{2}\frac{|u(t)|^2}{c^2}\right]\right\}u(t) + \frac{1}{2}\gamma_c u(t) = -\frac{e}{m}E_0. \tag{2.6}$$

However, to later compare with the raising and lowering operators of quantum theory, we use related notation

$$\alpha(t) = \sqrt{\frac{m}{2\hbar\omega_c}}\,\gamma\left(v_x(t) - iv_y(t)\right) = \sqrt{\frac{m}{2\hbar\omega_c}}\,\gamma\, v^*(t) \tag{2.7}$$

$$\alpha^*(t) = \sqrt{\frac{m}{2\hbar\omega_c}}\,\gamma\left(v_x(t) + iv_y(t)\right) = \sqrt{\frac{m}{2\hbar\omega_c}}\,\gamma\, v(t). \tag{2.8}$$

We go to a rotating frame $\alpha(t) = \bar{\alpha}(t)e^{-i\omega_d t}$. Notice the direction of rotation is opposite the $v \to u$ rotation direction because α is proportional to v^* rather than v. Also notice a factor of γ is included in the definition of α rather than saving it for the relationship between α and $\bar{\alpha}$ (in order to simplify the rotating frame convention). Then the equation of motion in the rotating frame is

$$\dot{\bar{\alpha}}(t) - i\left\{\omega_d - \omega_c\left[1 - |\bar{\alpha}(t)|^2\frac{\hbar\omega_c}{mc^2}\right]\right\}\bar{\alpha}(t) + \frac{1}{2}\gamma_c\bar{\alpha}(t) = -\sqrt{\frac{(eE_0)^2}{2m\hbar\omega_c}}. \tag{2.9}$$

The first order relativistic correction appears as a term proportional to $|\bar{\alpha}|^2$ in the square brackets.

The total energy of this classical anharmonic oscillator is given by the relativistic expression $E = \sqrt{(mc^2)^2 + (\mathbf{p}c)^2}$ where $\mathbf{p}$ is the kinetic momentum

$$\mathbf{p} = m\gamma\mathbf{v}, \tag{2.10}$$

not too be confused with the canonical momentum $\mathbf{P} = \mathbf{p} - (e/c)\mathbf{A}$ which will be used in the quantum Hamiltonian formulation. Expanded in terms of $\mathbf{p}^2/m^2c^2$, and also written in terms of $|\bar{\alpha}|^2$, the anharmonic cyclotron energy becomes

$$\begin{aligned} E &= mc^2 + \frac{\mathbf{p}^2}{2m} - \frac{1}{2mc^2}\left(\frac{\mathbf{p}^2}{2m}\right)^2 + ... && (2.11) \\ &= mc^2 + \hbar\omega_c|\bar{\alpha}|^2 - \frac{1}{2mc^2}\left(\hbar\omega_c|\bar{\alpha}|^2\right)^2 + ... && (2.12) \end{aligned}$$

This relativistic expansion for energy will be the starting point for the quantum Hamiltonian treatment of Ch. 3. In most discussion of cyclotron excitations, however, the harmonic term $\hbar\omega_c|\bar{\alpha}|^2$ or sometimes just $|\bar{\alpha}|^2$ will be referred to as energy.

2.2 Steady State

The steady state of this anharmonic oscillator can be studied by taking $\dot{\bar{\alpha}}(t) = 0$. It is convenient to characterize the drive strength by the maximum response $\bar{\alpha}_{\max}$ and the anharmonicity strength by the dimensionless parameter N, where

$$\begin{aligned} |\bar{\alpha}_{\max}|^2 &= \left(\frac{2}{\gamma_c}\right)^2 \frac{(eE_0)^2}{2m\hbar\omega_c} && (2.13) \\ N &= -\frac{\omega_c}{\gamma_c}|\bar{\alpha}_{\max}|^2\left(\frac{\hbar\omega_c}{mc^2}\right). && (2.14) \end{aligned}$$

The steady state energy $|\bar{\alpha}_{ss}|^2$, as a function of drive frequency ω_d, can be expressed in terms of these parameters as a "tilted" Lorentzian,

$$\left|\frac{\bar{\alpha}_{ss}}{\bar{\alpha}_{\max}}\right|^2 = \frac{1}{1+4\left[\frac{\omega_d-\omega_c}{\gamma_c} - N\left|\frac{\bar{\alpha}_{ss}}{\bar{\alpha}_{\max}}\right|^2\right]^2}. \tag{2.15}$$

Fig. 2.1a shows a plot of such a resonance curve for a mild anharmonicity case $N = -10$ (solid) and the harmonic case $N = 0$ (dashed). The harmonic curve is a familiar Lorentzian response. The anharmonic curve demonstrates how the resonant frequency of the oscillator shifts downward as the excitation energy increases. The triple-valued region is responsible for hysteresis and bistability. The lower and upper energy curves correspond to regions of stable motion, while the mid-energy section between points A and B corresponds to a region of unstable motion. This is proven by expanding the response $\bar{\alpha}(t)$ about its steady state value and solving for the time dependence of a small deviation from equilibrium. (See [15].) Along the stable branches, the deviation damps to zero, while along the unstable branch it blows up.

The bistability leads to hysteresis if the drive frequency is swept through resonance. When swept from high frequencies to low, the drive excites the oscillator along the upper stable curve, as indicated by the arrow. When the drive is swept from low frequencies to high, however, the oscillator remains relatively unexcited on the lower branch until the drive reaches the frequency for point A, at which point the oscillator energy jumps up to the single valued portion of the response curve to continue.

The first experimental observation of a relativistic electron cyclotron resonance was reported by Gabrielse, Dehmelt and Kells [1]. A typical experimental curve taken in the currently used hyperbolic trap is shown in Fig. 2.2. The illustrated resonance has anharmonicity parameter $N \simeq -10^5$, which is so much larger in

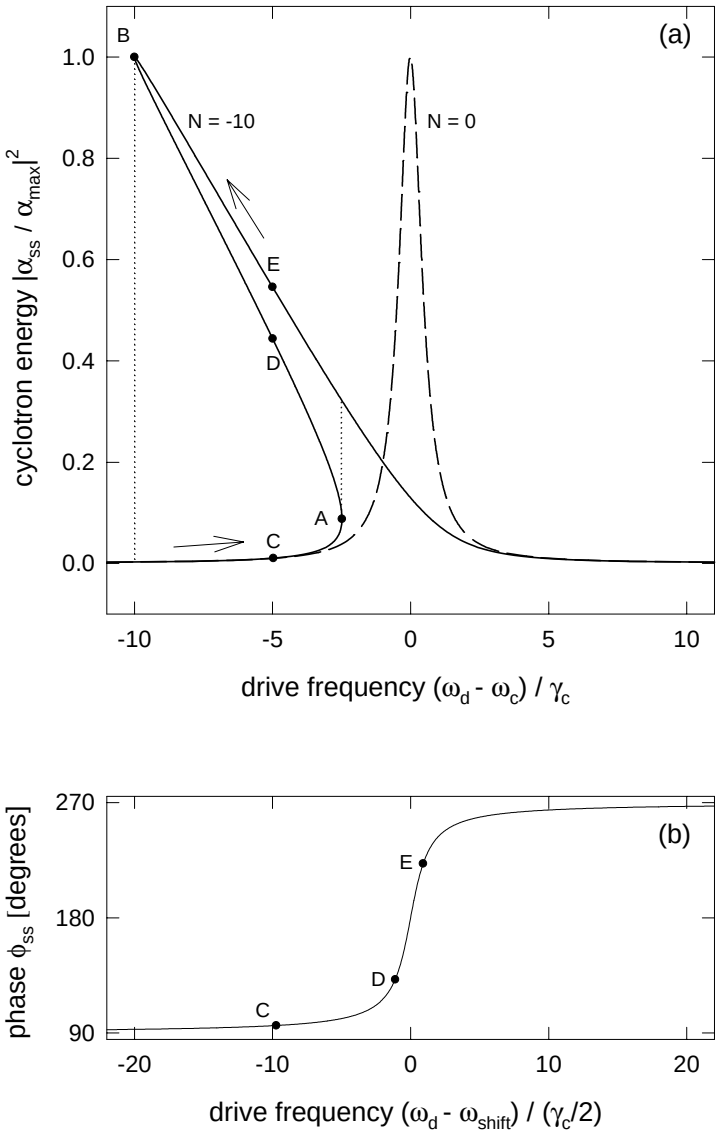

Figure 2.1: (a) Steady state squared amplitudes of both a harmonic (dashed) and an anharmonic (solid) driven damped oscillator. (b) Steady state phase lag with respect to a drive for the anharmonic oscillator shown in (a). The phase curve is similar to that of a *harmonic* oscillator when plotted versus $\omega_c - \omega_{\rm shift}$, where $\omega_{\rm shift}$ is the amplitude dependent resonant frequency of Eq. 2.16. Points C and E are the two stable solutions and D is the single unstable solution for the fixed drive frequency to be used in Fig. 2.3.

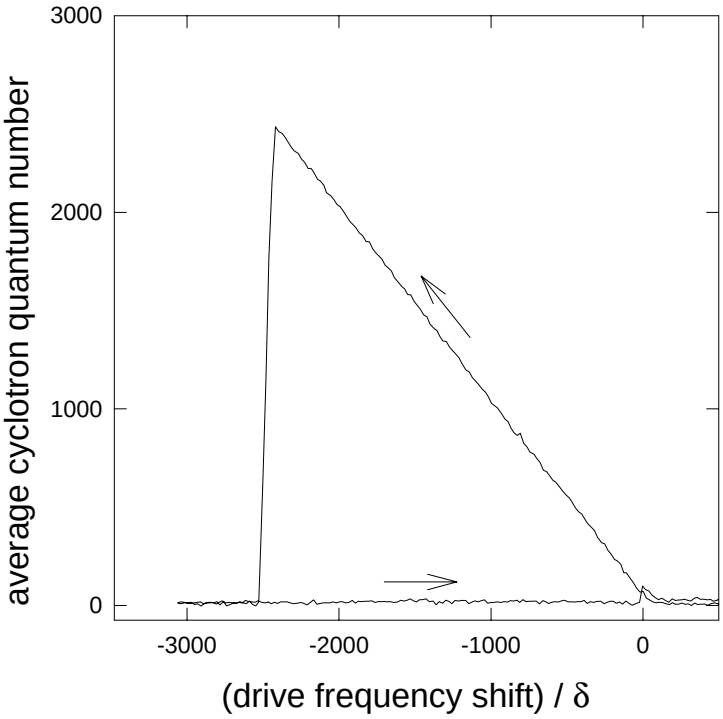

Figure 2.2: Observed single electron relativistic cyclotron excitation [19]. Excitation energy is detected as a relativistic shift of the axial frequency. Arrows indicate the sweep direction of a microwave drive. Hysteresis and bistability are observed. Calculations will show that instability of the upper energy portion of the "stable" branch is what limits the extent of the excitation (as opposed to microwave power).

magnitude than the $N = -10$ shown in Fig. 2.1a, that its width is too narrow to be visible.

The other classical parameter that will be used in quantum comparisons is the steady state response phase ϕ_{ss}, defined by $\bar{\alpha}_{ss} = |\bar{\alpha}_{ss}|e^{i\phi_{ss}}$. Momentarily going back to the stationary frame expression for the response $\alpha_{ss} = |\bar{\alpha}_{ss}|e^{-i(\omega_d t - \phi_{ss})}$ and writing the driving field as $E_x - iE_y = E_0 e^{-i\omega_d t}$, reveals that ϕ_{ss} is a phase lag of the response with respect to the drive. It, too, is found by setting $\dot{\bar{\alpha}}(t) = 0$. When

written in terms of the shifted cyclotron frequency

$$\omega_{\text{shift}} = \omega_c \left[1 - |\bar{\alpha}_{ss}|^2 \frac{\hbar\omega_c}{mc^2} \right], \tag{2.16}$$

the solution for the phase lag ϕ_{ss} looks the same as for a driven damped *harmonic* oscillator with $\omega_{\text{shift}} = \omega_c$, and is given by

$$\phi_{ss} = \tan^{-1}\left(\frac{\omega_d - \omega_{\text{shift}}}{\gamma_c/2} \right). \tag{2.17}$$

Fig. 2.1b shows a plot of the response phase in terms of the drive frequency. Far above resonance the response lags the drive by $3\pi/2$, while far below resonance it lags by only $\pi/2$. When the drive is exactly resonant with the shifted cyclotron frequency ($\bar{\alpha}_{ss} = \bar{\alpha}_{\max}$), the response and the drive are π out of phase, as can be seen by zeroing the curly bracket term in Eq. 2.9. This differs from the familiar $\pi/2$ phase lag for a resonantly driven simple harmonic oscillator. The difference arises merely from the fact that we are treating velocity oscillations as opposed to the standard spatial oscillations.

2.3 Time Evolution

The steady state response is fully characterized by the amplitude and phase of $\bar{\alpha}_{ss}$. The time evolution of the system is most easily described in phase-space. If we plot $Re[\bar{\alpha}(t)]$ versus $Im[\bar{\alpha}(t)]$ for a fixed drive, we see the trajectory that $\bar{\alpha}$(t) follows. Remember these real and imaginary parts are proportional to v_x and v_y, so phase-space trajectories can be visualized as actual cyclotron trajectories. (In the quantum development of the next chapter, it will be shown that these real and imaginary parts satisfy the same commutation relation as the commonly used phase-space variables

q and p_q, up to a constant.) Fig. 2.3a shows two such computed trajectories for a drive frequency in the bistable region of the response curve. There are two stable attractors to which $\bar{\alpha}$(t) damps, one excited state and one unexcited state near the origin. These two attractors correspond to the steady state amplitudes and phases labeled E and C in Fig. 2.1. The definition of stability assures that for an initial excitation close to the high energy stable attractor, the oscillator will remain excited by damping to that attractor. However, for displacements far from equilibrium, it is not obvious into which attractor the oscillator will damp.

Fig. 2.3b illustrates the excited-state's stable 'bucket', defined as those points in phase-space which eventually damp to the excited attractor. The rest of phase-space is then the unexcited-state's stable 'bucket'. The two stable attractors are again labeled E and C. (Also shown is the unstable steady state solution, located on a boundary between the 2 'buckets', labeled D.) These pictures help us to understand how large a fluctuation is necessary to de-excite a stable resonance. The buckets shown, however, are for the still mild anharmonicity parameter $N = -10$. The spiral structure gets even narrower (and therefore harder to calculate and depict graphically) for stronger anharmonicity. This stable 'bucket' picture will be revisited using a quantum mechanical model in Ch. 4, where we seek to reproduce the stability for some classical limit while using the correct quantum model.

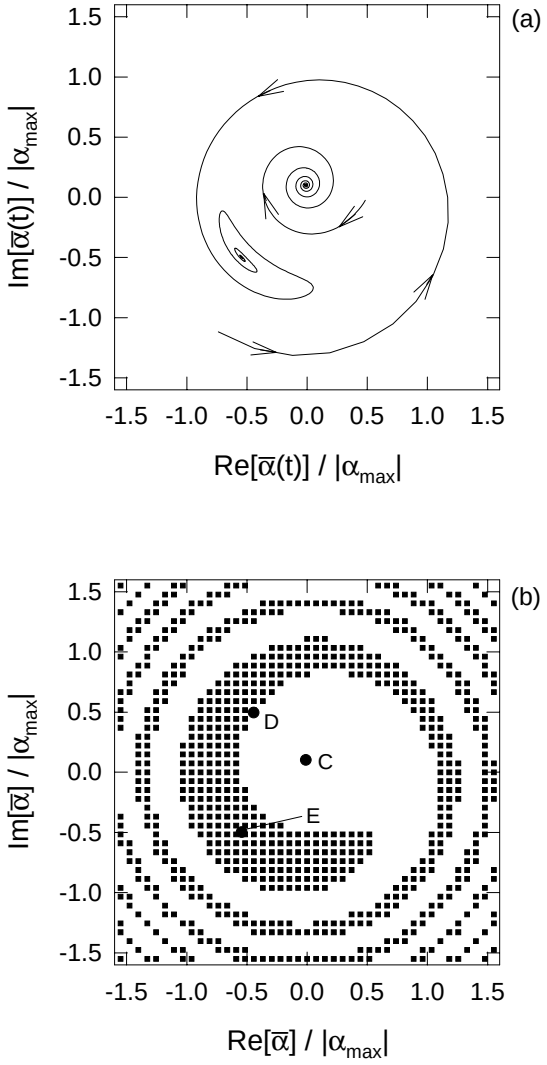

Figure 2.3: Two classical phase-space trajectories in (a) and a map of the excited state's stable bucket in (b) for $N = -10$ and a drive frequency corresponding to the steady state solutions C, D, and E of Fig. 2.1. Trajectories in (a) damp to either the excited stable attractor E or the unexcited stable attractor C. Phase-space points which damp to the excited attractor are shown in (b) (filled squares), along with the stable and unstable solutions C, D, and E (filled circles).

Chapter 3

Quantum Cyclotron Motion

In this chapter the cyclotron motion for an electron of charge $-e$ in a magnetic field $\mathbf{B}$ is described quantum mechanically. Raising and lowering operators analogous to classical phase-space variables are defined, and a quantum Hamiltonian is derived. First, features of the undamped anharmonic oscillator with and without a drive are explored. Then, dissipation via coupling to a finite temperature reservoir is introduced, using both a density operator and a Monte Carlo wave-function approach. The two approaches are shown analytically and computationally to agree. In addition, the choice of measurement operators for the anharmonic oscillator is discussed in regard to the question of whether the emitted photon frequency is resolvable or not. This sets the stage for solutions to the master equation which will be presented in Ch. 4.

3.1 Undamped Quantum Hamiltonian

We begin with the 2-dimensional harmonic Hamiltonian taken from the first term of the relativistic energy expansion of Eq. 2.11 (ignoring the rest mass term),

$$H_c = \frac{\mathbf{p}^2}{2m} = \frac{p_x^2 + p_y^2}{2m}. \tag{3.1}$$

The kinetic momentum components p_x and p_y are non-commuting and satisfy

$$[p_x, p_y] = -i\hbar\omega_c m. \tag{3.2}$$

The commutation relation is derived from the usual canonical commutation relations $[\rho_k, P_l] = i\hbar\delta_{kl}$, where the canonical radial momentum $\mathbf{P}$ is given by $\mathbf{P} = \mathbf{p} - (e/c)\mathbf{A}$, the radial position is given by $\boldsymbol{\rho}$, and the gauge is chosen so that $\mathbf{A} = (1/2)\mathbf{B} \times \boldsymbol{\rho}$.

The cyclotron Hamiltonian can be recast as a simple 1-dimensional oscillator with canonically conjugate variables q and p_q

$$H_c = \frac{1}{2}m\omega_c^2 q^2 + \frac{{p_q}^2}{2m} \tag{3.3}$$

if we take

$$q = \frac{p_x}{m\omega_c} \qquad p_q = -p_y. \tag{3.4}$$

Then raising and lowering operators can be defined as usual,

$$a = \sqrt{\frac{m\omega_c}{2\hbar}}\, q + i\sqrt{\frac{1}{2m\hbar\omega_c}}\, p_q = \sqrt{\frac{1}{2m\hbar\omega_c}}\,(p_x - ip_y) \tag{3.5}$$

$$a^\dagger = \sqrt{\frac{m\omega_c}{2\hbar}}\, q - i\sqrt{\frac{1}{2m\hbar\omega_c}}\, p_q = \sqrt{\frac{1}{2m\hbar\omega_c}}\,(p_x + ip_y). \tag{3.6}$$

The commutation relation $[q, p_q] = i\hbar$ ensures that $[a, a^\dagger] = 1$, and the quantum

harmonic cyclotron Hamiltonian is the familiar

$$H_c = \hbar\omega_c(a^\dagger a + \frac{1}{2}). \tag{3.7}$$

Notice that Eqs. 3.5 and 3.6 satisfy equations which are the same as those for the classical variables α and α^* defined last chapter in Eqs. 2.7 and 2.8.

We digress to consider a complete Dirac treatment which includes relativistic shifts of the cyclotron energy levels, and two spin states for the electron [15]. The energy level structure shown is in Fig. 3.1, with a separate Landau ladder for each value of the electron spin. The relativistic anharmonicity gives a diminishing spacing between successive Laundau levels. The transition frequency between Landau level n, m_s and $n+1, m_s$ is shifted from ω_c by an amount proportional to the cyclotron quantum number and also dependent on the spin state,

$$\Delta\omega_{nm_s} = -\delta(n + 1 + m_s). \tag{3.8}$$

The anharmonicity parameter

$$\delta = \omega_c \frac{\hbar\omega_c}{mc^2} \tag{3.9}$$

gives the shift in transition frequency per Landau level. For a cyclotron frequency near 150 GHz, the shift per level, $\delta/2\pi \simeq 180$ Hz, is a ppb shift.

As can be seen from the energy level figure, the $m_s = \frac{1}{2}$, $n = 0$ state is nearly degenerate with the $m_s = -\frac{1}{2}$, $n = 1$ state. This is due to the spin precession frequency ω_s being nearly equal to the cyclotron frequency ω_c, the slight inequality being characterized by the g factor,

$$\frac{g}{2} = \frac{\omega_s}{\omega_c}. \tag{3.10}$$

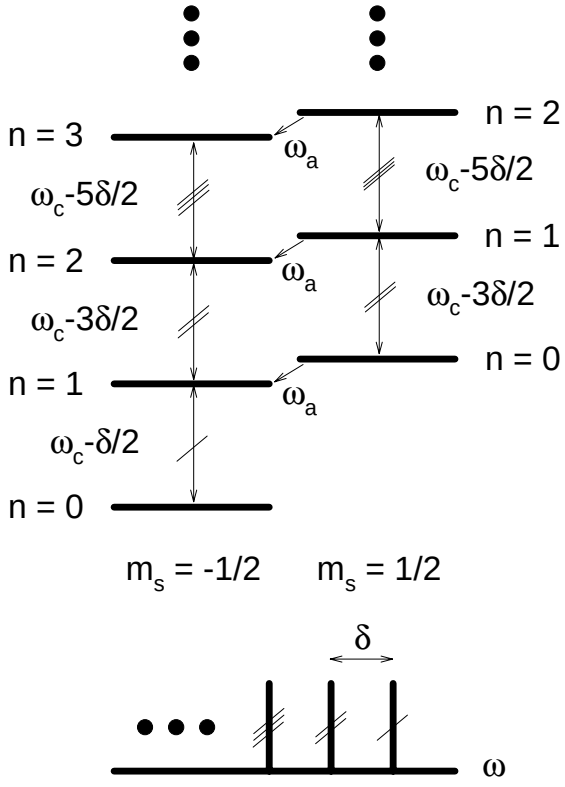

Figure 3.1: Energy levels of a spin $\frac{1}{2}$ electron in a magnetic field. Anomaly transitions at the frequency $\omega_a = \omega_s - \omega_c$ are labeled, where ω_s is the electron spin precession frequency. Successive cyclotron transitions are spaced by the anharmonic 1 ppb shift per level, δ.

The g factor is nearly equal to 2, and can be calculated using the theory of quantum electrodynamics. The crucial measurements for determining $g - 2$ of the electron experimentally to 1 ppb, are that of the cyclotron frequency ω_c and the anomaly frequency ω_a. An anomaly transition is a simultaneous spin flip and cyclotron transition. In previous g factor measurements, a magnetic bottle was introduced to increase the coupling between the axial and cyclotron motions in order to enable detection of changes in the cyclotron quantum number of 1, and thus immediate detection of anomaly transitions. [10]. The bottle, however, broadened the cyclotron

and anomaly lines which needed to be measured. Since the spin motion has a near infinite lifetime, anomaly transitions can instead be detected after the fact by simply measuring whether a spin flip has occurred. We investigate the possibility to use the cyclotron ladder as a probe of the spin state, identifying spin flips as shifts in the ground state cyclotron transition by δ (See Fig. 3.1). Thus, ppb cyclotron frequency resolution is needed not only for the ω_c measurement but also for spin flip detection and the ω_a measurement.

At 4.2 K, the electron probability is spread among the Landau levels for one of the spin ladders shown, according to the Boltzmann thermal distribution

$$P(n) = \left(1 - e^{-\hbar\omega_c/kT}\right) e^{-n\hbar\omega_c/kT}, \tag{3.11}$$

which places the electron in the ground state roughly 80% of the time. Observed excitations similar to the one shown in Fig. 2.2, take the electron from the ground state ($n = 0$) to an average energy as large as 16.2 eV ($n = 26,500$) [19]. Initially this seemed a natural system for investigating the transition from a quantum regime to a classical one. As results of Ch. 4 indicate, however, the behavior of large excitations diverges from the classical expectation. Still, since in a classical regime, we can understand the effects of damping, noise, and temperature as fluctuations in the response variable $\bar{\alpha}$ away from the stable phase-space attractor, we introduced a quantum model with the hope of reproducing classical behavior in some limit.

The final step in the Hamiltonian derivation, before including dissipation, is to formulate a quantum mechanical characterization of the external microwave drive. We use the same rotating wave drive field $\mathbf{E}_{\text{drive}}(\text{t})$ as in Ch. 2, using a vector

potential in the Coulomb gauge ($\mathbf{E}_{\text{drive}} = -\frac{1}{c}\partial\mathbf{A}_{\text{drive}}/\partial t$),

$$\mathbf{A}_{\text{drive}}(t) = \frac{c}{\omega_d} E_0 \left[-\hat{\mathbf{x}}\sin(\phi_d(t)) + \hat{\mathbf{y}}\cos(\phi_d(t))\right], \tag{3.12}$$

and allowing the drive frequency ω_d to change in time so that the drive phase $\phi_d(t)$ is given by

$$\phi_d(t) = \phi_d(0) + \int \omega_d(t)dt. \tag{3.13}$$

For simplicity, in the classical derivation of Ch. 2, the drive frequency ω_d was fixed and the initial phase $\phi_d(0)$ was taken to be zero.

The drive Hamiltonian is found by including this new vector potential in the original cyclotron Hamiltonian

$$H_c = \frac{\mathbf{p}^2}{2m}. \tag{3.14}$$

Since $\mathbf{p} = \mathbf{P} + (e/c)\mathbf{A}_{\text{trap}} + (e/c)\mathbf{A}_{\text{drive}}$, the driven kinetic momentum becomes $\mathbf{p} \rightarrow \mathbf{p} + (e/c)\mathbf{A}_{\text{drive}}$. Equivalently, a drive Hamiltonian is added,

$$H_{\text{drive}} = \frac{e}{mc}\mathbf{p}\cdot\mathbf{A}_{\text{drive}}. \tag{3.15}$$

(The ${\mathbf{A}_{\text{drive}}}^2$ term is ignored since it is smaller than the $\mathbf{p}\cdot\mathbf{A}_{\text{drive}}$ term by the factor $\Omega_R/(\omega_c\sqrt{n})$, which is less than 10^{-9} for $\Omega_R/\delta \approx 1$). Eqs. 3.5 and 3.6 for the cyclotron raising and lowering operators can then be inverted to give expressions for the kinetic momentum components,

$$p_x = \sqrt{\frac{m\hbar\omega_c}{2}}(a + a^\dagger) \tag{3.16}$$

$$p_y = i\sqrt{\frac{m\hbar\omega_c}{2}}(a - a^\dagger), \tag{3.17}$$

which combined with the expression for $\mathbf{A}_{\text{drive}}$, give the drive Hamiltonian

$$H_{\text{drive}} = \frac{\hbar\Omega_R}{2}\left[ae^{i(\phi_d(t)+\pi/2)} + a^\dagger e^{-i(\phi_d(t)+\pi/2)}\right]. \tag{3.18}$$

The drive power is now characterized as a Rabi frequency

$$\Omega_R = \sqrt{\frac{2(eE_0)^2}{m\hbar\omega_c}}. \tag{3.19}$$

Table 3.1: Cyclotron Oscillator Experimental Parameters

system frequencies and rates		
cyclotron frequency	ω_c	2π(150 GHz)
free space damping	γ_{fs}	2π(2 Hz)
anharmonicity	δ	2π(180 Hz)
temperature parameters		
temperature	T	4.2 K
average thermal excitation	$\bar{n}$	0.21
Boltzmann ratio	$\hbar\omega_c/kT$	1.7

A summary of our system parameters is shown in Table 3.1. Notice the electron cyclotron oscillator is unusual in that it has some characteristics of a weakly anharmonic system and some of a strongly anharmonic system. The anharmonicity is weak insofar as the relativistic shifts are small compared to the cyclotron frequency ($\delta/\omega_c \simeq 10^{-9}$). However, the anharmonicity is strong insofar as relativistic shifts are large compared to the damping width ($\delta/\gamma_{\text{fs}} \simeq 100$). This latter "strong" anharmonicity distinguishes our system from familiar mass-on-a-spring classical oscillators which are always harmonic at low enough energies, in the sense that damping width masks the smaller anharmonicity shift (*natural linewidth* $\gamma \gg n\delta$). Our system would not become harmonic till $n \simeq \frac{1}{100}$. In other words, the cyclotron oscillator is

anharmonic throughout the quantum regime. A similar nonlinear quantum oscillator has been studied both experimentally and theoretically by Stroud [7–9, 20]. His characterization of Rydberg wave packets reveals similar revival and interference properties [7–9] to what we find for the one-electron oscillator. While these wave packets look very similar to the dressed coherent state probability distributions we will present in Ch. 4, his system does differ slightly insofar as it does not include a driving force, and dynamics considered occur in times short compared to damping.

3.2 Two State Model and Adiabatic Fast Passage

We now describe the excitation process which produces observed signals, such as shown in Fig. 2.2, in a quantum mechanical language. An intuitive understanding of the excitation process can be obtained by treating the anharmonic oscillator as a series of two-state systems. The Landau levels are not harmonic, and successive two-level spacings are separated from one another in frequency by the relativistic factor δ.

A diagonal two-state Hamiltonian plus an off-diagonal drive Hamiltonian can be diagonalized in a dressed state basis, the base appropriate for the driven system. The 'dressed' eigenstates are in general a linear combination of the two 'bare' states, and depend on drive frequency and power. For drive frequency far above or far below resonance, the 'dressed' eigenstates are simply the 'bare' states. Slowly sweeping the drive frequency through resonance transfers the population from the lower to the upper 'bare' state and vice versa. This is known as adiabatic fast passage or adiabatic passage. If the drive is swept nonadiabatically, the transition probability

is given by the Landau-Zener formula [21]

$$P = 1 - e^{-2\pi\Gamma_{\rm LZ}} \tag{3.20}$$

where

$$\Gamma_{\rm LZ} = \frac{{\Omega_{Rabi}}^2}{4|d\omega_d/dt|} \tag{3.21}$$

is the Landau-Zener parameter, and Ω_{Rabi} is the Rabi frequency for the two-state system. The sweep can be shown to be adiabatic when $\Gamma_{\rm LZ} \gg \frac{1}{4}$.

The excitation process up the Landau ladder may be thought of as a series of two-state transitions. Consider the electron cyclotron oscillator in its ground state. As the drive is swept from high frequency to low, it first passes the $n = 0 \rightarrow 1$ transition frequency, and the electron moves to the $n = 1$ state. As the sweep continues, the $1 \rightarrow 2$ resonance is passed, causing a transition to $n = 2$, then the $2 \rightarrow 3$ resonance is passed and so on. In this way, the cyclotron motion can be excited to high Landau levels, just as in the classical picture. For a fixed sweep speed $d\omega_d/dt$, the process becomes more and more adiabatic because the Rabi frequency, Ω_n, for the $n \rightarrow n+1$ transition grows as $\sqrt{n}$ times the $0 \rightarrow 1$ Rabi frequency,

$$\Omega_n = \Omega_R\sqrt{n}. \tag{3.22}$$

With this model of the excitation process, we are able to conceive of a method for measuring the ground state resonant frequency to the ppb precision desired. The large observed excitation is a binary signal that indicates only whether an excitation process was successful or not. The frequency resolution comes from knowledge of the drive's start frequency for a given sweep. Clearly if we sweep the frequency of a weak drive downward, starting below the $0 \rightarrow 1$ resonant frequency, the drive never

passes the first resonance, and the electron remains in the ground state. By plotting probability of excitation versus start frequency, we see the probability change from 0 to 1 when the drive's start frequency is near the ground state transition frequency. The width and offset of such a probability resonance depend somewhat on drive power, but we should be able to achieve 1 δ resolution for small Rabi frequencies ($\Omega_R/\delta \leq 1$).

Computation results presented in the next chapter confirm the validity of the simple adiabatic passage model, even for large Rabi frequencies $\Omega_R/\delta \geq 1$, for which dressed two-state energy levels actually overlap. In addition, the computations address the very important question of the role of spontaneous emission, which the simple model cannot address.

3.3 Dissipation and the Master Equation

To introduce dissipation, we solve the master equation for the density operator, quantum theory of damping for the anharmonic oscillator. In the next section we describe an equally valid Monte Carlo wave-function approach, which yields the same ensemble average behavior. The wave-function approach, however, can model single experimental runs if appropriate measurement operators are chosen.

A series of papers have been written about quantum harmonic and anharmonic oscillators with damping and/or amplification [3–5, 22–25]. Master equation methods have been used to describe the difference between quantum mechanical and classical behavior [3–5]. Coherent states are often used to help conceptualize the quantum behavior in terms of classical motion [3–5]. Quantum-coherence effects do still emerge, but are found to be very sensitive to dissipation [3–5]. Even the weakest damping is found to be sufficient to restore classical behavior [3–5]. We

will see this destruction of coherence in our undriven damped system, but when the drive is added, quantum effects remain.

Often the master equation is transformed into a C-number equation, by representing the density operator in a coherent state base. The density operator $\bar{\sigma}$, in such a coherent state base $|\alpha\rangle$, is a joint probability distribution called a Q-function

$$Q(\alpha, \alpha^*) = \langle\alpha|\bar{\sigma}|\alpha\rangle. \tag{3.23}$$

The Q-function evolution equation for a damped, anharmonic oscillator has previously been solved analytically, but unfortunately, the time-dependent driven case has not been solved. Since the drive is integral to our excitation process, we perform a numerical analysis. We use the Q-functions as a pictorial language for visualizing the quantum probability distribution in a phase-space identical to the classical phase-space discussed earlier.

We begin with the familiar harmonic oscillator Hamiltonian (Sec. 3.1), $H_c = \hbar\omega_c(a^\dagger a + \frac{1}{2})$ Adding the relativistic corrections discussed earlier (ignoring spin) yields the anharmonic Hamiltonian

$$H_{\text{aho}} = H_c + \frac{\mu}{\hbar\omega_c}{H_c}^2 \tag{3.24}$$

where $\mu = -\delta/(2\omega_c)$. This Hamiltonian is the same form studied by Milburn [3, 5].

Eliminating the zero-point-energy does not change the quantum dynamics and reduces the Hamiltonian to another commonly studied form [6, 22, 25]

$$H_{\text{aho}} = \hbar(\omega_c - \frac{\delta}{2})a^\dagger a - \frac{1}{2}\hbar\delta(a^\dagger a)^2. \tag{3.25}$$

Since the harmonic oscillator n-levels are still eigenstates of H_{aho} (Eq. 3.25), we can

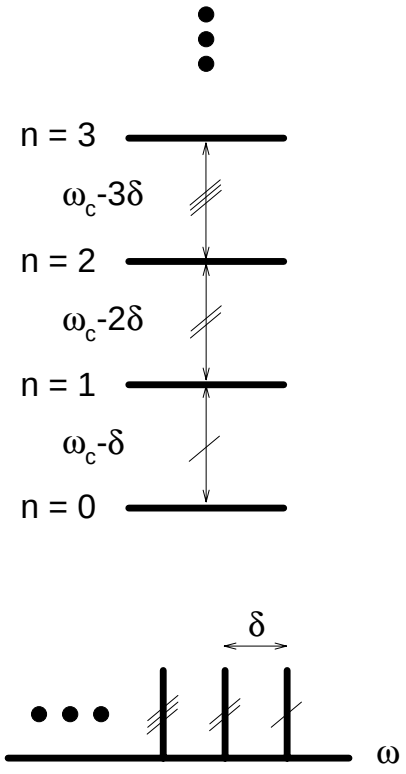

Figure 3.2: Landau levels for the anharmonic cyclotron Hamiltonian solved. The first transition frequency $\omega_c - \delta$ differs from the true ground state transition frequency by the ignored relativistic spin-dependent correction, $-m_s\delta$, where $m_s = \pm 1/2$.

easily find the energies of the first few levels and check the transition frequencies. The ground state has been defined to have energy 0, while the first excited state has energy $\hbar(\omega_c - \delta/2 - \delta/2)$, thus the first transition frequency is $\omega_c - \delta$. (See Fig. 3.2) This differs from the $n = 0 \rightarrow 1$ transition frequencies shown in Fig. 3.1 only by the ignored relativistic spin-dependent correction, $-m_s\delta$.

Dissipation is introduced by coupling the system to a large reservoir of oscillators. For dissipation via synchrotron radiation, these oscillators are the modes of a

radiation field

$$H_R = \hbar \sum_j \omega_j b_j^\dagger b_j, \tag{3.26}$$

and coupling to the reservoir is described by

$$V = \hbar[a^\dagger \sum_j g_j b_j + a \sum_j g_j^* b_j^\dagger]. \tag{3.27}$$

The full system-reservoir Hamiltonian, including the drive term from Eq. 3.18, is then

$$\begin{aligned} H &= \hbar(\omega_c - \frac{\delta}{2})(a^\dagger a) - \frac{1}{2}\hbar\delta(a^\dagger a)^2 \\ &\quad + \hbar \sum_j \omega_j b_j^\dagger b_j \\ &\quad + \hbar[a^\dagger \sum_j g_j b_j + a \sum_j g_j^* b_j^\dagger] \\ &\quad + \hbar[v_d(t) a^\dagger + v_d{}^*(t) a]. \end{aligned} \tag{3.28}$$

where $v_d(t) = \frac{1}{2}\Omega_R e^{-i(\phi_d(t)+\pi/2)}$ and $\phi_d(t) = \phi_d(0) + \int \omega_d(t) dt$ fully characterize the drive.

At zero temperature, the reservoir oscillators are in their ground states. A spontaneous emission from the cyclotron system is accompanied by a brief excitation of one reservoir oscillator. The standard Markoff approximation assumes that this excited reservoir oscillator is not able to coherently re-excite the system. The reservoir is assumed to have too many degrees of freedom to maintain such coherence or 'memory'. At nonzero temperature, the resonant reservoir oscillators have an average excitation $\bar{n}$ determined by the Boltzmann thermal distribution. This average excitation allows for stimulated emission and absorption in the cyclotron system but again, the reservoir quickly re-thermalizes. A theoretical derivation of the master

equation for a driven *harmonic* oscillator damped to such a heat bath can be found in Louisell [26, 27]. Adding the anharmonic piece of the Hamiltonian gives

$$\begin{aligned}\frac{\partial\sigma}{\partial t} &= -i(\omega_c - \frac{\delta}{2} - \Delta_R)[a^\dagger a, \sigma] + i\frac{\delta}{2}[(a^\dagger a)^2, \sigma] \\ &\quad + \frac{\gamma_c}{2}(2a\sigma a^\dagger - a^\dagger a\sigma - \sigma a^\dagger a) \\ &\quad + \gamma_c\bar{n}(a^\dagger\sigma a + a\sigma a^\dagger - a^\dagger a\sigma - \sigma a a^\dagger) \\ &\quad - iv_d(t)[a^\dagger, \sigma] - iv_d{}^*(t)[a\,, \sigma], \end{aligned} \tag{3.29}$$

where σ is the Schrödinger picture reduced density operator (reservoir variables traced over)

$$\sigma = Tr_R\{\rho\}, \tag{3.30}$$

ρ is the Schrödinger picture global density operator (cyclotron plus reservoir), Δ_R is a radiative shift analogous to the Lamb shift in an atom, and γ_c is the same cavity damping rate used in the classical equations. The first line includes the harmonic and anharmonic contributions. The second line results from zero temperature damping. The third line has the finite temperature damping contribution, and the fourth line results from the microwave drive. The radiative shift, Δ_R, has been shown to be small and will be neglected for the rest of this work [15].

Clearly it would be advantageous to choose an interaction picture in which the fast ω_c oscillation is removed, but there are several reasonable choices for the unperturbed Hamiltonian H_0. Choosing H_0 as the entire $H_{\rm aho}$ would eliminate the first line of Eq. 3.29 in the new master equation. The nonlinearity in $H_{\rm aho}$, however, would effectively lead to different rotating frame frequencies for each Landau level of the oscillator. While we used this choice to check for numerical consistency, the bulk of our work is done in a single frequency rotating frame. Still, the choice of rotation

frequency is not obvious, as the frame will only cancel out the rotation of at most one Landau level. Milburn chooses an unperturbed Hamiltonian of $H_0 = \hbar(\omega_c - \frac{\delta}{2})a^\dagger a$ to zero the entire $[a^\dagger a, \sigma]$ term in Eq. 3.29, but we choose the interaction picture frame rotating at ω_c by making the unperturbed Hamiltonian equal to

$$H_0 = \hbar\omega_c a^\dagger a. \tag{3.31}$$

The new master equation for the interaction picture, reduced density operator $\bar{\sigma}$ is then

$$\begin{aligned}
\frac{\partial\bar{\sigma}}{\partial t} &= i\frac{\delta}{2}[a^\dagger a, \bar{\sigma}] + i\frac{\delta}{2}[(a^\dagger a)^2, \bar{\sigma}] \\
&\quad + \frac{\gamma_c}{2}(2a\bar{\sigma}a^\dagger - a^\dagger a\bar{\sigma} - \bar{\sigma}a^\dagger a) \\
&\quad + \gamma_c\bar{n}(a^\dagger\bar{\sigma}a + a\bar{\sigma}a^\dagger - a^\dagger a\bar{\sigma} - \bar{\sigma}aa^\dagger) \\
&\quad - iv_d(t)[a^\dagger e^{+i\omega_c t}, \bar{\sigma}] - iv_d{}^*(t)[ae^{-i\omega_c t}, \bar{\sigma}],
\end{aligned} \tag{3.32}$$

where all operators other than $\bar{\sigma}$ are still in the Schrödinger picture. This is the equation that has been solved analytically for the special cases of no drive [4, 5, 22, 25] and no anharmonicity [23, 24]. We solve the fully anharmonic, driven case using a Bulirsch-Stöer numerical integration method [28]. (Appendix A gives the energy eigenbasis formulation of Eq. 3.32 used in the calculations and gives details on phase conventions and finite basis effects). The calculation enables us to simulate experimental frequency sweeps as well as less realizable but perhaps more illuminating combinations of initial conditions and system parameters.

3.4 Quantum Monte Carlo Dissipation

Instead of the master equation approach of Sec. 3.3, a Monte Carlo wave-function (MCWF) technique is often used to model dissipative quantum mechanics in atomic systems with a large number of momentum eigenstates, especially for laser cooling and quantum optics [29]. The density operator method requires tracking an $n \times n$ matrix Bloch equation, whereas a wave-function approach only requires evolving an n-dimensional vector. For a large number of basis states, the MCWF approach can save a considerable amount of integration time and/or make unwieldy calculations more tractable. In addition, the MCWF approach helps visualize dissipation as emission and absorption events and may provide a better picture of a single swept cyclotron excitation. For these reasons, and because we wanted to apply the technique to a complex anharmonic oscillator system at nonzero temperature (at the time, it had only been applied to two and three state systems at zero temperature [29]), we adapted the MCWF technique to this calculation. More recently, the formalism has been developed for generalized system Hamiltonians [30–32].

The basic procedure is analogous to the first published two/three state procedure [29]. We solve for the time dependent wave-function by numerically integrating the Schrödinger equation with an effective Hamiltonian that includes an imaginary component for loss. At the beginning of each time step, a random number chooses whether an emission (or absorption) will occur. If so, the wave-function is collapsed with the appropriate measurement operator. We demonstrate both analytically and numerically that if many such trials are averaged together, the density operator master equation results are recovered.

The effective Hamiltonian is taken as

$$H_{\text{eff}} = H_{\text{aho}} + H_{\text{drive}} - i\hbar\frac{\gamma_c}{2}[(\bar{n}+1)a^\dagger a + \bar{n}aa^\dagger], \tag{3.33}$$

where H_{aho} is given in Eq. 3.25 and H_{drive} is given in Eq. 3.18. The state vector is expanded as

$$|\Psi(t)\rangle = \sum_n C_n(t)|n\rangle \tag{3.34}$$

and is initially normalized so that $|C_n|^2 = 1$. Fig. 3.3 shows a schematic diagram of emission and absorption between two Landau levels. In a small time interval dt, the probabilities of emission dp_n and of absorption dq_n between levels n and $n+1$, as shown in the diagram, are given by

$$dp_n(t) = \gamma_c(n+1)dt|C_{n+1}(t)|^2(\bar{n}+1) \tag{3.35}$$

$$dq_n(t) = \gamma_c(n+1)dt|C_n(t)|^2\bar{n}. \tag{3.36}$$

The $\bar{n}$ in the $\bar{n}+1$ factor of dp_n accounts for stimulated emission, whereas the 1 accounts for spontaneous emission. At the start of each time step, a random number decides between three final states. An emission occurs with probability $\sum_n dp_n$, an absorption occurs with probability $\sum_n dq_n$, and normal Schrödinger evolution via the effective Hamiltonian H_{eff} occurs with probability $1 - \sum_n dp_n - \sum_n dq_n$. The time step must be kept short so that the probability of a collapse event is small. It must also be short compared to all other time-scales in the system ($(\sqrt{n}\Omega_R)^{-1}$and $(n\delta)^{-1}$). The resulting state-vectors for the three cases are the superpositions

$$\text{Emission}: \quad |\Psi(t)\rangle \to \sum_n \sqrt{\gamma_c(n+1)dt(\bar{n}+1)}C_{n+1}(t)|n\rangle \tag{3.37}$$

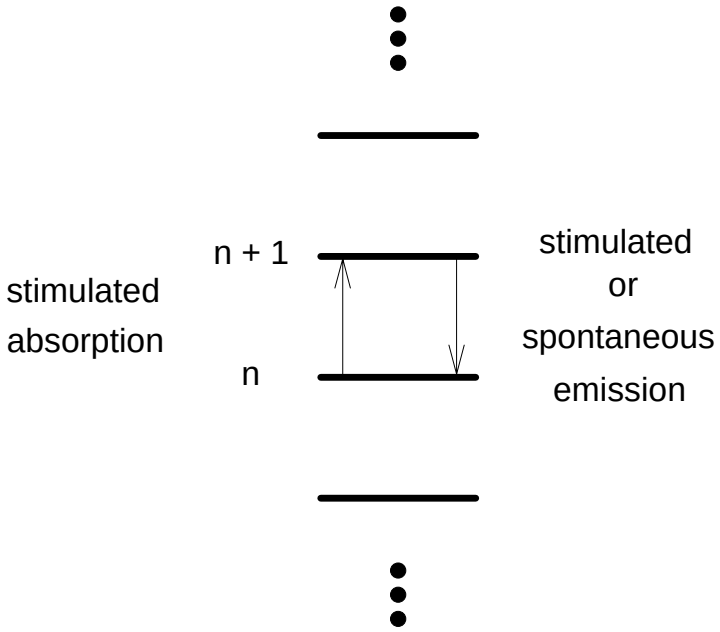

Figure 3.3: Emission and absorption between two Landau levels of the anharmonic cyclotron oscillator. The rates for stimulated emission and absorption are proportional to the thermal excitation $\bar{n}$ of the reservoir, while the rate for spontaneous emission is independent of $\bar{n}$. Rates are given in the text.

$$\text{Absorption}: \quad |\Psi(t)\rangle \rightarrow \sum_n \sqrt{\gamma_c(n+1)dt\bar{n}}C_n(t)|n+1\rangle \tag{3.38}$$

$$\text{Evolution}: \quad |\Psi(t)\rangle \rightarrow \sum_n C_n(t+dt)|n\rangle \tag{3.39}$$

where $C_n(t+dt)$ are the evolved wave function coefficients determined by the Schrödinger equation. The measurement operators used are $\sqrt{\gamma_c dt(\bar{n}+1)}\,a$ for emission and $\sqrt{\gamma_c dt\,\bar{n}}\,a^\dagger$ for absorption. Note that the "measurement" collapses a wavefunction into a superposition state rather than into a single n-level. At the end of each time step, the state-vectors are normalized back to 1.

The square of the norm of each of the three final wave-functions reflects the probability of following that particular path. It is easily seen that the emission wave-function has norm-squared $\sum_n dp_n$ and the absorption wave-function has norm-squared $\sum_n dq_n$. For small time steps, the Schrödinger evolved wave-function can be approximated as $|\Psi(t+dt)\rangle = \left(1 - \frac{i}{\hbar} H_{\text{eff}} dt\right) |\Psi(t)\rangle$, and H_{eff} has been carefully chosen so that the norm-squared of this vector is $1 - \sum_n dp_n - \sum_n dq_n$. An observable $\langle \hat{O} \rangle$ is averaged over an ensemble of N runs with

$$\langle \hat{O} \rangle_{ens}(t) = \frac{1}{N} \sum_{i=1}^{N} \langle \Psi_i(t) | \hat{O} | \Psi_i(t) \rangle. \tag{3.40}$$

3.4.1 Analytical Agreement with the Master Equation

The Monte Carlo procedure outlined above reproduces the master equation of Sec. 3.3 with a derivation analogous to one used for the two-state MCWF procedure in [29]. The density operator for a given trial $\sigma(t+dt) = |\Psi(t+dt)\rangle\langle\Psi(t+dt)|$ is averaged over the three possible outcomes to make the appropriate mixed state, is compared to $\sigma(t)$, and is then ensemble averaged over many trials. The normalized state vectors at time $t + dt$ are similar to those given in Eqs. 3.37 - 3.39 but are multiplied by normalization coefficients μ_1, μ_2, and μ_3 respectively, where

$$\mu_1 = \left(\sum_n dp_n \right)^{-1/2} \tag{3.41}$$

$$\mu_2 = \left(\sum_n dq_n \right)^{-1/2} \tag{3.42}$$

$$\mu_3 = \left(1 - \sum_n dp_n - \sum_n dq_n \right)^{-1/2}. \tag{3.43}$$

Then the mixed state density operator for a given trial, $\sigma_{mix}(t+dt)$, is given by

the probability of each outcome times the density operator for that outcome

$$\begin{aligned}
\sigma_{mix}(t+dt) &= \left(\sum_n dp_n\right) {\mu_1}^2\, \gamma_c(\bar{n}+1)dt\; a\left\{|\Psi(t)\rangle\langle\Psi(t)|\right\} a^\dagger \\
&+ \left(\sum_n dq_n\right) {\mu_2}^2\, \gamma_c\bar{n}dt\; a^\dagger \left\{|\Psi(t)\rangle\langle\Psi(t)|\right\} a \\
&+ \left(1-\sum_n dp_n - \sum_n dq_n\right) {\mu_3}^2 \times \\
&\quad (1-\frac{i}{\hbar}H_{\rm eff}dt)\left\{|\Psi(t)\rangle\langle\Psi(t)|\right\}(1+\frac{i}{\hbar}H_{\rm eff}^\dagger dt), \qquad (3.44)
\end{aligned}$$

where each of the outcome-states at time $t+dt$, prior to normalization, is taken as a collapse operator or propagator times the initial state at time t. The normalization coefficients cancel the probability factors. The bracketed terms are simply density operators at time t for that trial. The expression then reduces to

$$\begin{aligned}
\sigma_{mix}(t+dt) &= \gamma_c(\bar{n}+1)dt\; a\sigma(t)a^\dagger \\
&+ \gamma_c\bar{n}dt\; a^\dagger\sigma(t)a \\
&+ \sigma(t) - \frac{i}{\hbar}dt(H_{\rm eff}\sigma(t) - \sigma(t)H_{\rm eff}^\dagger). \qquad (3.45)
\end{aligned}$$

Finally, taking the ensemble average and the limit of small dt gives the master equation for the averaged density operator $\langle\sigma\rangle_{ens}(t)$

$$\begin{aligned}
\frac{d\langle\sigma\rangle_{ens}}{dt} &= -\frac{i}{\hbar}(H_{\rm eff}\langle\sigma\rangle_{ens} - \langle\sigma\rangle_{ens}H_{\rm eff}^\dagger) \\
&\quad + \gamma_c(\bar{n}+1)a\langle\sigma\rangle_{ens}a^\dagger + \gamma_c\bar{n}a^\dagger\langle\sigma\rangle_{ens}a \qquad (3.46) \\
&= \frac{i}{\hbar}\left[\langle\sigma\rangle_{ens}, H_{\rm aho}+H_{\rm drive}\right] \\
&\quad + \frac{\gamma_c}{2}(2a\langle\sigma\rangle_{ens}a^\dagger - a^\dagger a\langle\sigma\rangle_{ens} - \langle\sigma\rangle_{ens}a^\dagger a) \\
&\quad + \gamma_c\bar{n}(a^\dagger\langle\sigma\rangle_{ens}a + a\langle\sigma\rangle_{ens}a^\dagger - a^\dagger a\langle\sigma\rangle_{ens} - \langle\sigma\rangle_{ens}aa^\dagger) \qquad (3.47)
\end{aligned}$$

where Eq. 3.47 is found using the expression for H_{eff} from Eq. 3.33. The ensemble average master equation in Eq. 3.47 is equivalent to the Schrödinger picture equation given in Eq. 3.29 (ignoring Δ_R).

3.4.2 Choice of Measurement Operators

If we claim that the frequency of an emitted (or absorbed) photon can be resolved so as to distinguish which quantum level has decayed (or absorbed), then the collapse operators $\sqrt{\gamma_c dt(\bar{n}+1)}\,a$ and $\sqrt{\gamma_c dt\,\bar{n}}\,a^\dagger$ need to be adjusted: The outcome-states must be taken as individual n-levels rather than the superposition states given by the simple collapse operators a and $a^\dagger$. This is perhaps necessary for the lowest levels of the anharmonic cyclotron oscillator where the damping widths (γ_cn) are small compared to the frequency shift from one transition to the next (δ). The new collapse operators are $\sqrt{\gamma_c dt(\bar{n}+1)}\,a|n_j\rangle\langle n_j|$ and $\sqrt{\gamma_c dt\,\bar{n}}\,a^\dagger|n_j\rangle\langle n_j|$, where $|n_j\rangle\langle n_j|$ is the projection operator for the Landau level corresponding to a frequency transition ω_j. Using these new collapse operators is equivalent to choosing a reservoir coupling Hamiltonian

$$V = \hbar\sum_j a^\dagger|n_j\rangle\langle n_j|g_j b_j + \hbar\sum_j a|n_j\rangle\langle n_j|g_j^* b_j^\dagger \tag{3.48}$$

instead of the one chosen in Eq. 3.27 of the master equation derivation.

With these frequency resolvable collapse operators, the MCWF procedure reproduces the same master equation as the one given in Eq. 3.46 with one important difference. The damping terms on the second line each have the diagonal density operator $\langle(\sum_n |n\rangle\sigma_{nn}\langle n|)\rangle_{ens}$ in place of the full density operator $\langle\sigma\rangle_{ens}$. The equivalence of these two master equations is established by showing that the off-diagonal density operator elements in the terms $\gamma_c(\bar{n}+1)a\sigma a^\dagger$ and $\gamma_c\bar{n}a^\dagger\sigma a$ do not couple to $d\sigma/dt$. This is argued by Cohen-Tannoudji [33] and labeled the *secular approxima-*

tion. He shows that for a general master equation in a basis of energy eigenstates

$$\frac{d\sigma_{ij}}{dt} = -i\omega_{ij}\sigma_{ij} + \sum_{lm} R_{ijlm}\sigma_{lm}, \tag{3.49}$$

the coupling between σ_{ij} and σ_{lm} is negligible if $|\omega_{ij} - \omega_{lm}| \gg \Gamma$. In this condition, ω_{ij} is the evolution frequency of σ_{ij} in the absence of damping, and Γ gives the order of magnitude of the coupling coefficients R_{ijlm}. For the master equation terms we are considering, the condition roughly reduces to $\delta \gg \gamma_c n$, the same condition used to decide that the frequency of the emitted or absorbed photon is resolvable. Thus using the resolvable frequency collapse operators is equivalent to taking the *secular approximation* and omitting the negligible off-diagonal couplings, but it is not necessary. Such an approximation is useful for simplifying master equation calculations, and for allowing larger time steps in MCWF calculations, but it raises the difficult issue of how to make a transition from resolvable photon frequencies to unresolvable ones as the cyclotron excitation grows. As long as the computer power is available, we choose to solve the more general master equation of Eq. 3.46. Future studies which investigate individual MCWF realizations for the one-electron cyclotron oscillator, however, should explore the differences between the two sets of measurement operators.

3.4.3 Numerical Agreement with the Master Equation

Fig. 3.4a shows how the agreement arises between the solution of the master equation and the quantum Monte Carlo approach. Plotted are undriven exponential decays from $n = 10$ to final excitations of $n = 1$ for a 30-level anharmonic oscillator coupled to a finite temperature reservoir with $\bar{n} = 1$. A solid curve shows the master equation result and fits well to the expected exponential. Monte Carlo calculations

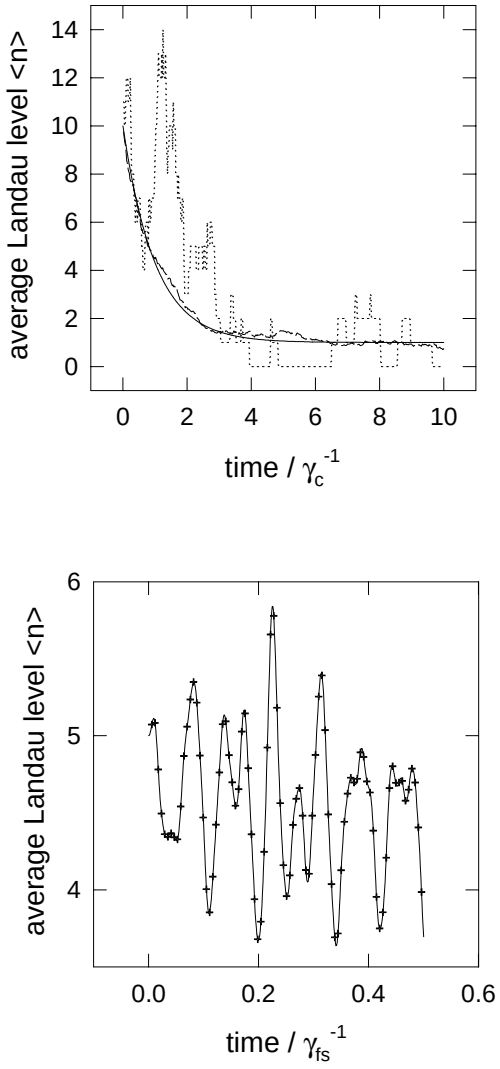

Figure 3.4: Comparisons of the anharmonic oscillator Monte Carlo and master equation solutions for damped but undriven conditions in (a) and for undamped but driven conditions in (b). (a) The master equation solution (solid) is the expected exponential decay to $\langle n \rangle = 1$ for this finite temperature reservoir ($\bar{n} = 1$) case. Monte Carlo calculations for a single realization (dotted) and a 100 trial ensemble average (dashed) approach the master equation solution. (b) Without damping, a single realization of the Monte Carlo (crosses) reproduces the master equation solution (line) for Rabi flopping in the presence of a drive ($\Omega_R/\delta = 1$), and confirms identical drive frequency, power, and phase conventions for the two codes.

for a single realization (dotted) and a 100 trial ensemble average (dashed) approach the master equation solution. (A 1000 realization ensemble average is nearly indistinguishable from the exponential shown.) Fig. 3.4b shows master equation and wave-function Rabi flopping solutions for an undamped 10-level anharmonic oscillator. A single trial of the MCWF code is sufficient for this undamped comparison. The agreement assures that the Rabi frequency and phase conventions for the two codes are identical.

An alternative implementation of the MCWF method using a delay function is analytically shown to be identical to the method described above [31, 34]. Instead of determining the probability of a jump at each time step and then renormalizing, the effective Hamiltonian is evolved until its norm has decayed to an amplitude determined by a single random number. At that point another random number is generated to decide between the two collapse paths, and then the wave-function is renormalized. This method is computationally faster for our system because a Bulirsch-Stöer adaptive step-size routine can integrate quickly through the free evolution time interval, and small steps need only be taken to zero in on the collapse time. Another benefit of the delay function method is that fewer random numbers need to be generated. Both implementations have been used, but future work should make use of the faster delay function procedure. See Appendix A for details on the Schrödinger equation evolution, drive phase conventions, and finite basis effects.

3.5 Classical Correspondence

The classical description was carefully formulated to allow comparisons with the quantum description. In this section we find correspondences between the classical response variable $\bar{\alpha}(t)$ and quantum variables.

Comparing the classical harmonic oscillator energy $E = \hbar\omega_c|\bar{\alpha}|^2$ (first term in Eq. 2.12 ignoring the rest mass), and the quantum harmonic oscillator energy $\langle H_c\rangle = \hbar\omega_c(\langle a^\dagger a\rangle + \frac{1}{2})$ (Eq. 3.7), gives the classical-quantum energy correspondence

$$|\bar{\alpha}|^2 = \langle n\rangle + \frac{1}{2}. \tag{3.50}$$

When $\langle n\rangle$ is large enough, the one-half can be ignored.

Next we relate the classical characterizations of drive strength and anharmonicity

$$|\bar{\alpha}_{\max}|^2 = \left(\frac{2}{\gamma_c}\right)^2 \frac{(eE_0)^2}{2m\hbar\omega_c}\,, \qquad N = -\frac{\omega_c}{\gamma_c}|\bar{\alpha}_{\max}|^2\left(\frac{\hbar\omega_c}{mc^2}\right) \tag{3.51}$$

to the quantum characterizations

$$\Omega_R = \sqrt{\frac{2(eE_0)^2}{m\hbar\omega_c}}\,, \qquad \delta = \omega_c\frac{\hbar\omega_c}{mc^2}. \tag{3.52}$$

We rewrite the classical characterizations in terms of the quantum ones

$$|\bar{\alpha}_{\max}|^2 = \left(\frac{\Omega_R}{\gamma_c}\right)^2\,, \qquad N = -\frac{\delta}{\gamma_c}|\bar{\alpha}_{\max}|^2, \tag{3.53}$$

and remember the energy correspondence gives $|\bar{\alpha}_{\max}|^2 \simeq \langle n_{\max}\rangle$ for large $n_{\max}$. Notice how the maximum energy level is determined by a competition between the drive (Ω_R) and the damping (γ_c). In addition, the anharmonicity parameter N is simply the ratio of the maximum relativistic shift $-\langle n_{\max}\rangle\delta$, and the natural linewidth γ_c.

Next we go back to the steady state equation for $\bar{\alpha}$ (in the rotating frame) to check that both pictures give the same equilibrium energy for a given drive frequency ω_d. Confirming this consistency is vital for setting quantum state energies equal to

the equilibrium levels predicted by the classical equations. Rewriting the classical steady state response of Eq. 2.15 in terms of quantum parameters, we find

$$|\bar{\alpha}_{ss}|^2 \left[\left(\frac{\gamma_c}{\delta} \right)^2 + 4 \left(\frac{\omega_d - \omega_c}{\delta} + |\bar{\alpha}_{ss}|^2 \right)^2 \right] = \left(\frac{\Omega_R}{\delta} \right)^2 . \tag{3.54}$$

For small damping $\gamma_c/\delta \ll 1$ and small Rabi frequency $\Omega_R/\delta \ll 1$ the two stable steady state response energies are $|\bar{\alpha}_{ss}|^2 \simeq 0$ and $|\bar{\alpha}_{ss}|^2 \simeq (\omega_c - \omega_d)/\delta$. The classical excited state energy then corresponds to an average quantum level $\langle n \rangle \simeq \frac{(\omega_c - \delta) - \omega_d}{\delta} + \frac{1}{2}$. This is where the one-half in the energy correspondence equation is necessary.

In this low damping, low drive regime, the quantum two-state model should be valid, and the quantum model predicts an average n-level half way between the two resonant levels. Referring back to Fig. 3.2, we find that the drive frequency ω_d is indeed resonant with the two levels $n = \frac{(\omega_c - \delta) - \omega_d}{\delta}$ and $n = \frac{(\omega_c - \delta) - \omega_d}{\delta} + 1$.

Finally, we would like to compare the classical rotating frame steady state phase ϕ_{ss} found in Eq. 2.17 to a quantum phase variable. We extract a phase parameter from the quantum model by making an analogy to coherent states. We define a c-number $\alpha(t)$ to be the expectation value of the lowering operator a

$$\alpha(t) = \langle a \rangle = Tr(\sigma(t)a) \tag{3.55}$$

where σ is the Schrödinger picture reduced density operator. The classical (rotating frame) steady state phase can then be compared to the phase of the c-number $\bar{\alpha}(t) = \alpha(t)e^{i\omega_d t}$ during the quantum calculation. This serves mainly as a check for factors of π or $\pi/2$ in drive phase conventions.

Chapter 4

Master Equation Solutions, Loss, and Revivals

Now that we have a method for evaluating the master equation, we need to explore the nature of its solutions. This study leads to the discovery and/or confirmation of some surprising phenomena for oscillators whose anharmonicity shift is larger than the damping width at the lowest n-levels, and yet much smaller than the harmonic level spacing. While a simple series of two-state adiabatic passages represents the excitation process quite well, an unexpected amount of instability in the final excited state is exhibited. This instability is quantitatively characterized by determining the lifetime dependencies of resonantly driven excited states. The loss mechanism is interpreted as differential rotation (due to "large" anharmonicity) of the imposed quantum energy level distribution away from the stable phase-space attractor. Time scales for spreading of the quantum distribution are probed by studying the evolution of perturbations of the equilibrium dressed coherent state of the anharmonic oscillator. Classical correspondence to the quantum instability is confirmed using a probability distribution of classical phase-space trajectories, and is contrasted to

the behavior of familiar classical oscillators whose anharmonicity-to-damping ratios are much smaller. Implications of these findings for ppb cyclotron frequency measurements are discussed in the next two chapters.

Solutions to the master equation ensemble average behavior were complex enough to require study before probing individual trials with the Monte Carlo technique. Still, having two codes with two very different algorithms allowed for comparisons to check for minus signs, factors of two, finite basis effects, and other such errors. With damping set to zero, the two codes give identical results with only a single run of the Monte Carlo code. With nonzero damping, however, many MCWF trials needed to be averaged together. Since much of the work was done with a basis of 50 Landau levels, and $100 - 1000$ runs of the MCWF were need to achieve good averaging statistics, the master equation approach was faster. Nevertheless, the integration was time consuming because of the different frequency scales in the problem. The rotating frame removes the fast GHz cyclotron rotation, but the anharmonicity makes each Landau level rotate 180 Hz faster than the level above it. Many such cycles ($\delta/2\pi\gamma_{\rm fs} \simeq 16$) must be integrated per free space damping time. Even when the damping is set to zero, for Rabi frequencies smaller than the anharmonic shift ($\Omega_R/\delta < 1$), many rotation cycles must be integrated per Rabi-flopping period. Most of the runs discussed lasted overnight on a 125 MHz Sun SparcStation20. Some took less time, and some took as long as a week on the faster 175 MHz DEC 3000 (Alpha).

Throughout this chapter, the free space damping rate, $\gamma_{\rm fs}$, is distinguished from the actual cyclotron damping rate, γ_c, since we have the ability to vary γ_c experimentally by tuning the cyclotron frequency relative to Penning trap cavity modes. We mention that the cavity quality factor is not large enough to allow a buildup of radiated photons which can coherently interact with the cyclotron oscillator and

violate the Markoff approximation. When the cyclotron frequency is resonant with a typical cylindrical trap cavity mode, the lifetime for photons to remain in the cavity is on the order of nanoseconds ($\Gamma = \omega_{mode}/Q$, for $\omega_{mode} \approx 2\pi(150\text{ GHz})$ and $Q \approx 1000$), whereas the lifetime for synchrotron radiation is on the order of ten milliseconds ($\gamma_c/\gamma_{\rm fs} \approx 10$) [14]. De-tuning the cyclotron frequency from such a mode reduces both of these rates simultaneously, therefore, even when spontaneous emission is inhibited, synchrotron radiated photons leave the cavity quickly over the time-scale in which they are created.

4.1 Adiabatic Sweep from Ground State

First we investigate frequency sweeps such as those that produced the observed resonance found in Fig. 2.2. Instead of sweeping the drive frequency until the excitation falls to zero, we stop changing the drive frequency at the transition $n = 30 \rightarrow 31$, and then see if the excitation persists. We plot these adiabatic passages as response energy versus time (rather than drive frequency) in order to investigate the stability of the final excitations. The response curves thus rise to the right.

We begin with the case of no damping (γ_c=0) to verify the simple two-state excitation model discussed in Sec. 3.2. Fig. 4.1 plots the average Landau excitation as a function of time, with time scaled by the free space damping time, $\gamma_{\rm fs}^{-1} \simeq 90$ ms (even though this sweep does not include damping). The Rabi frequency is kept small ($\Omega_R/\delta = 0.2$) so the dressed eigenstates are well separated two-state systems. The response grows as expected once the drive frequency reaches the first resonance, and remains stably excited when the sweep is halted.

Fig. 4.2 shows the same sweep for 4 different Landau-Zener parameters. Recall a larger Landau-Zener parameter means a slower sweep speed and $\Gamma_{\rm LZ} \gg \frac{1}{4}$ is required

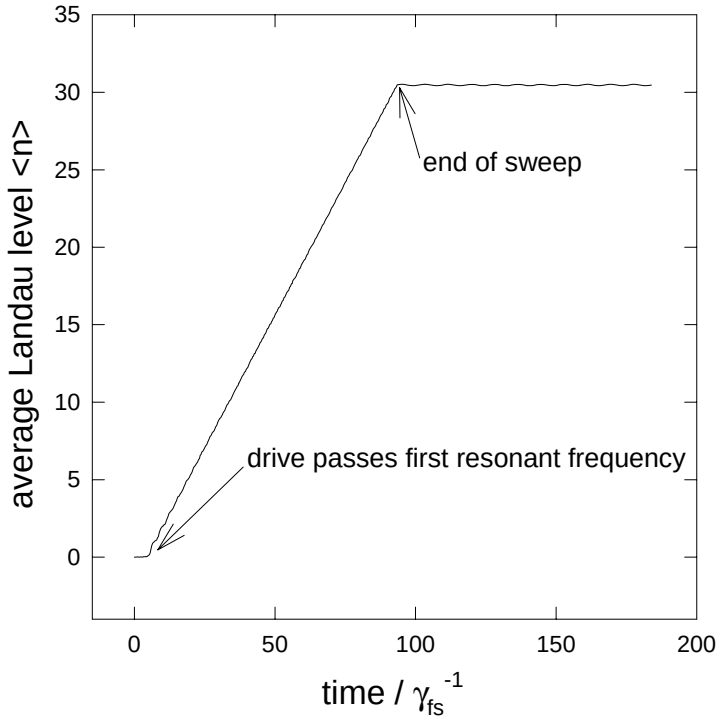

Figure 4.1: Undamped ($\gamma_c = 0$), low power ($\Omega_R/\delta = 0.2$), adiabatic ($\Gamma_{\rm LZ} = 3$) sweep and hold. Drive frequency is swept from above the $1^{\rm st}$ resonant frequency down to the $31^{\rm st}$. Average Landau level is plotted as a function of time. The average n rises and remains stable once the drive frequency stays fixed.

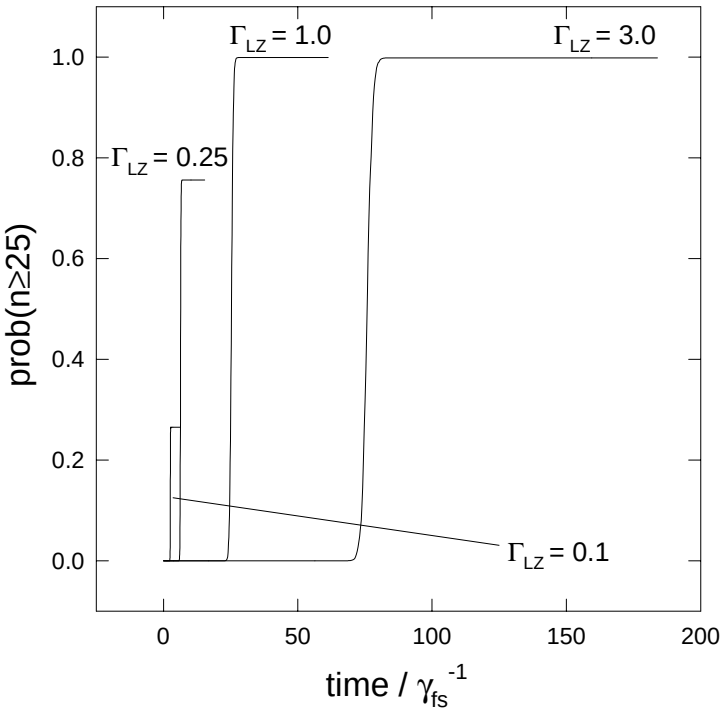

Figure 4.2: Undamped, low power sweeps of Fig. 4.1, using 4 different Landau-Zener parameters. Here the probability for the electron to be in a Landau level greater than or equal to 25 is plotted as a function of time. Fast sweeps (small Landau-Zener parameters) have lower probabilities of inducing excitations.

for adiabaticity. Here the probability for the electron to occupy $n \geq 25$ is plotted rather than average n in order to emphasize the ensemble nature of the problem and to probe the likelihood of obtaining an excitation signal for each sweep speed. The excitation probability drops off rapidly as the Landau-Zener parameter is reduced below 1.

For the final undamped test, Fig. 4.3 shows an adiabatic passage for a much larger Rabi frequency ($\Omega_R/\delta = 5$). Notice the change in scale of the time axis since the higher Rabi frequency enables a much faster adiabatic sweep. Even though the

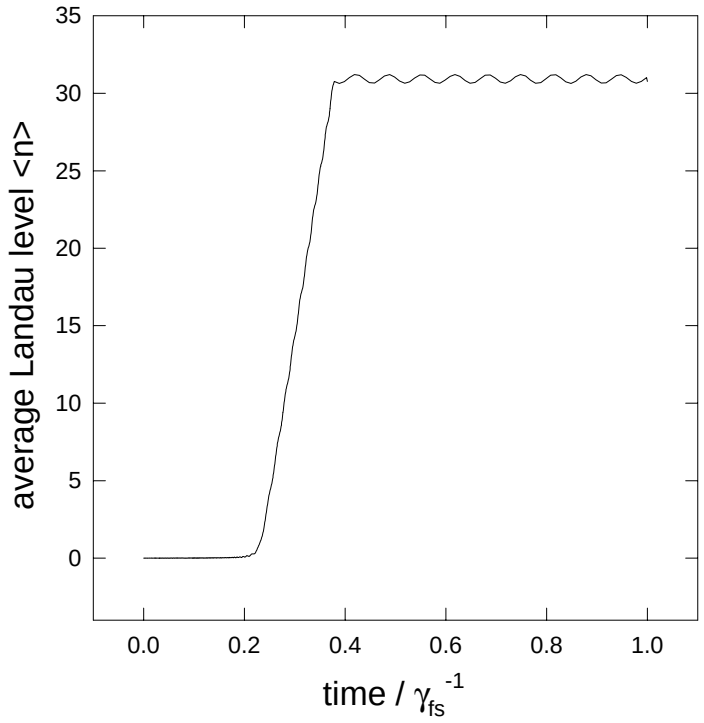

Figure 4.3: Undamped, high power, adiabatic sweep and hold, using the same conditions as Fig. 4.1 but with a Rabi frequency of $\Omega_R/\delta = 5$ rather than $\Omega_R/\delta = 0.2$.

dressed two-state systems overlap at this power level, the sweep is successful and the frequency hold is stable. We can not be too surprised that coherent excitations are possible for overlapping dressed energy levels because we know that a Rabi frequency greater than 3.5δ has successfully produced experimentally observed signals. Unless one imagines that damping in the experiment somehow aids the coherent excitation process, one would be led to believe that undamped sweeps with large Rabi frequencies should certainly be successful. The lower limit $\Omega_R/\delta = 3.5$ on experimental microwave power is obtained by knowing that we have seen a cyclotron excitation as large as $\langle n \rangle = 26,500$ under twice free-space damping conditions [19].

The Rabi frequency is arrived at using Eqs. 3.50 and 3.53, but is only a lower limit since factors other than lack of power may have prevented the excitation process from continuing. (In Sec. 4.4 we will argue that the Rabi frequency must actually have been much larger).

Note the oscillations in the portion of Fig. 4.3 where the drive frequency in no longer being swept. When the sweep is stopped, the electron is not necessarily in a single dressed eigenstate and Rabi flopping results. The actual Rabi oscillations are much faster than the oscillations shown, as they have not been sampled rapidly enough to illustrate the higher frequencies.

We now proceed to investigate the effects of damping on the system. The experimentally relevant question to ask when adding damping is "can an adiabatic passage excite the electron past the 25^{th} level (minimum needed for our detection model) under free space damping conditions with a Rabi frequency that is small enough to achieve the ppb resolution desired?" Fig. 4.4a provides what first seems to be a negative answer. It replots the successful $\Omega_R/\delta = 0.2$ adiabatic passage from Fig. 4.1, and the additional tiny bump shows that free space damping kills the excitation. It was hoped and expected that raising the drive power would eliminate damping loss. Indeed Fig. 4.4b shows a successful excitation with damping for a $\Omega_R/\delta = 5$ adiabatic passage, superimposed on the $\Omega_R/\delta = 5$ sweep of Fig. 4.3. The oscillations, however, obscure any small damping losses. Fig. 4.5 plots results of the same $\Omega_R/\delta = 5$ adiabatic passages in terms of the probability for $n \geq 25$ instead of $\langle n \rangle$. With the oscillations no longer masking the effect, it is evident that the probability of seeing a signal slowly decays away. It is this unexpected loss which is the subject of the next section. The decay could explain why the $\Omega_R/\delta = 0.2$ adiabatic passage was not even able to excite the electron, since that sweep extended over 100 damping times. This instability differs qualitatively from the classical case in which

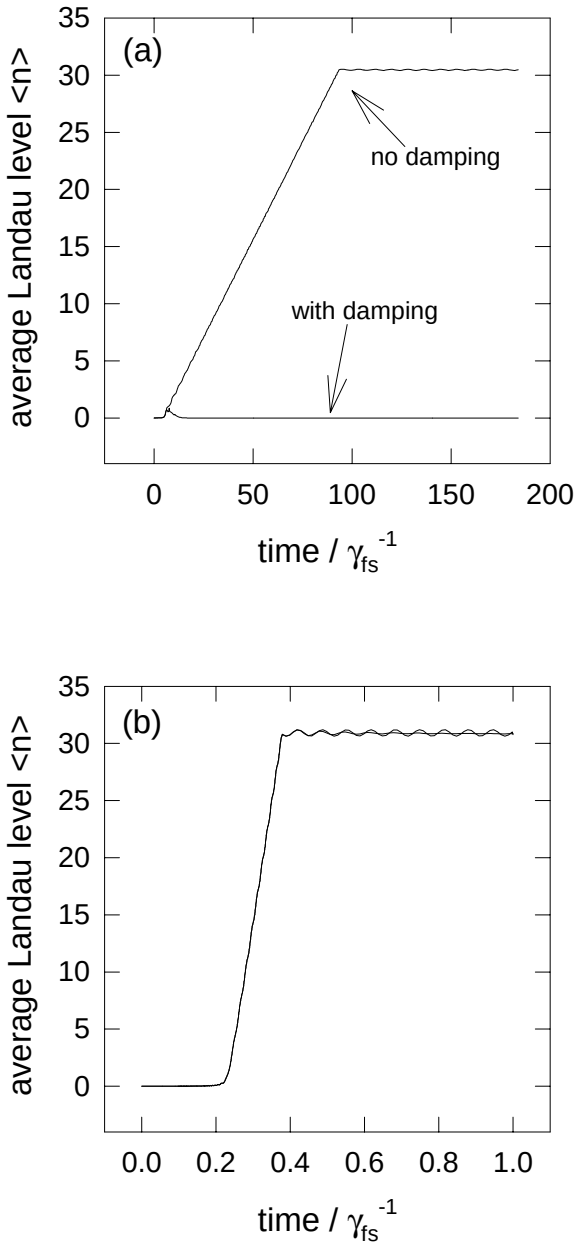

Figure 4.4: Damped versus undamped adiabatic sweep and holds, with a low power (a) and a high power (b) drive. The undamped curves in each plot are identical to those of Figs. 4.1 and 4.3. Damping (at the free space rate) destroys the low power ($\Omega_R/\delta = 0.2$) excitation in (a), but does not seem to hinder the high power ($\Omega_R/\delta = 5$) excitation process in (b).

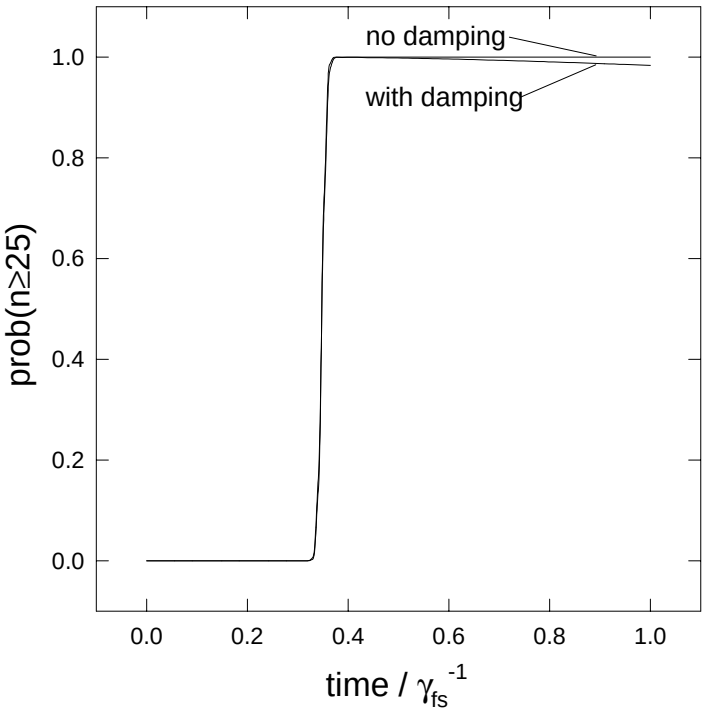

Figure 4.5: Damped versus undamped, high power ($\Omega_R/\delta = 5$), adiabatic sweep and hold, shown here as the probability for the electron to be in a Landau level greater than or equal to 25. The system and sweep parameters used are identical to those of Fig. 4.4b. Free space damping leads to decay of excitation probability from the resonantly driven state.

a driven excitation is indefinitely stable unless some noise source knocks it out of the stable phase-space bucket.

4.2 Loss from a "Classical" Excited State

As discussed in Sec. 2.2, a classical driven anharmonic oscillator has a stable equilibrium excitation. In this section we investigate the decay of excited state probability found in sweeps such as Fig. 4.5 for the quantum oscillator. In an effort to identify

the quantum mechanical origin of loss, we eliminate the complexity of such sweeps and study the fate of a resonantly driven distribution initially in a coherent excited state. Because we do not have an analytical expression for dressed coherent states of the anharmonic oscillator, the electron is started in the closest approximation to such distributions that we can easily manage, a coherent state of the *harmonic* oscillator

$$|\alpha\rangle = e^{-|\alpha|^2/2} \sum_{n=0}^{\infty} \frac{\alpha^n}{\sqrt{n!}} |n\rangle. \tag{4.1}$$

The quantum distribution in phase-space is represented by an interaction picture Q-function,

$$Q(\alpha, \alpha^*, t) = \langle \alpha | \bar{\sigma}(t) | \alpha \rangle, \tag{4.2}$$

where $\bar{\sigma}(t)$ is the interaction picture reduced density operator. Although a harmonic oscillator coherent state distribution can be finely tuned to match the expected (classical) steady state response amplitude and phase, it is not the exact solution to the quantum anharmonic oscillator. Master equation solutions will show, however, that this initial Q-function distribution does rapidly evolve into a characteristic shape which we interpret as a dressed coherent state of the anharmonic oscillator.

In terms of the steady state $\bar{\alpha}_{ss}$ found in Sec. 2.2, the amplitude and phase for the finely tuned α are

$$|\alpha|^2 = \langle n \rangle = |\bar{\alpha}_{ss}|^2 - \frac{1}{2} \tag{4.3}$$

$$\phi_\alpha = \phi_{ss} - \phi_d(0) \tag{4.4}$$

where the convention for the drive's initial phase is $\phi_d(0) = \pi$ (see Appendix A). The phase for α was actually varied to check that it was indeed the correct steady state parameter and was confirmed (to within 10%) to minimize loss from the excited

state. The drive and system parameters are mostly chosen so that the average steady state n-level is much less than $n_{\max}$ and thus located on the right-most wing of the classical resonance curve (see Fig. 2.1), but still in the triple-valued region for such an anharmonic oscillator. Remember for these large detunings, the stable excited state phase lag is near $\phi_{ss} = 3\pi/2$ whereas the unstable phase lag is near $\phi_{ss} = \pi/2$, so the two are separated by 180°. This phase difference is, however, smaller than 180° for the few runs taken with 100 times free-space damping (and thus smaller $n_{\max}$).

Fig. 4.6 shows a typical time series of Q-functions for the damped anharmonic oscillator with a high power ($\Omega_R/\delta \simeq 22$) drive. Q-functions are plotted in a $Re[\alpha]$ versus $Im[\alpha]$ phase-space, with time increasing to the right and then on to the next row, for a total of 5 damping times. Unless otherwise noted, free space damping and zero temperature are assumed. The initial Gaussian coherent state distribution ($\langle n \rangle = 30$), spreads out due to differential rotation rates of the various occupied Landau levels. A steady state configuration is reached very quickly on this time scale and continues to rotate only because the interaction picture is chosen to rotate at frequency ω_c rather than ω_d. In the next section we take a closer look at the early time development as this dressed coherent state configuration emerges. Since the Rabi frequency for this run is very large ($\Omega_R/\delta \simeq 22$), no reduction of excited state probability is evident.

Fig. 4.7 shows a similar time series for a smaller Rabi frequency ($\Omega_R/\delta \simeq 5$). The central ring in the third snapshot shows early loss from the excited state. This is analogous to the loss seen after one damping period in Fig. 4.5. Later time shots show the ring damping to the origin, and still later ones show the loss peak at the center continuing to grow. Comparing with the $\Omega_R/\delta \simeq 22$ time series, it may seem that there is no loss for high enough drive powers, but in fact there is still a very

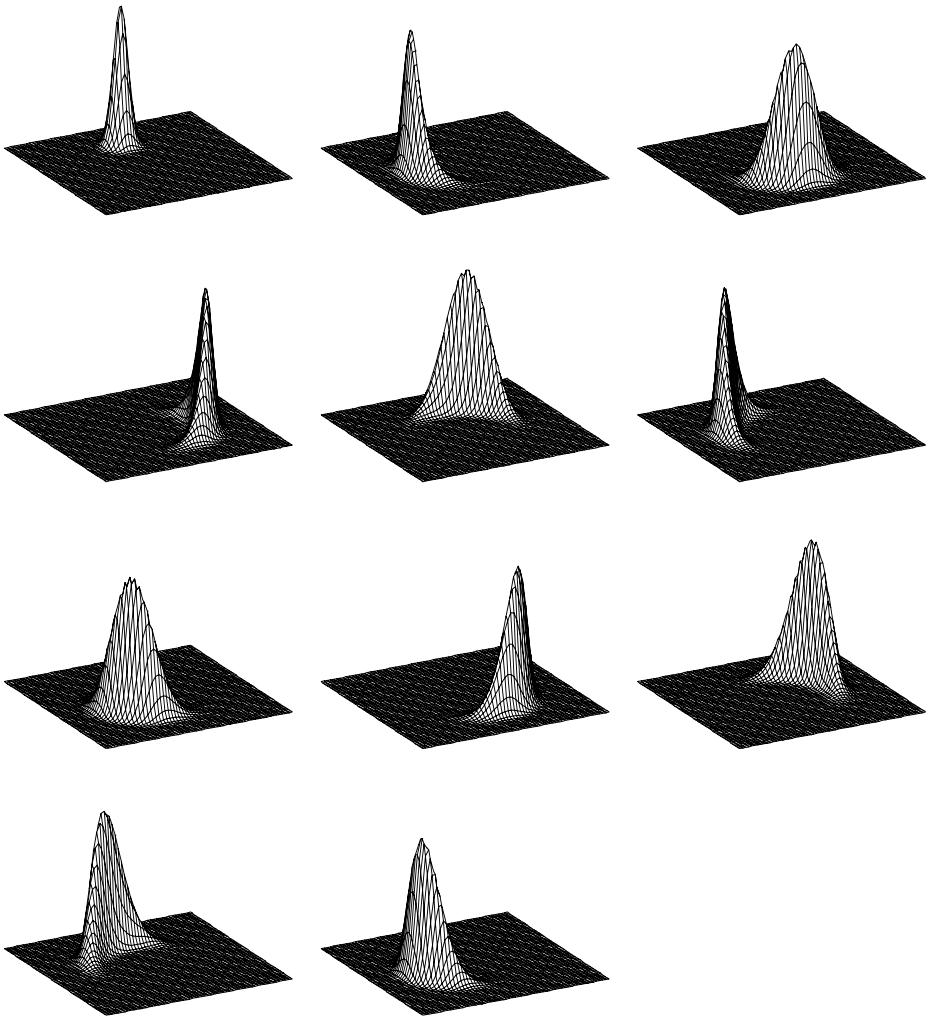

Figure 4.6: The Q-function for a very high Rabi frequency resonantly driven, initially harmonic coherent state excitation: It quickly settles into a dressed state of the anharmonic oscillator, and then continues to rotate at the difference frequency between the drive and the rotating frame, during this 5 damping-time series of equally spaced intervals. Each Q-function Q(α, α^*, t) is plotted in a Re[α] versus Im[α] phase-space. $\Omega_R/\delta \approx 22$, $\gamma_c/\gamma_{\rm fs} = 1$, and initial $\langle n \rangle = 30$.

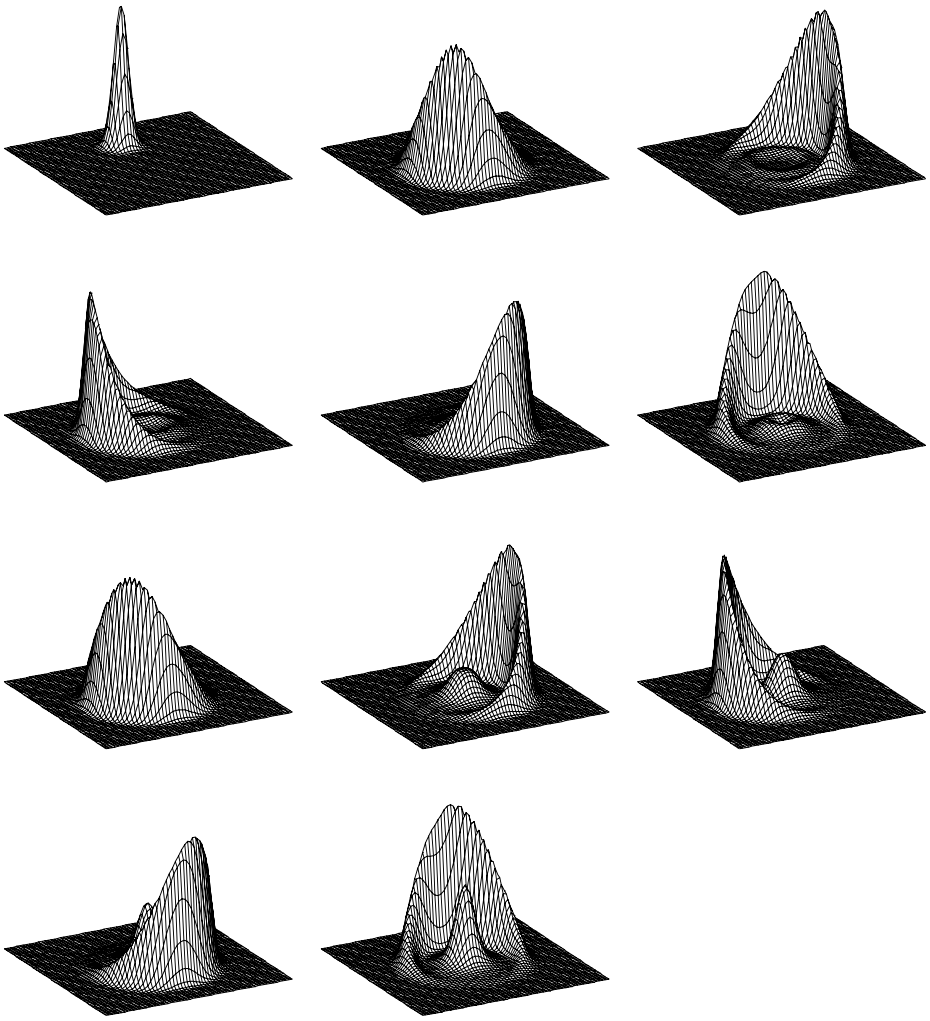

Figure 4.7: A 5 damping-time series of resonantly driven Q-functions for a lower Rabi frequency than that of Fig. 4.6. The Q-function quickly settles into a dressed state configuration and continues to rotate, but a ring of probability lost from the resonant excitation damps to the origin from where it continually grows with time. $\Omega_R/\delta \approx 5$, $\gamma_c/\gamma_{\rm fs} = 1$, and initial $\langle n \rangle = 30$.

slight loss not detectable in the resolution of these plots.

By developing a consistent cutoff scheme which uses the diagonal elements of the density operator to separate the Landau level occupation into an 'excited' part and a 'lost' part, we can quantify the loss-rate ($\Delta P(excited)/P(excited)$) and study what affects it. Fig. 4.8a shows a semi-logarithmic plot of this loss-rate as a function of Rabi frequency for 4 different n-level excitations ranging from 30 to 90. As expected the higher Rabi frequencies lead to dramatically less loss, but completely unexpected is the increase in loss for higher n-levels. Intuition might suggest that higher energy excitations should be more "classical" and therefore more stable, but the opposite is found. The rest of this chapter seeks to explain this divergence from expected classical behavior.

Fig. 4.8b shows loss-rates for the same series of runs plotted against an apparently universal parameter $\frac{\Omega_R/\delta}{\sqrt{n}}$. All loss-rates from Fig. 4.8a are predicted by this combined parameter. Smaller damping rates of $\frac{1}{10}^{\text{th}}$ and $\frac{1}{100}^{\text{th}}$ free-space damping were also tested and fit on the same universal curve (notice the loss-rate is scaled to the damping rate in these plots). Scatter in these plots is expected at the $2-10\%$ level due to imperfect cutoff schemes and loss-rate determinations, but the dependences look convincingly clean over 6 orders of magnitude.

Fig. 4.8c, however, shows system parameter changes which violate the generality of $\frac{\Omega_R/\delta}{\sqrt{n}}$. The "large" damping ($\gamma_c/\gamma_{\text{fs}} = 100$) loss-rate line represents runs for which the damping is large enough so that the excitations are no longer on the wing of the classical resonance curve (but still not large enough to mask anharmonicity since $\gamma_c \sim \delta$). Under these conditions, the stable and unstable steady state phases ϕ_{ss} are no longer $3\pi/2$ and $\pi/2$, but are instead closer than 180° from each other. (Qualitatively, one might expect more loss when the unstable equilibrium, which is on the border of the unstable 'bucket', is closer to the stable excited attractor.)

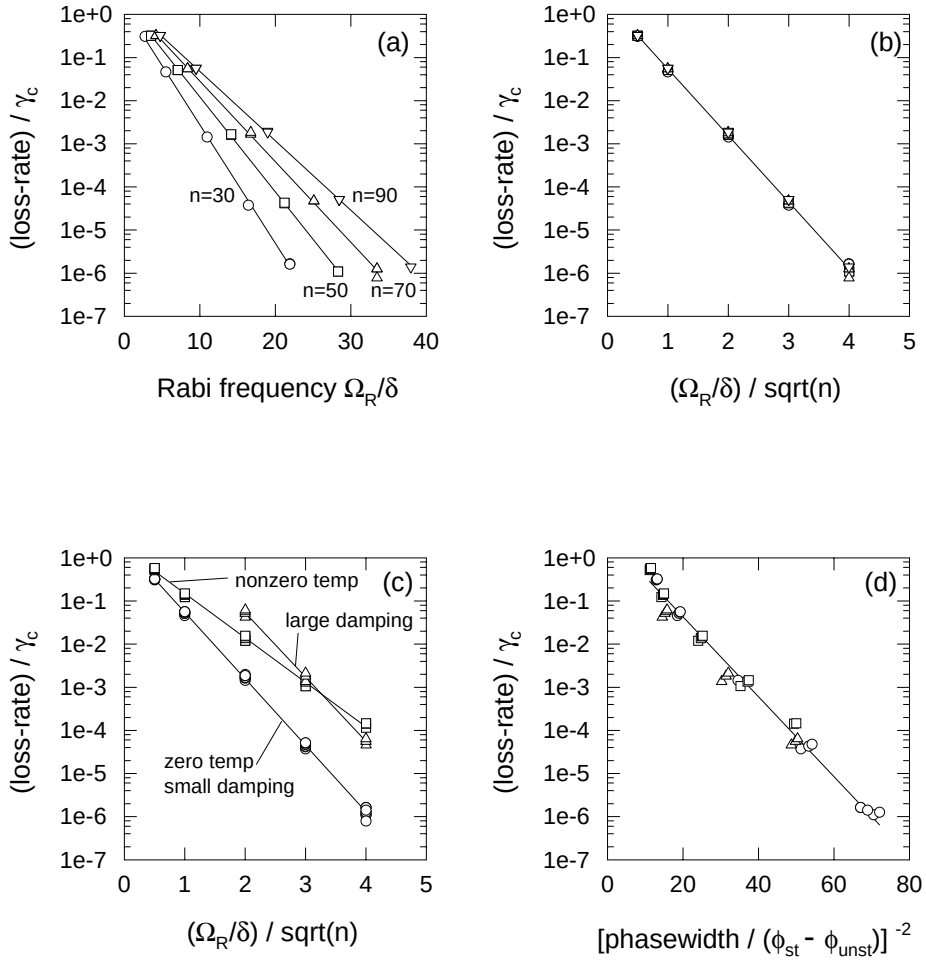

Figure 4.8: Anharmonic oscillator loss-rates (scaled to damping rates), found by measuring the decay of probability from a resonantly excited state, and plotted against a variety of different variables in an effort to determine a universal loss-rate parameter. (a) Loss-rate versus Rabi frequency for 4 different initial $\langle n \rangle$ levels, and free space damping. Smaller damping rates of $\frac{1}{10}^{\text{th}}$ and $\frac{1}{100}^{\text{th}}$ free-space damping were also tested and fall on the same curves. (b) All loss-rates from (a) plotted against a pseudo-universal parameter. (c) Same as (b) but including a set of nonzero temperature runs ($T = 4.2$ K) and a set of "large" damping runs ($\gamma_c/\gamma_{\text{fs}} = 100$). (d) All loss-rates from (c) plotted against a universal parameter. The loss-rate is found to be determined by the excited dressed state Q-function's phasewidth (scaled by the difference between the classical stable and unstable excited steady state phases, which for most cases is just π). Linear regressions (lines) are also shown.

The nonzero-temperature loss-rate line in Fig. 4.8c represents runs for which the reservoir temperature is taken to be $T = 4.2$ K (all previous runs were for zero temperature).

A hint for determining the true universal parameter can be obtained by looking at the final Q-functions for the two evolution series shown in Figs. 4.6 and 4.7. The Q-function with more loss is also much broader in angular spread. It makes some sense that the further the distribution spreads away from the coordinates of the classical stable attractor, the more likely it is for portions of the probability distribution to fall to zero. Plotting loss-rate versus a scaled phasewidth parameter, measured from the final Q-functions for the runs of Fig. 4.8c, indeed gives a true universal curve characterizing loss-rates over 6 orders of magnitude for various n-levels, Rabi frequencies, temperatures and damping rates. Fig. 4.8d shows such a universal plot, combining all three of the loss-rate curves of Fig. 4.8c. The phasewidths must be scaled by the difference between the classical stable and unstable excited-state phases, as given by Eq. 2.17, in order to produce such a universal curve (only necessary for the "large damping" runs which have phase differences other than 180°). This scaling is qualitatively explained by attributing a higher loss-rate (for the same angular distribution Q-function) to conditions where the unstable 'bucket' is closer to the stable excited attractor in phase-space. A phasewidth is measured by taking a slice through a cutoff Q-function (calculated using only the n-levels determined to be in the 'excited' state), at the n-level corresponding to the peak probability, and fitting the slice to a Gaussian phase distribution. Care must be taken to define the peak phase in the center of a $0 \rightarrow 2\pi$ range. Also, while the low-loss runs fit beautifully to Gaussians, the high-loss runs are more difficult. In the next section this process is incorporated into the code to obtain phasewidth information as a function of time, by automating the cutoff procedure and peak

phase determination, and by taking the standard deviation of the distribution rather than fitting.

4.3 Phasewidth of the Dressed Coherent State

Insofar as the loss from an excited dressed state of the anharmonic oscillator is determined by its phasewidth, the question naturally arises as to what determines the steady state phasewidth. The phasewidth $\Delta\Phi$ can be estimated in terms of the quantum uncertainty Δn, as the product of the mean differential rotation frequency $\Delta n\,\delta$ and some spreading time T_{spread} to be determined,

$$\Delta\Phi = (\Delta n\,\delta)T_{\text{spread}}. \tag{4.5}$$

The n-width scales roughly as the coherent state width $\sqrt{n}$. The spreading time can be related to the oscillation period of a perturbation from the (dressed) steady state equilibrium. Our convention of beginning with a harmonic oscillator coherent state serves as this perturbation: The initial localized Gaussian Q-function is, in effect, a phasewidth perturbation on the broad equilibrium distribution. We thus investigate the short time evolution (which was omitted in the last section) from the harmonic oscillator coherent state to the final steady state distribution. These final distributions are the closest possible reproductions of the classical steady state solutions and represent dressed coherent states of the anharmonic oscillator. They are clearly dependent on drive parameters such as drive frequency (which determines $\langle n\rangle$) and Rabi frequency (shown to affect phasewidth) which is why we call them *dressed* coherent states.

First we review the behavior of a Gaussian Q-function when no drive is present.

Such an undriven system has been characterized by Milburn, but for $\delta \ll \gamma_c$ [3, 5]. Fig. 4.9 shows a progression in unequal time steps highlighting the important effects. The times are given in anharmonicity periods $2\pi/\delta$. The second time shot at $t = .03$ shows the initial phase spreading due to differential rotation of the occupied n-levels. Free space damping ($\gamma_{\rm fs} \simeq \delta/100$) is included, but the damping time is roughly 16 anharmonicity time periods and does not have a noticeable effect in this second time shot. The spiral structure is instead an indication that the inner Landau levels are rotating clockwise faster than the outer ones. The next picture at $t = 0.1$ shows coherent interference as the quantum probability distribution wraps around on itself. At $t = 2\pi/\delta$, a revival of the initial coherent state occurs. The revival is not complete as indicated by the ring structure introduced by damping. The next revival at $t = 2$ is even less complete, and by $t = 20$ the quantum coherence is completely destroyed as the average n-level continues to damp exponentially. Revivals can be easily understood in terms a series of differentially rotating particles if one imagines a set of point particles starting at the same phase angle, but at different n-levels. For example, four particles rotating at frequencies 2 Hz, 3 Hz, 4 Hz, and 5 Hz, respectively, all come back to the same phase angle after one second.

In a driven system, the simple analogy to freely rotating particles fails because Rabi flopping between the various n-levels results. Fig. 4.10 illustrates the effect when such a drive is added. The harmonic coherent state spreads but then returns to its initial configuration before having a chance to wrap around on itself. The time series shows two revivals at $\delta t/2\pi \simeq 0.05$ and $\delta t/2\pi \simeq 0.1$ both short compared to an anharmonicity period or a free space damping time. Damping is not included in these runs, as it does not affect the results (as will be shown in Fig. 4.11c). The average n-level (30) and Rabi frequency ($\Omega_R = 4\sqrt{n}\delta \simeq 22\delta$) chosen, however, do affect the revival time and the completeness of revivals. Fig. 4.11 illustrates some

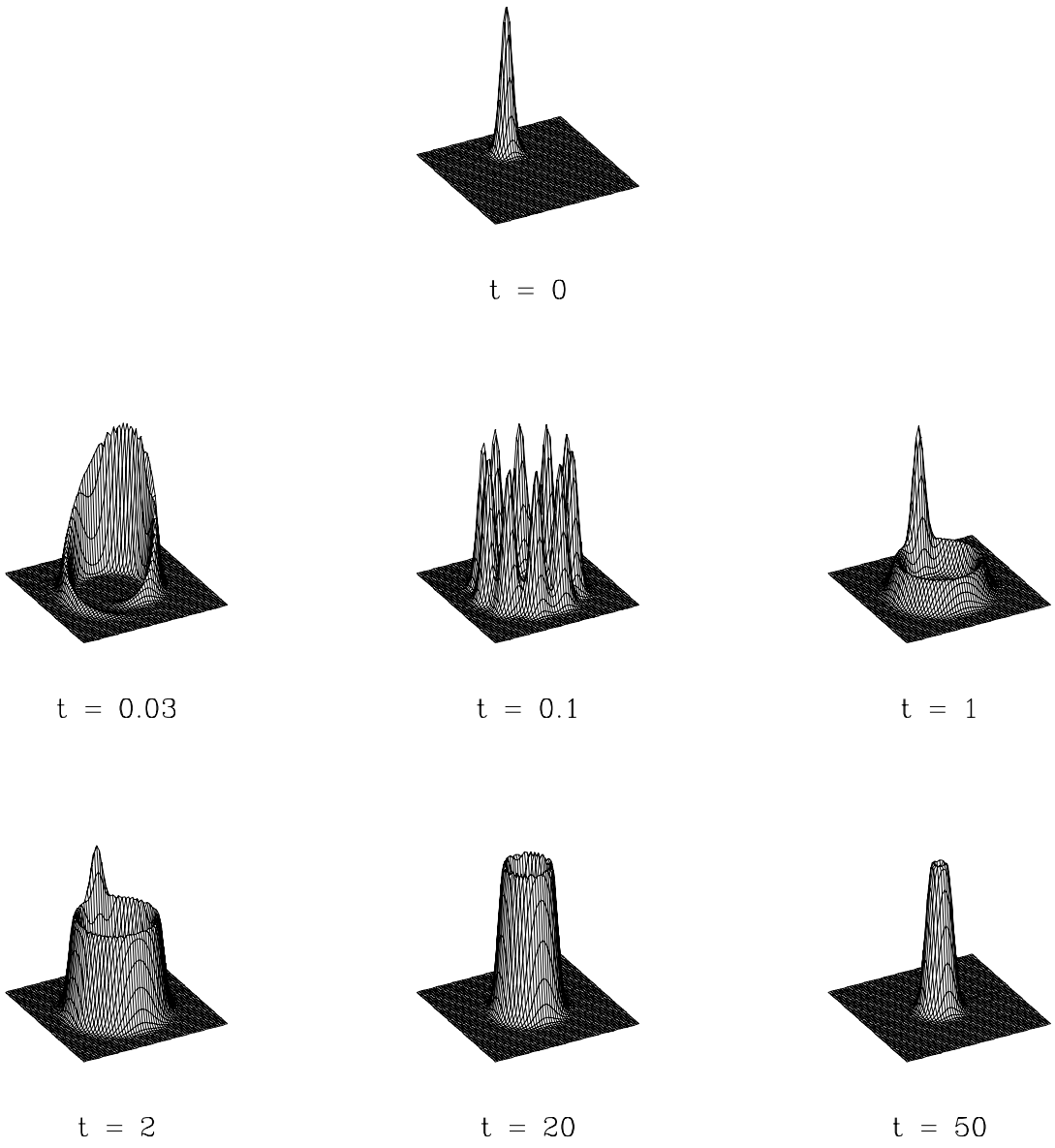

Figure 4.9: Snapshots of time evolution for the Q-function starting in a harmonic coherent state, under the influence of free space damping and without a drive. The initial Gaussian distribution spreads due to anharmonic rotation, wraps around, interferes with itself, and then returns to the initial distribution at the revival time $2\pi/\delta$. A portion of the revival is washed out into a ring due to the presence of damping, even though the time elapsed has only been 0.06 damping times. The next revival is even less complete, until eventually all quantum coherence is lost and the ring structure damps to 0. Initial $\langle n \rangle = 30$. Times are given in units of $2\pi/\delta$.

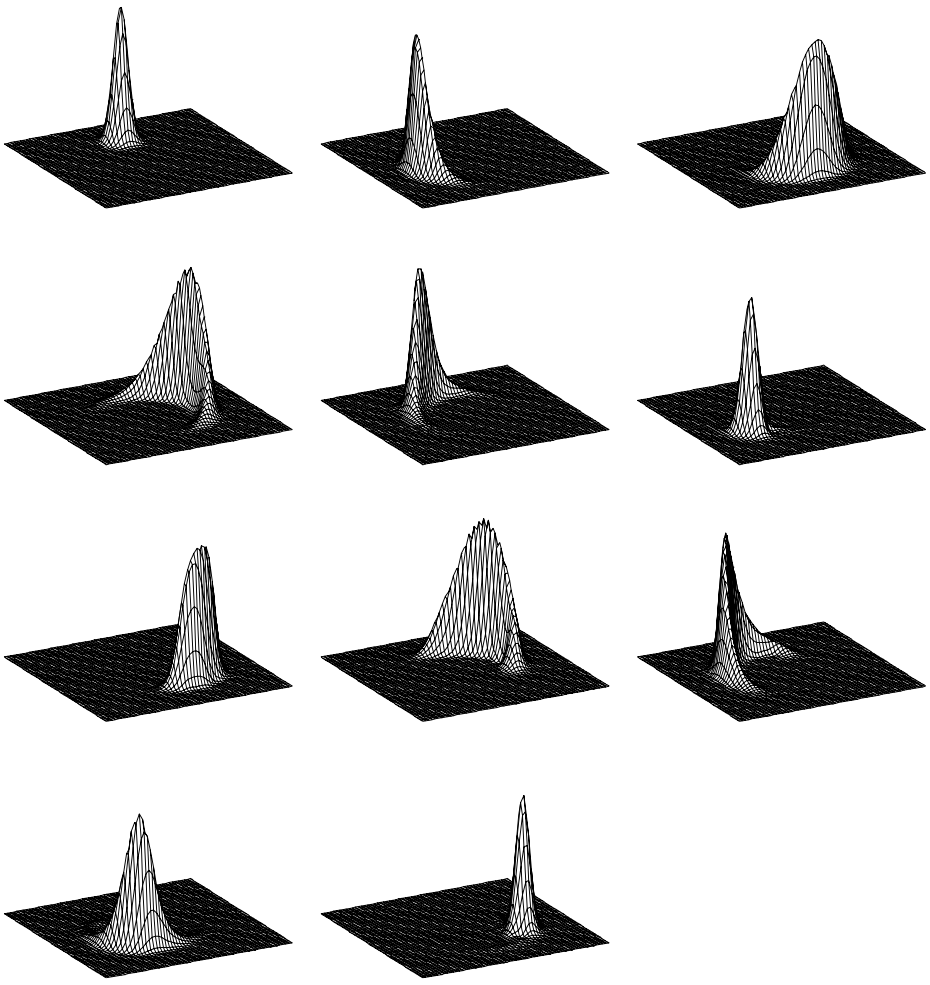

Figure 4.10: The Q-function probability distribution of an initially harmonic coherent state spreads and contracts on a very fast time scale as it evolves into a dressed coherent state of the anharmonic oscillator. Revivals for this driven anharmonic oscillator were not expected. Two revivals are seen during this time series of equally spaced intervals, covering approximately $\frac{1}{10}^{\text{th}}$ of a $2\pi/\delta$ anharmonicity time. Dissipation is not included, as free space damping does not have any effect on this short time scale. Initial $\langle n \rangle = 30$.

of these effects.

Fig. 4.11a shows phasewidth oscillations as the initial distribution spreads and contracts until it settles into a steady state. For a fixed initial Landau level (of 30) these plots show that for higher Rabi frequencies, the phasewidth oscillates more rapidly, revives more completely, and settles into a smaller final value. Fig. 4.11b shows $\langle n \rangle$ oscillations for the same set of parameters. These oscillations have a more complicated structure and were not investigated further. Fig. 4.11c verifies that adding free space damping does not affect the observed phasewidth oscillations (since the time scale is so short compared to a damping time). And finally, Fig. 4.11d shows phasewidth oscillations for various Rabi frequencies and n-levels chosen according to the pseudo-universal loss-rate parameter $(\Omega_R/\delta)/\sqrt{n} = 2$. Notice that the oscillation frequencies are all different, but the equilibrium phasewidths are all the same.

Two phasewidth-related time scales emerge from Fig. 4.11: the oscillation period and the time for relaxation to equilibrium. It is the oscillation period which is needed for the equilibrium phasewidth estimate, as it describes how long the distribution is allowed to spread before contracting. The relaxation time is not investigated further and together with the oscillation time would make the subject of an interesting analytical study. Fig. 4.12 shows that the phasewidth oscillation time (scaled by the time δ^{-1} in calculations) is inversely proportional to the parameter $\sqrt{\Omega_n/\delta}$, where $\Omega_n = \Omega_R\sqrt{n}$ is the Rabi frequency for the n^{th} two-state transition. The spread time of interest then has dependence

$$T_{\text{spread}} \propto \frac{1}{\sqrt{\Omega_R\sqrt{n}\delta}} \tag{4.6}$$

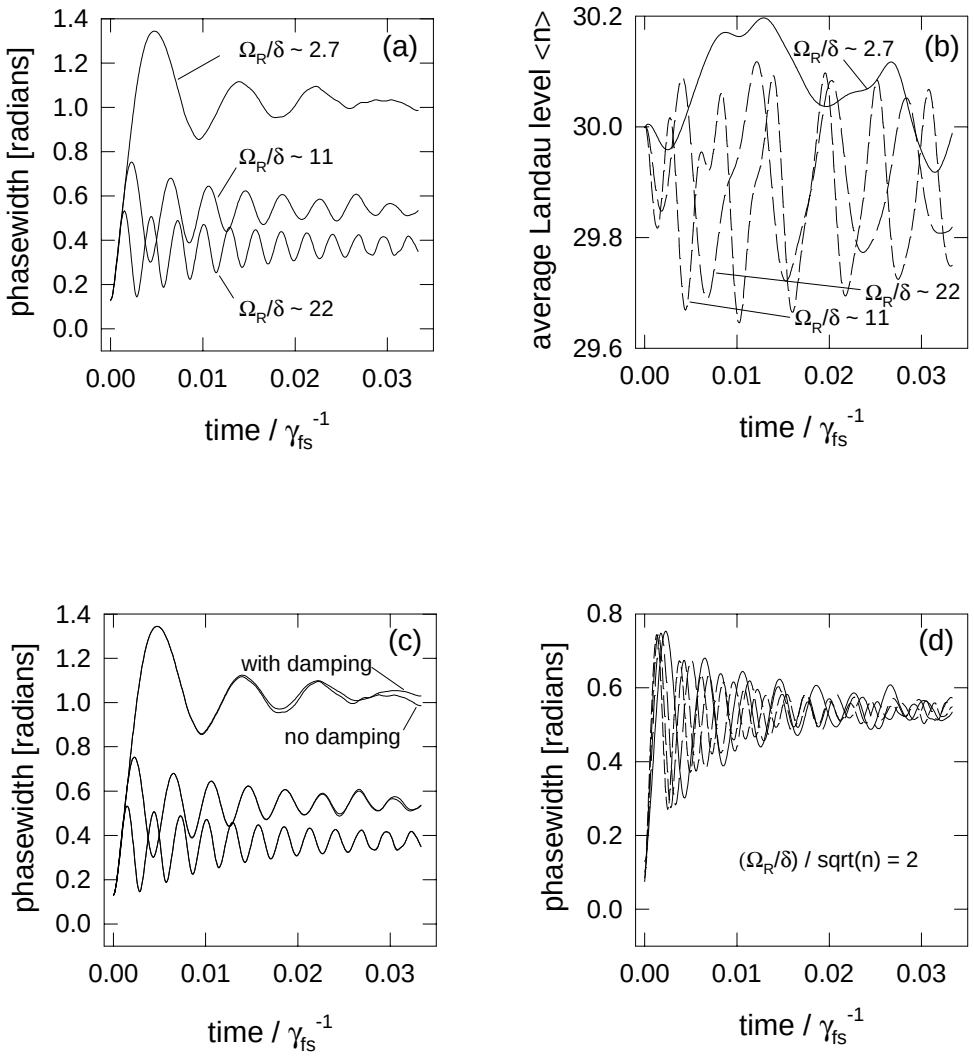

Figure 4.11: Oscillations of the Q-function phasewidth in (a,c and d) and of the average Landau level in (b) as an initially harmonic coherent state evolves into a dressed coherent state of the anharmonic oscillator. (a) Phasewidth oscillates more rapidly, revives more completely and settles into a smaller final value for larger Rabi frequencies (initial $\langle n \rangle = 30$). (b) Average n-level oscillations for the same Rabi frequencies as (a) have a more complicated structure and were not investigated further. (c) Free space damping has negligible effect on the phasewidth oscillations of (a). (d) Phasewidth oscillations for $\langle n \rangle = 30$, 50, 70, and 90, all with $\frac{\Omega_R/\delta}{\sqrt{n}} = 2$, show different revival frequencies but settle into the same steady state phasewidth. No damping is included in (a,b, or d).

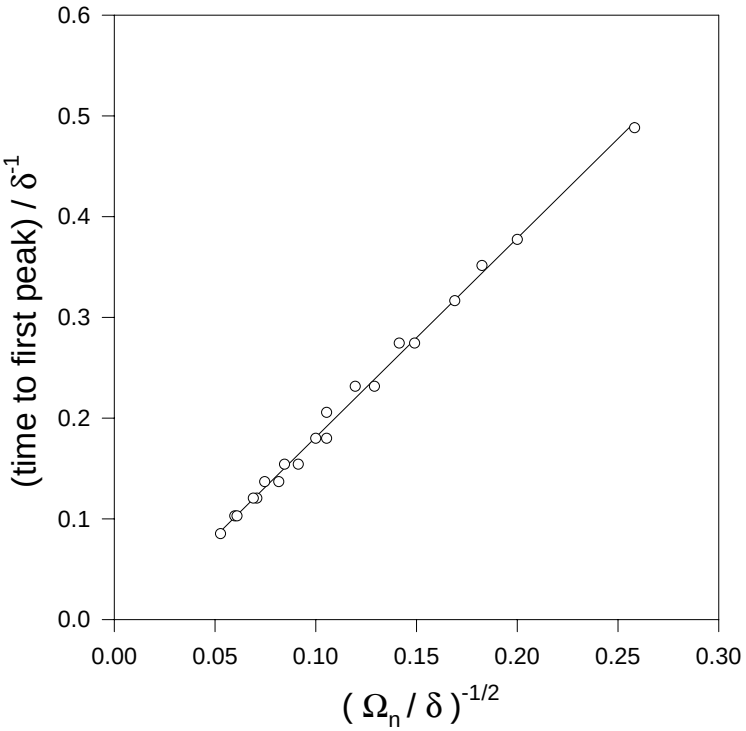

Figure 4.12: The dependence of Rabi frequency and initial $\langle n \rangle$ on the phasewidth spreading time is found by plotting the time to the 1st peak for oscillations (such as shown in Fig. 4.11a) versus the combined parameter which gives a linear relationship. Calculated peak times plotted (circles) are scaled by δ^{-1} and the combined parameter found is $(\Omega_n/\delta)^{-1/2} = (\Omega_R\sqrt{n}/\delta)^{-1/2}$. Since the calculated times are scaled by δ^{-1}, the resulting spreading time is $T_{spread} \propto (\Omega_R\sqrt{n}\delta)^{-1/2}$. A linear regression (line) is also shown.

and consequently the phasewidth estimate has dependence

$$(\Delta\Phi)^{-2} \propto \frac{\Omega_R/\delta}{\Delta n}\frac{\sqrt{n}}{\Delta n}. \tag{4.7}$$

The universal loss-rate parameter was determined in Sec. 4.2 to be the inverse squared phasewidth (scaled by the difference between the stable and unstable excited-state phases). Thus, the right hand side of Eq. 4.7 should be a good estimate for loss-rate. Fig. 4.13 confirms that this calculated parameter is a good predictor of the loss-rate for the same variety of n-levels, Rabi frequencies, temperatures and damping rates represented in Fig. 4.8d, when scaled with the same phase-difference method. Notice that the right hand side of Eq. 4.7 reduces to the pseudo-universal loss-rate parameter found earlier $\frac{\Omega_R/\delta}{\sqrt{n}}$ when the n-width is taken as the coherent state width $\sqrt{n}$.

4.4 Implications of Quantum Instability and the Classical Limit

We summarize the loss mechanism as follows. Quantum mechanics introduces a spread of energy levels into the electron probability distribution, as described by the Heisenberg uncertainty principle. Anharmonicity causes differential rotation of the phases of these levels. The maximum spread of this phasewidth depends on the time scale over which spreading occurs. This time scale, in turn, is limited for higher Rabi frequencies, presumably because the n-levels are mixed more rapidly. Spreading away from the stable attractor leads to loss.

The most surprising result is that higher energy excitations exhibit more loss. In fact, for a particular Rabi frequency and damping rate, a driven excitation only

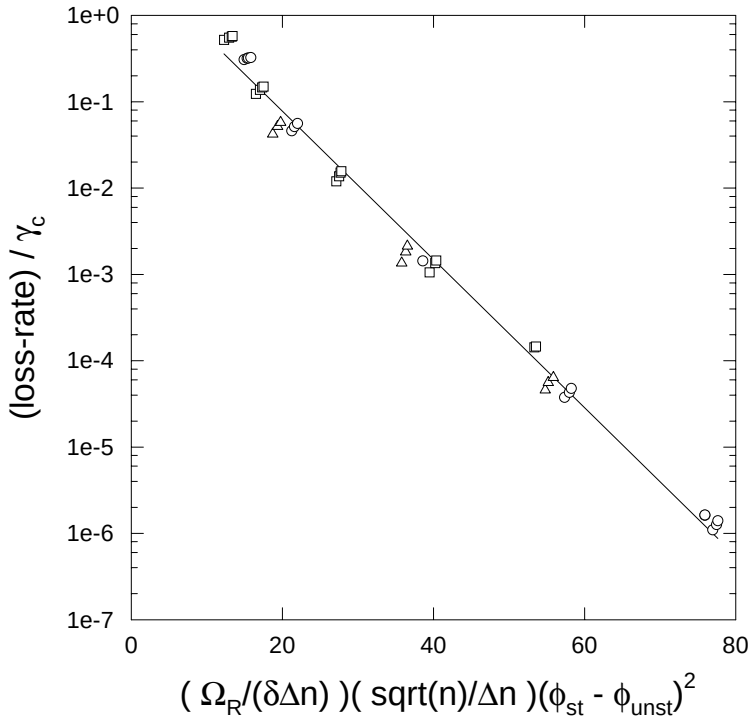

Figure 4.13: Loss-rates for resonant excitations (from Fig. 4.8d) plotted versus the calculated inverse-squared phasewidth given in Eq. 4.7. The calculated phasewidth is scaled by the difference between the classical stable and unstable excited-state phases given by equation Eq. 2.17. (This scaling is only necessary for the set of runs using large damping, $\gamma_c/\gamma_{\rm fs} = 100$, for which $\phi_{st} - \phi_{unst}$ is not equal to π.) A linear regression (line) is also shown.

has a long enough lifetime to be considered stable for the low energy portion of the corresponding classical response curve (see Fig. 2.1). If we use the pseudo-universal loss-rate parameter of Sec. 4.2, we find the condition

$$\frac{\Omega_R/\delta}{\sqrt{n_{\max}}} \gg 1 \tag{4.8}$$

or equivalently,

$$\Omega_{n_{\max}} \gg n_{\max}\delta \tag{4.9}$$

must be satisfied for stability of n-levels all the way up to $n_{\max}$. Substituting in $n_{\max} \simeq (\Omega_R/\gamma_c)^2$, the stability condition becomes

$$\delta \ll \gamma_c. \tag{4.10}$$

In other words, the anharmonic shift ($n\,\delta$) must be masked by the damping width (γ_c) at the lowest Landau levels in order to reproduce a classical response curve. Familiar classical oscillators and pendula always satisfy this condition. Perhaps one would go so far as to say that this restriction is a requirement for classical oscillators. As already mentioned, however, the one-electron cyclotron oscillator is very anharmonic relative to damping and would never be considered classical with that definition. It seems that the one-electron cyclotron oscillator's "large" anharmonicity exaggerates what are normally minute quantum fluctuations enough to knock even a highly excited particle out of its stable phase space bucket.

The stability condition of Eq. 4.8 is necessary but not sufficient for average excitations near $n = n_{\max}$. The more stringent condition found is that the phasewidth must be small compared to the difference between the stable and unstable steady state phases. We thus use the approximate, but scaled, universal loss-rate parameter

to get a more stringent stability condition

$$\frac{\Omega_R/\delta}{\sqrt{n_{\max}}} \gg |\phi_{\rm st} - \phi_{\rm unst}|^{-2}. \tag{4.11}$$

The phase-difference, for $n \approx n_{\max}$, can be approximated as

$$|\phi_{\rm st} - \phi_{\rm unst}|^2 = 4\frac{n_{\max} - n}{n}, \tag{4.12}$$

and the more stringent stability condition becomes

$$\delta \ll \gamma_c(4\frac{n_{\max} - n}{n}). \tag{4.13}$$

The anharmonicity needs to be even smaller than γ_c to maintain stability all the way up to $n_{\max}$. Another way of viewing this condition is that the closer one expects n to get to the top of the classical resonance curve at $n_{\max}$, the smaller the anharmonicity-to-damping ratio δ/γ_c needs to be. This analysis is somewhat speculative in that most of the parameter space investigated was for $n \ll n_{\max}$. Only the few runs with $\gamma_c/\gamma_{\rm fs} = 100$ investigated loss rates for n-levels closer to $n_{\max}$. Still, it seems to indicate that experimental observations of one-electron cyclotron excitations (such as in Fig. 2.2) have been limited in extent by quantum instability rather than by microwave power.

A correspondence check is performed by evolving a *classical* distribution of probability surrounding the stable phase-space attractor (equivalent to the Gaussian coherent state distribution for $\langle n \rangle = 50$) and seeing whether some of the initial points damp to the unexcited attractor at the origin. Indeed they do, as shown in Fig. 4.14. A snapshot of the initial distribution is plotted in crosses. After one damping time, another snapshot (circles) shows that the distribution is split into an 'excited'

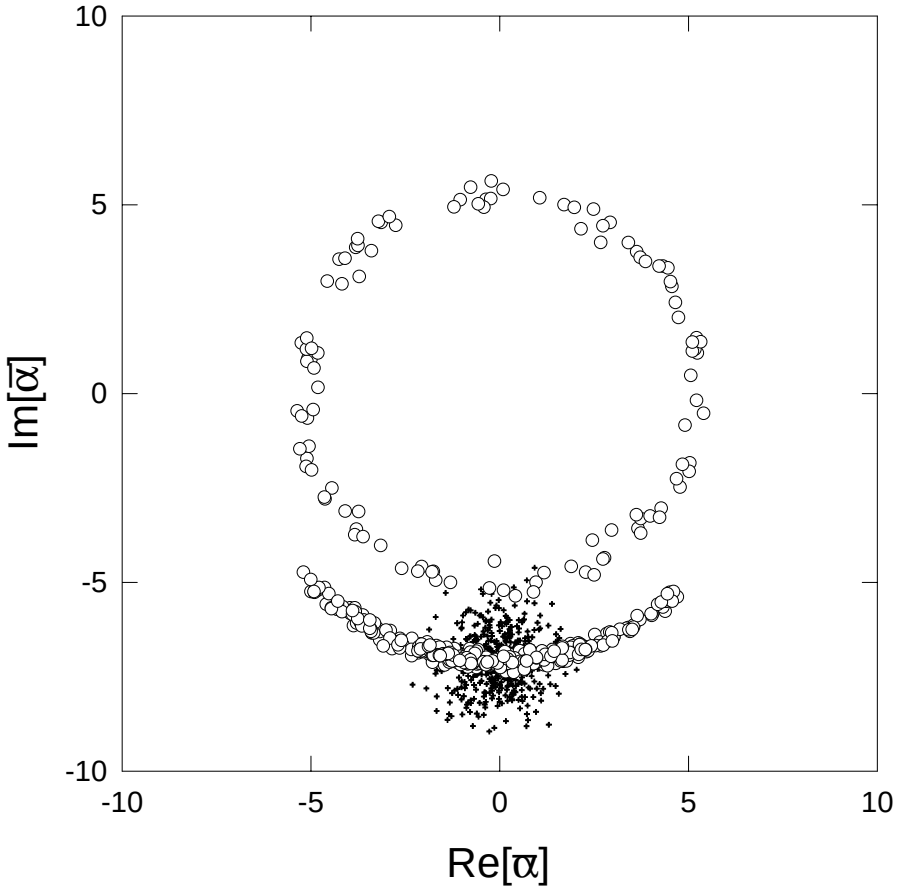

Figure 4.14: The evolution of a *classical* (Gaussian) distribution in phase-space for a driven, free-space damped, anharmonic oscillator governed by the equation of motion in Eq. 2.9 also exhibits loss. The initial distribution (crosses) separates into two pieces (circles) after 1 damping time. In later snapshots (not shown), the ring of circles continues to damp to smaller amplitude, while the crescent of circles continues to damp to the stable excited state. Drive parameters chosen give a steady state amplitude corresponding to the quantum $\langle n \rangle = 50$. A Rabi frequency of $\Omega_R/\delta \approx 3.5$ is chosen from $\frac{\Omega_R/\delta}{\sqrt{n}} = 0.5$. See Fig. 4.15 for a picture of the excited-state's stable bucket.

crescent and a 'lost' ring, just as in the master equation solutions. In later time shots (not shown) the crescent continues to damp to the excited attractor, and the ring continues to damp to the origin. Thus the typical $n \gg 1$ is still a possible classical limit to the quantum system in the sense that the same loss behavior is exhibited for identical initial distributions.

Finally, to picture how this phase spreading can lead to loss of probability in the excited state, Fig. 4.15 shows a contour plot of a Q-function after one damping time of evolution from a coherent state, for the high loss parameter $\frac{\Omega_R/\delta}{\sqrt{n}} = 0.5$ (taking $n = 50$), superimposed on a classical calculation of the excited-state's stable phase-space bucket. Note there is only enough resolution in the bucket sampling to distinguish the first few inner spirals (which appear much darker than the rest of the stable bucket simply because of the higher density of points). All other structures such as the outer lying ovals are mere artifacts from insufficient resolution. The Q-function contour clearly extends beyond the thick first spiral of the classical bucket. It may not be obvious that phase spreading should cause more loss than radial spreading, but it is clear that the first spiral gets much narrower at phases far from that of the excited attractor (at $3\pi/2$).

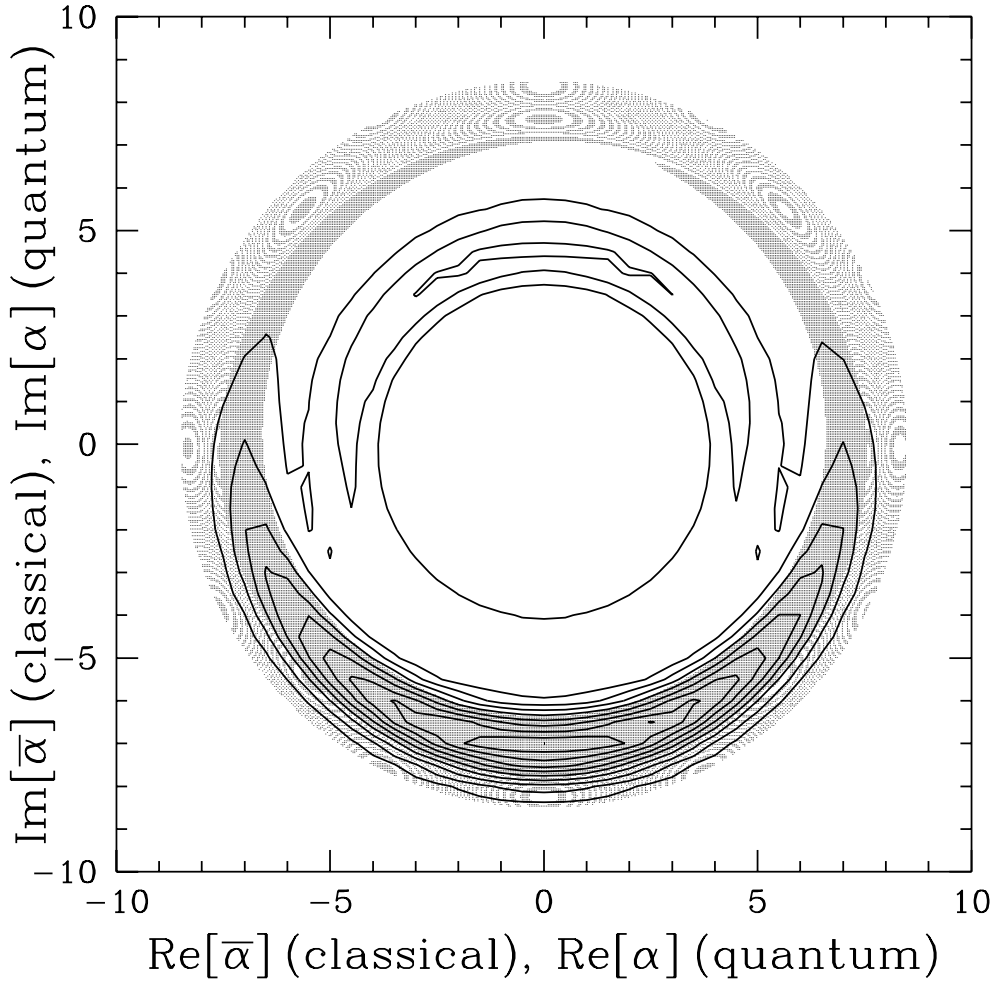

Figure 4.15: Q-function contours (lines) of an unstable anharmonic oscillator after evolving 1 damping time from an initial harmonic coherent state, under the same drive and damping parameters used in Fig. 4.14. The contours reflect a similar distribution to the evolved classical distribution shown in Fig. 4.14, consisting an 'excited' crescent and a 'lost' central ring. Contours are superimposed on a map of the the classical phase-space excited-state bucket (finely spaced dots). The first few (inner) spirals of the bucket are detectable, but the outer regions of the phase-space map do not have enough resolution to resolve the spiral structure (oval structures are artifacts). In addition, the inner spiral appears darker than the rest of the stable bucket due to the higher density of phase-space points in this region. The central region (blank, except for the Q-function 'lost' contours) all belongs to the unexcited-state's bucket. See Fig. 2.3 for a more resolved phase-space map with less anharmonicity and a higher $|\bar{\alpha}_{ss}|^2/|\bar{\alpha}_{\max}|^2$ ratio.

Chapter 5

Possibilities for ppb Frequency Measurements

5.1 Excitation and Detection

An understanding of loss and stability makes it possible to evaluate the feasibility of 1 ppb measurements of the cyclotron frequency, required for the next generation of electron magnetic moment measurements. As discussed in Sec. 3.1, the cyclotron frequency, ω_c, and the anomaly frequency, $\omega_a = \omega_s - \omega_c$, need be measured. Since an anomaly transition is a simultaneous spin flip and cyclotron transition, and since the spin motion has a near infinite lifetime, anomaly transitions can be detected after the fact by simply measuring whether a spin flip has occured. We investigate the possibility of using the cyclotron ladder as a probe of the spin state in the following manner: Referring back to the cyclotron-spin energy level diagram shown in Fig. 3.1, one sees that a spin flip can be identified by detecting a one δ (1 ppb) shift in the $n = 0 \rightarrow 1$ cyclotron transition ($\omega_{0\rightarrow 1}$), between $\omega_c - \delta/2$ and $\omega_c - 3\delta/2$.

The cyclotron energy is experimentally detected as a shift in the axial fre-

quency [1]. Without adding an inhomogeneous magnetic field, the coupling arises only from special relativity and is quite small. Consequently, a transition of one cyclotron energy level causes an axial frequency shift which is too small to be detected directly. We must therefore rely on detection of large cyclotron excitations above some threshold to probe the $n = 0 \rightarrow 1$ transition. Insofar as a 50 level cyclotron excitation corresponds to an easily measurable 2 Hz axial shift, we choose $n = 50$ as a reasonable detection threshold for this study.

We consider two possible excitation methods which allow the detection of $n \geq 50$ to reveal the $n = 0 \rightarrow 1$ transition frequency. Both methods provide $\omega_{0\rightarrow 1}$ frequency information by recording the excitation probability as a function of start frequency for a microwave drive whose frequency is varied with time. The two excitation processes considered are adiabatic passage (as introduced in Chs. 3 and 4) and series of π-pulses. In this chapter we describe and highlight the advantages of each technique, while in the next chapter we illustrate the effect of noise using adiabatic passage.

Slowly sweeping the drive frequency results in a series of adiabatic two-state passages. Consider an electron cyclotron oscillator in its ground state. As the drive is swept from high frequency to low, it first passes the $n = 0 \rightarrow 1$ transition frequency, and the electron moves to the $n = 1$ state. As the sweep continues, the $1 \rightarrow 2$ resonance is passed, causing a transition to $n = 2$ and so on. In this way, the cyclotron motion can be excited to high Landau levels. The large observed excitation is a binary signal that indicates only whether an excitation process was successful or not. The frequency resolution comes from knowledge of the drive's start frequency for a given sweep. Clearly if we sweep the frequency of a weak drive downward, starting below the $0 \rightarrow 1$ resonant frequency, the drive never passes the first resonance, and the electron remains in the ground state. By plotting

probability of excitation versus start frequency, we see the probability change from 0 to 1 when the drive's start frequency is near $\omega_{0\to1}$. The width and offset of such a probability resonance depend somewhat on drive power, but for small Rabi frequencies ($\Omega_R/\delta \leq 1$) we show that the desired ppb resolution can be achieved.

For small Rabi frequencies, spontaneous emission is a problem, and speed of excitation and detection are of utmost importance. Sweep speed is described by the chosen Rabi frequency Ω_R and the Landau-Zener parameter $\Gamma_{\rm LZ}$ (both for the ground state transition),

$$\frac{d\omega_d}{dt} = -\frac{\Omega_R^2}{4\Gamma_{\rm LZ}}, \tag{5.1}$$

where $\Gamma_{\rm LZ} \gg \frac{1}{4}$ is required for adiabaticity. The fixed-speed sweep becomes more and more adiabatic as the two-state Rabi frequency grows with n-level ($\Omega_n = \Omega_R\sqrt{n}$). An experimental way to speed the excitation process, while remaining in the adiabatic regime, is to increase the sweep speed as the cyclotron energy grows, but in this study, the simple fixed-speed case is examined.

The other excitation process considered is a series of π-pulses. A π-pulse for a two-state system is an application of a resonant drive for the exact amount of time necessary to transfer all the population from one state to the other. A series of such pulses, with successive pulse frequencies decreased by δ and the $n^{\rm th}$ pulse duration decreased by the factor $\sqrt{n}$, can also produce a large cyclotron excitation. Again, a resonance curve can be generated by starting the π-pulse sequences at different frequencies surrounding the true ground state frequency, and determining the excitation probability for each.

The adiabatic sweep may be easier to perform experimentally, but it is slower than the π-pulse method for the smallest Rabi frequencies. The time needed per

level of excitation for each of the two methods is

$$\tau_{\text{sweep}} = \frac{4\Gamma_{\text{LZ}}}{(\Omega_R/\delta)^2}\frac{1}{\delta} \tag{5.2}$$

$$\tau_{\text{pi}} = \frac{\pi}{(\Omega_R/\delta)\sqrt{n}}\frac{1}{\delta}. \tag{5.3}$$

Each π-pulse is faster than the corresponding two-state sweep when the condition

$$\frac{\Gamma_{\text{LZ}}}{\Omega_R/\delta} > \frac{\pi}{4} \tag{5.4}$$

is satisfied. Thus, for Rabi frequencies much less than δ, the π-pulse method is faster than the adiabatic sweep. It will be shown, in fact, that the π-pulse method is most useful for these lowest Rabi frequencies, since for higher power drives, multiple resonance peaks get broadened together to reduce the frequency resolution.

The calculated frequency sweeps (and π-pulses) of this chapter all stop at the resonant frequency $\omega_{54\to55}$. Continuation of the sweeping or pulsing does not enhance the probability of exciting the electron past level $n = 50$, but it does allow time for dissipation to destroy the excitation. Setting these parameters experimentally will be an iterative process of refining the cyclotron frequency measurement and readjusting the parameters. Fortunately, calculated excitation probabilities are not very sensitive to these detection-threshold and frequency-stop parameters.

5.2 Predicted Cyclotron Resonance Curves

The desired 1 ppb frequency resolution can only be achieved with a sufficiently small Rabi frequency. Fig. 5.1a demonstrates the frequency resolution. For several Rabi frequencies, the probability to excite above $n = 50$ by adiabatic passage is plotted

versus the starting frequency of the drive. While the smaller Rabi frequencies provide better frequency resolution, they also impose longer duration adiabatic passage times during which damping can play a role. The lowest Rabi frequency curves, therefore, have very small probabilities for excitation above $n = 50$.

The π-pulse excitation process is faster and thus allows less spontaneous emission. Excitations above $n = 50$ are therefore more likely (Fig. 5.1b). The frequency scale of Fig. 5.1b is extended due to the more complicated resonance structure, however, these curves indicate the possibility of ppb resolution as well. For small Rabi frequency (see $\Omega_R/\delta = 0.2$) a multiple peak structure emerges. This structure arises because beginning the pulse sequence one δ above the first transition frequency results in the second pulse being resonant (although the duration is slightly off) and so on. For higher Rabi frequencies, these multiple peaks overlap and the resonances become much broader than the corresponding adiabatic passage resonances. Thus the π-pulse method is really most useful for the lowest Rabi frequencies (and the highest resolution).

The resonance curves shown in Fig. 5.1 were all calculated with zero temperature. Including a 4.2 K temperature and a Boltzmann distribution of initial occupied Landau levels did not appreciably alter the shapes, but did slightly reduce excitation probabilities.

The resonance curves shown in Fig. 5.1 were also produced assuming that an instantaneous detection of the cyclotron excitation is possible. While fast "in-the-dark" axial frequency detection methods have been demonstrated [18, 19] a simpler approach may be possible. Fig. 5.2a shows the adiabatic resonance curves of Fig. 5.1a with a power increase to $\Omega_R/\delta = 21$ at the end of the sweep. This strong drive decreases the loss-rate to less than $0.001\gamma_c$ (see Fig. 4.8) so there is ample time for axial frequency detection. The power increase does not appreciably alter

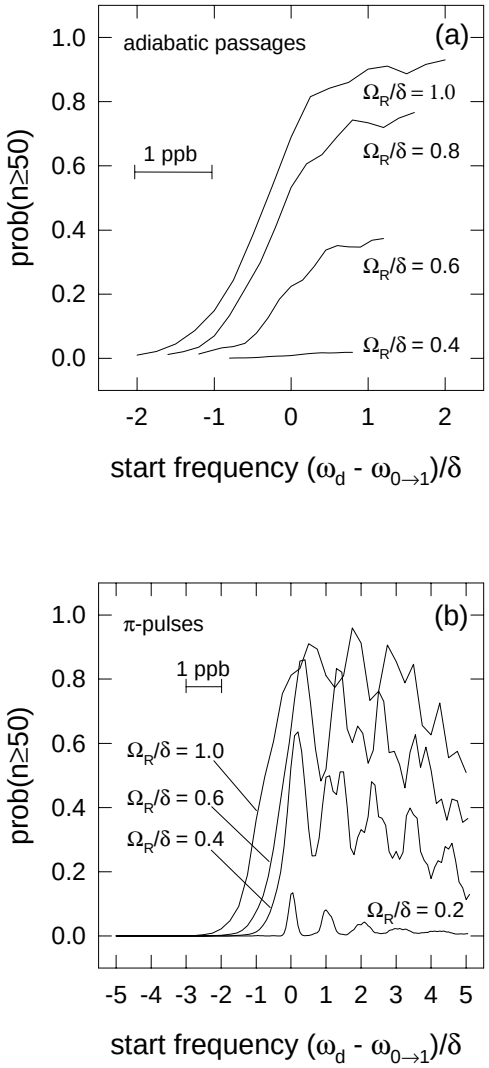

Figure 5.1: Probability of exciting above $n = 50$ by adiabatic passage ($\Gamma_{\rm LZ} = 1$) in (a), and by a series of π-pulses in (b), for 4 different drive strengths. Excitation probabilities are calculated with zero temperature, weak drive ($\Omega_R/\delta \leq 1$), and inhibited spontaneous emission ($\gamma_c/\gamma_{\rm fs} = 0.1$). Part-per-billion cyclotron frequency resolution and accuracy are attainable for these small Rabi frequencies.

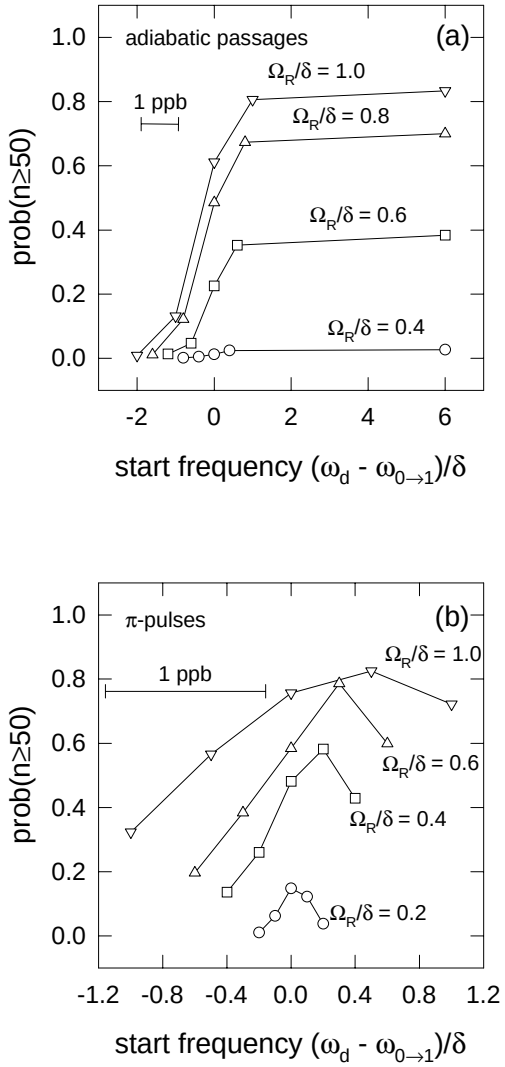

Figure 5.2: Same resonance curves as in Fig. 5.1, but with an increase of the Rabi frequency to $\Omega_R/\delta = 21$ upon completion of the excitation process.

the frequency resolution of the resonance curves, so a 1 ppb resolution cyclotron frequency measurement should be possible and detectable. A similar check on pulsed excitations (Fig. 5.2b) shows that the first resonant peaks of Fig. 5.1b maintain their high resolution as well.

It has been suggested to try sensing the $n = 0 \rightarrow 1$ transition frequency with a single resonant low-power π-pulse, followed by a higher-power adiabatic detection sweep. A weak 'sense' pulse would probe the $n = 0 \rightarrow 1$ transition with high resolution, and the higher power adiabatic sweep would quickly detect whether the transition was made. In this way, the entire process would be completed in much less than a spontaneous emission time. This technique relies on the ability of the high power adiabatic sweep to transfer the electron from the $n = 1$ state back to the ground state and subsequently not induce a large detectable excitation, if the sense pulse was effective. Very strong adiabatic passage drives ($\Omega_R/\delta \gg 1$), however, were just as effective at inducing large excitations from $n = 1$ as from $n = 0$. Thus, this technique is only viable for adiabatic detection drives whose Rabi frequencies are on the order of or less than δ, but then hope of easily beating spontaneous emission must be disregarded. There is still an advantage to being able to 'sense' with a very weak driving force and then 'detect' with a $\Omega_R/\delta \sim 1$ adiabatic fast passage, and that is having the ability to obtain the resolution determined by the sense pulse in the amount of time determined by the detection sweep.

Since the low Rabi frequency excitation probabilities are very sensitive to dissipation, a separate study was performed to characterize maximum excitation probability as a function of Rabi frequency for different damping rates. The stability condition $\frac{\Omega_R/\delta}{\sqrt{n}} \gg 1$ can not be met for these small Rabi frequencies, which is why a portion of the excitation is lost. Still, the loss-rate is proportional to the cyclotron damping rate, so inhibiting spontaneous emission in the Penning trap cavity reduces

the amount of loss for these slow excitations. An inhibited rate of $\gamma_c/\gamma_{\rm fs} = 0.3$ in a Penning trap has been experimentally measured [17], while the rate of $\gamma_c/\gamma_{\rm fs} = 0.1$ used in Figs. 5.1 and 5.2 should be attainable as well.

Figs. 5.3a and 5.3b show the probabilities for adiabatic sweeps from above resonance to excite the electron past $n = 50$ using three representative synchrotron radiation rates: $\gamma_c/\gamma_{\rm fs} = 0.1$, 0.3, and 1. For adiabatic conditions (Fig. 5.3), lower damping rates and higher drive powers clearly result in less loss during the excitation process. In 5.3a an adiabatic Landau-Zener parameter of 1 is taken whereas in 5.3b a less adiabatic Landau-Zener parameter of 0.25 is used. Both $\Gamma_{\rm LZ}$ choices are reported in order to illustrate those cases where it is advantageous to give up adiabaticity in favor of beating spontaneous emission ($\Omega_R/\delta = 0.6$, $\gamma_c/\gamma_{\rm fs} = 0.1$ for example). Such plots help quantify the expected dependencies and should be useful for experimentally choosing favorable sets of sweep, damping, and drive power parameters.

Similar maximum probability curves for the π-pulse method are shown in Fig. 5.4. The higher probabilities achieved reflect the faster nature of this method in the presence of damping. Start-frequencies for these pulse sequences are chosen to correspond to the ground state transition peaks of Fig. 5.1b.

In summary, ppb cyclotron frequency resolution and accuracy should be possible by starting excitation π-pulses or adiabatic passages at different frequencies and measuring the probability of excitation for each. Small Rabi frequencies are needed for the highest resolution, but the slower sweep speed requirement allows spontaneous emission more time to destroy the signal. Damping should thus be minimized as much as is experimentally possible. Resonance curves are not compromised by including a 4.2 K black-body temperature, or by increasing the Rabi frequency at the end of a sweep to make the excitation persist for detection.

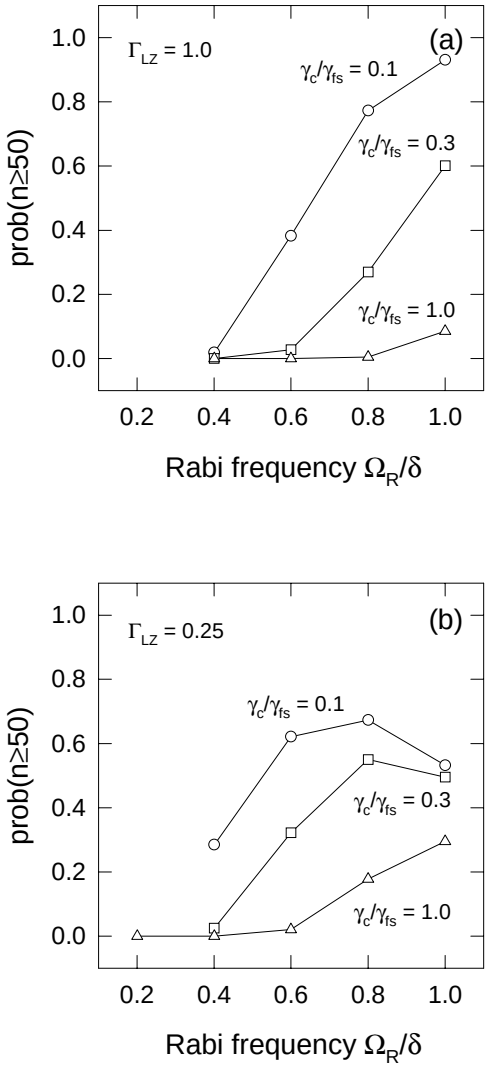

Figure 5.3: Probability of exciting above $n = 50$ by adiabatic passage ($\Gamma_{\rm LZ} = 1$) in (a), and by less adiabatic sweeps ($\Gamma_{\rm LZ} = 0.25$) in (b) for 3 different synchrotron radiation rates and as a function of Rabi frequency. Lower damping rates and faster sweep speeds increase the likelihood of obtaining an excitation.

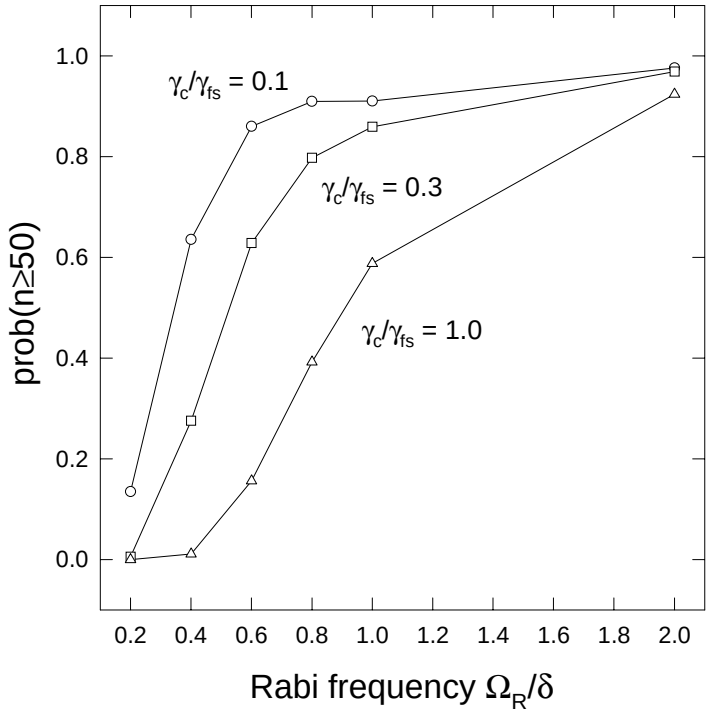

Figure 5.4: Probability of exciting above $n = 50$ versus Rabi Frequency as in Fig. 5.3 but for π-pulse excitation sequences. Again, lower damping rates and the shorter durations of high power pulse sequences increase the likelihood of obtaining an excitation. Start-frequencies for these pulse series are chosen to correspond to the ground state transition peaks of Fig. 5.1b.

Chapter 6

Stochastic Fluctuations in the Cyclotron Frequency

So far we have analyzed a driven one-electron cyclotron oscillator, including relativistic anharmonicity, and synchrotron radiation damping to equilibrium with a black-body background. The experimentally realizable system differs most notably in that special relativity also couples the energy in the electron's axial motion to the cyclotron frequency. This coupling produces "noise" on the cyclotron frequency (or equivalently "noise" on the drive frequency). Phase-noise on the microwave driving field has similar consequences. We turn now to consider the influence of axial noise. First, we express the cyclotron frequency shift as a function of axial amplitude. Next, we generate axial amplitude noise (the subject of Sec. 6.1). Finally, in Sec. 6.2, we illustrate the effect of such noise on cyclotron resonance curves and adiabatic sweeps.

The relativistically shifted resonant cyclotron frequency discussed in Ch. 2 is

$$\omega = \frac{eB}{\gamma mc} = \frac{\omega_c}{\gamma}, \tag{6.1}$$

where $\gamma = 1/\sqrt{1 - \left(\frac{\mathbf{v}}{c}\right)^2}$ is the usual relativistic factor. Solving the Dirac equation [15] gives the 1st order correction to the resonant cyclotron frequency, due to the axial energy E_z,

$$\frac{\Delta\omega}{\omega_c} = -\frac{E_z}{2mc^2}. \tag{6.2}$$

where $\Delta\omega$ is the relativistic shift $\Delta\omega = \omega - \omega_c$. The axial oscillation is brought to thermal equilibrium with a 4.2 K detection circuit through resistive damping at a typical rate of $\gamma_z^{-1} = 30$ ms. At this temperature, the average axial Landau excitation is $n_z \simeq 1000$, and the motion can be treated as a classical harmonic oscillator, with response amplitude $z \sim e^{i\omega_z t}$ and energy

$$E_z = \frac{1}{2}m\omega_z^2 z^2 + \frac{1}{2}m\dot{z}^2 = m\omega_z^2|z|^2. \tag{6.3}$$

We scale the axial amplitude squared dependence to its time average, given by the equipartition theorem

$$\frac{1}{2}m\omega_z^2\langle z^2\rangle = \frac{1}{2}kT_z, \tag{6.4}$$

where the axial temperature T_z is differentiated from the cavity temperature T. The cyclotron frequency shift is then

$$\Delta\omega = -\frac{1}{2}\frac{kT_z}{\hbar\omega_c}\frac{|z|^2}{\langle z^2\rangle}\delta, \tag{6.5}$$

where $\delta = \omega_c(\hbar\omega_c/mc^2)$ is the anharmonic shift per energy level.

As the axial response z fluctuates due to Johnson noise from the resistive detector, the cyclotron $n = 0 \rightarrow 1$ transition frequency fluctuates as well. The first order effect of such frequency noise is to convolve the predicted resonance curves found in Ch. 5 with a Boltzmann exponential distribution of expected cyclotron frequency

shifts. At 4.2 K, however, the average shift $\langle \Delta\omega \rangle \simeq -\frac{1}{3}\delta$ is close enough to the one δ spacing to suggest a significant impact on both adiabatic passage and π-pulse excitations. The effect may be particularly important if axial temperatures higher than 4.2 K are imposed by a hot detector. In this chapter we show how to represent the thermal noise as a stochastically changing cyclotron frequency, and then give one example of its effect on adiabatic fast passages and possible ppb cyclotron frequency measurements.

6.1 Axial Motion Driven by Noise

The axial equation of motion is that of a simple harmonic oscillator

$$\ddot{z} + \gamma_z \dot{z} + \omega_z^2 z = n(t) \tag{6.6}$$

where $n(t)$ is Gaussian white noise whose amplitude must be adjusted so that the axial response satisfies the equipartition theorem. In the end, the generated response amplitudes can be scaled by a ratio of the actual rms amplitude to the generated rms amplitude, so the original size of the noise drive is unimportant. The fast 60 MHz oscillation is removed by going to the oscillating frame $z = \bar{z}e^{i\omega_z t}$ where $\bar{z}$ is assumed to be slowly varying. The equation of motion for $\bar{z}$ is then

$$\ddot{\bar{z}} + \dot{\bar{z}}(2i\omega_z + \gamma_z) + \bar{z}(i\omega_z\gamma_z) = n(t)e^{i\omega_z t}. \tag{6.7}$$

For slowly varying $\bar{z}$, $|\ddot{\bar{z}}| \ll |\dot{\bar{z}}\omega_z|$ and $|\dot{\bar{z}}\gamma_z| \ll |\bar{z}\omega_z\gamma_z|$, the equation of motion becomes

$$\dot{\bar{z}} + \frac{\gamma_z}{2}\bar{z} = \frac{n(t)e^{i\omega_z t}}{2i\omega_z}. \tag{6.8}$$

Since white noise has equal power density at all frequencies, the right hand side of Eq. 6.8 is just another arbitrary white noise source $n_2(t)$ (or alternatively can be thought of as 60 MHz white noise mixed down to the low resonant frequencies of $\bar{z}$), and the oscillating frame equation of motion reduces to

$$\dot{\bar{z}} + \frac{\gamma_z}{2}\bar{z} = n_2(t). \tag{6.9}$$

Thus, as intuition suggests, the axial response is just that of white noise filtered with a time constant $RC = 2\tau_z = 2/\gamma_z$.

Eq. 6.9 is solved to generate a time series of axial energies which can be used in the adiabatic cyclotron sweep computation. At each of 300 equally spaced intervals per time $2\tau_z$, the noise driving amplitude is changed randomly to fit a Gaussian profile. Fig. 6.1 shows plots which characterize this noise drive and the axial response. A time series of random drive amplitudes spanning 10 $2\tau_z$ times is shown in (a). The Fourier transform (squared) of this time series, in (b), illustrates the flat white-noise energy spectral density out to a frequency determined by the minimum time step. Fig. 6.1c shows the "filtered" energy spectral density of the axial response to such a drive, and for comparison, Fig. 6.1d shows the energy spectral density of a pure exponential decay (no noise drive). All angular frequency axes in Fig. 6.1 are scaled by $\gamma_z/2$. The axial response time series used to produce the spectral densities of (c) and (d) are extended to span 1000 and 100 $2\tau_z$ times, respectively, in order to achieve high enough resolution for the figures.

These spectral densities provide an intuitive explanation of how the axial oscillator filters the broad-band Johnson noise. The broad-band noise in (b) is filtered to a narrow bandwidth of γ_z in (c). From this observation, we are assured that the choice of step-size for the Johnson noise becomes irrelevant once the step-size

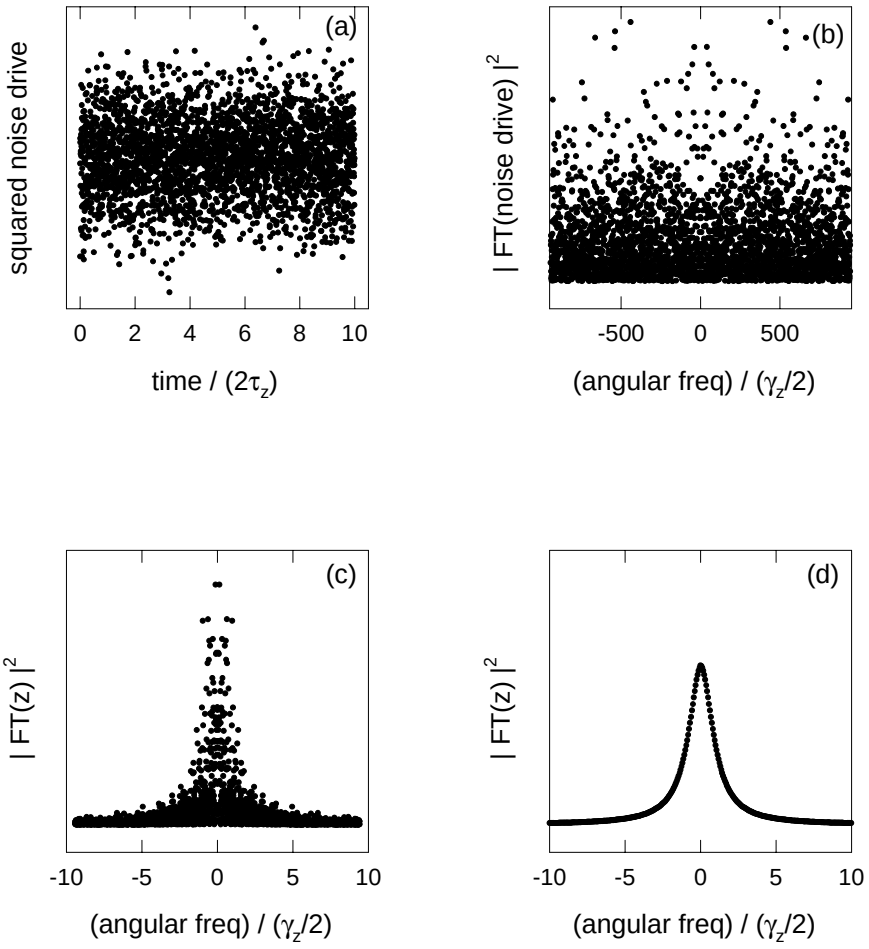

Figure 6.1: (a) A time series of Gaussian white noise amplitudes spanning 10 $2\tau_z$ times. (b) The Fourier transform (squared) of this time series. (c) A Fourier transform (squared) "filtered" axial response to a similar noise series (spanning 1000 $2\tau_z$ times). (d) Another Fourier transform (squared) axial response, but undriven. When no noise drive is included, the exponential time response has a Lorentzian energy spectral density. All plots show 3000 points, and all noise drives are represented by 300 random amplitudes per time $2\tau_z$.

is much smaller than an axial damping time. Smaller steps serve to increase the bandwidth of the driving noise, but since the axial oscillator filters it anyhow, this is unnecessary. We generate 300 points per $2\tau_z$ so that the unfiltered white noise source extends well into the outer wings of the "filtered" Lorentzian tail. (The "filtered" Lorentzian spectral shape can be derived by Fourier transforming Eq. 6.9. The undriven spectral density in (d) confirms this expected shape by fitting well to a Lorentzian with half-width $\gamma_z/2$.)

Fig. 6.2 shows additional properties of the computed axial energies. Fig. 6.2a shows a running average of energies for an extended time series spanning 100,000 τ_z times. The final value is used to scale the data set of response energies. Finally, a histogram of energies generated from another extended run spanning 2000 τ_z times is shown in Fig. 6.2b. The expected Boltzmann exponential shape emerges.

6.2 Adiabatic Passage with Noise: An Example

The fluctuating axial amplitude makes the effective cyclotron resonant frequency vary stochastically in time because of the relativistic coupling in Eq. 6.5. The noise is characterized by the axial temperature T_z (which gives the magnitude of the frequency shift), and the axial damping time τ_z (which gives the time-scale or bandwidth of the noise). These two parameters are varied to determine the cyclotron oscillator's sensitivity to them. Phase-noise in the microwave driving field can also be understood insofar as it can be described by these two parameters.

Noise effects in this section are illustrated using one representative set of adiabatic sweep parameters which we have shown should allow for 1 ppb resolution of the cyclotron frequency: $\Omega_R/\delta = 1$, $\gamma_c/\gamma_{\rm fs} = 0.1$, and $\Gamma_{\rm LZ} = 1$. The time dependent cyclotron frequency is easily incorporated into the master equation calculation, but

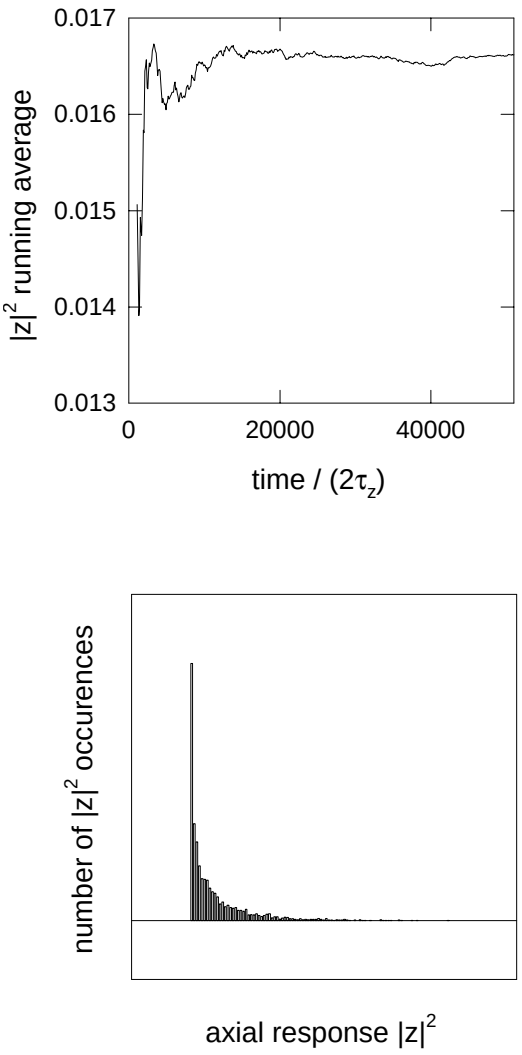

Figure 6.2: (a) Running average of axial amplitude squared, driven by noise. (b) Histogram of 3000 noise driven axial amplitudes squared, sampled over 1000 $2\tau_z$ times. For both, 300 drive noise points are generated per $2\tau_z$ time.

now repeated trials must be averaged. A set of 10 such trials, in Fig. 6.3a, shows that the noise typically decreases and delays the probability to excite the cyclotron oscillator above $n = 50$. Plotted are excitation probabilities as a function of time for adiabatic frequency sweeps starting far above resonance. The top curve is an adiabatic passage without noise, taken from the last chapter. The other curves are adiabatic passages for ten different sets of stochastic axial noise using $T_z = 4.2$ K and $\tau_z = 30$ ms.

Not surprisingly, the cyclotron excitation is affected less when the noise is more heavily filtered by increasing the axial damping time. Fig. 6.3b illustrates this with a set of excitations which use a slower axial damping time of $\tau_z = 300$ ms. Fortunately the axial damping time can be experimentally adjusted by de-tuning the axial frequency from the detection circuit. This does make detection more difficult, but it should be possible to de-tune the axial oscillator during the sensitive adiabatic cyclotron sweep and then re-tune it for detection after the Rabi frequency has been increased for stability.

Fig. 6.4 explores the dependence of the cyclotron excitation probability on temperature as well as further exploring the dependence on axial damping time. Each point represents the final excitation probability averaged together for ten trials such as those shown in Fig. 6.3. The same ten sets of noise data are used for each point in Fig. 6.4. "Error" bars extend plus or minus one standard deviation of the mean or $\sigma/\sqrt{10}$. With only ten samples, we caution that the "error" bars are not very reliable. Still, the dependences are clear.

The temperature sensitivity is probed by fixing the axial damping time at $\tau_z = 30$ ms and varying T_z. Fig. 6.4a demonstrates that cooling the axial temperature to 1 K would eliminate the effect of axial noise for these sweep parameters. Electrons have recently been trapped in a dilution refrigerator cooled Penning trap at 50 mK

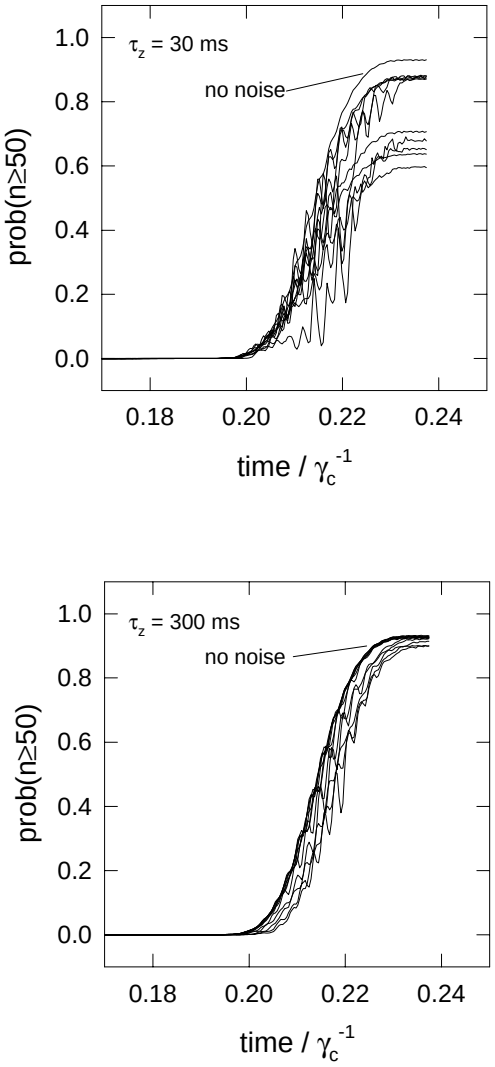

Figure 6.3: Probability of exciting above $n = 50$ by adiabatic passage starting far above resonance, without noise (labeled) and with 10 different sets of axial noise coupled to the cyclotron frequency. For a 4.2 K axial temperature (both), a faster axial damping time of $\tau_z = 30$ ms (a) has a more detrimental effect on the excitation than a slower axial damping time of $\tau_z = 300$ ms (b). Spontaneous emission rate is $\gamma_c/\gamma_{\rm fs} = 0.1$.

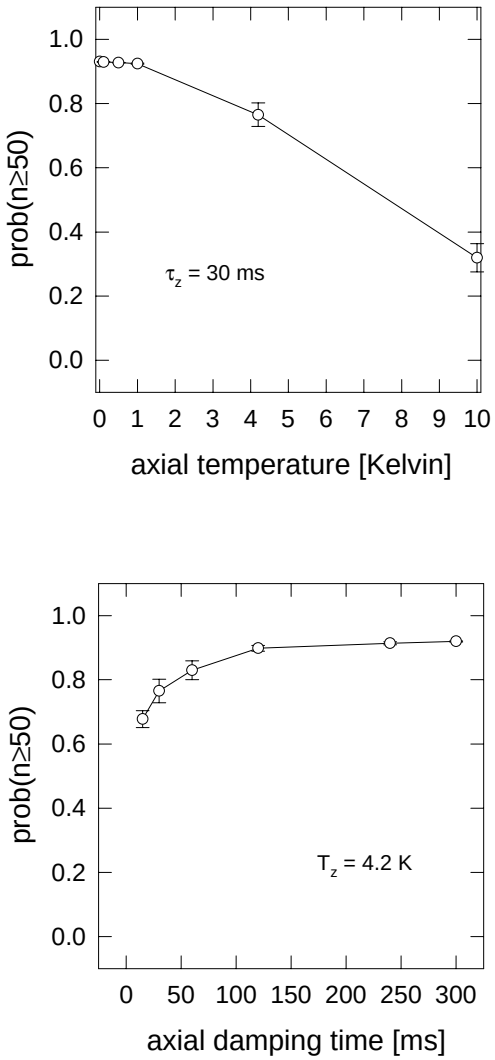

Figure 6.4: Probability of exciting above $n = 50$ by adiabatic passage, with a a stochastically changing cyclotron frequency, as a function of axial temperature (for $\tau_z = 30$ ms) in (a), and as a function of axial damping time (for $T_z = 4.2$ K) in (b). Each point represents an average of 10 noisy sweeps such as found in Fig. 6.3. "Error" bars extend plus or minus one standard deviation of this mean (points without error bars have standard deviations smaller than the point size). Spontaneous emission rate is $\gamma_c/\gamma_{\rm fs} = 0.1$.

[35]. It should alternatively be possible to cool the axial temperature at least 1000 times below the traditional 4.2 K environment using cavity sideband cooling [13], after decoupling the axial motion from the detection circuit. For operation at 4.2 K, however, Fig. 6.4b demonstrates that narrowing the noise bandwidth can also reduce its influence. The adiabatic passage excitation probability is not significantly reduced for axial damping times slower than 100 ms.

As a final check of the axial noise's influence under typical $T_z = 4.2$ K, $\tau_z = 30$ ms conditions, an entire resonance curve is generated by starting adiabatic sweeps at different frequencies. Fig. 6.5 shows a comparison of this resonance curve with the noise-free case from last chapter. Again, each of the noise affected excitation probabilities are an average of ten trials. New noise sequences are used for each start frequency, in an effort to simulate the constantly changing axial energy that would be encountered in an experimental measurement. The computed resonance is still encouraging for obtaining ppb frequency measurements. The maximum probability is reduced by 20% and the midpoint of the transition is shifted an amount consistent with the expected $-\frac{1}{3}\delta$. Remember, however, that this resonance curve represents a sweep with $\Omega_R/\delta = 1$. A 20% reduction in excitation probability may be more detrimental for the lower Rabi frequencies.

In summary, the noise analysis shows that it is extremely beneficial to cool and/or reduce the bandwidth of the axial noise, even if only slightly. Without cooling below 4.2 K or increasing the axial time constant above $\tau_z = 30$ ms, however, 1 ppb cyclotron frequency resolution should still be possible.

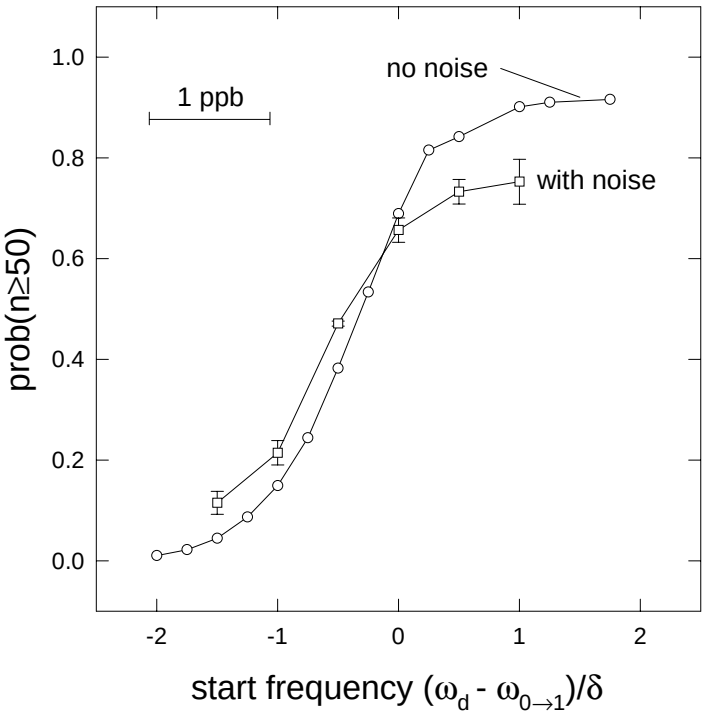

Figure 6.5: Probability of exciting above $n = 50$ by adiabatic passage, as a function of start frequency (as in Fig. 5.1a), both with and without 4.2 K, 30 ms, axial noise (as labeled). Rabi frequency is $\Omega_R/\delta = 1$, Landau-Zener parameter is $\Gamma_{\rm LZ} = 1$, and damping rate is $\gamma_c/\gamma_{\rm fs} = 0.1$.

Chapter 7

Conclusions and Future

The one-electron relativistic cyclotron oscillator is a rich quantum mechanical system useful for modeling a certain class of nonlinear oscillators. Solving the master equation, with a driving force incorporated, completes the mission of describing physical nonlinear oscillators, begun by those such as Milburn [3–5, 22–25]. Interesting loss and revival features are quite different when a drive is present, and the stability of resonantly driven excitations are characterized. The master equation calculation is complemented by a Monte Carlo wave-function calculation, the method being generalized from the published two/three state procedure [29]. The equivalence of the 2 methods is shown both analytically and numerically. Future work can, therefore, probe the nature of individual trials.

Q-functions for dressed coherent states of the anharmonic oscillator are calculated. Perturbations to these states exhibit revivals in the absence of a drive and partial revivals in the presence of a drive. Phasewidth oscillations are seen at a frequency determined by the n-level Rabi frequency $\Omega_n = \Omega_R\sqrt{n}$ and the anharmonicity δ. Higher Rabi frequencies allow less spreading time and result in more stable excitations as described below.

The scaled phasewidth squared is shown to be a universal parameter which characterizes loss from a dressed excited state. Most surprising is the failure of the notion that cyclotron excitation above a certain "classical" level remains stably excited. For a large excitation, quantum uncertainty introduces a large spread in energy levels, each of which rotate at a different frequency. Differential rotation leads to angular spreading away from the stable phase-space attractor, and loss occurs at a rate proportional to (but most often quite different from) the cyclotron damping rate. Although the classical model is generally thought to predict stability for driven excitations, a distribution of phase-space points corresponding to the quantum distribution is also shown to be classically unstable for such a large anharmonicity-to-damping ratio oscillator. More work is thus warranted to quantify the unstable effect of angular spreading in the classical phase-space 'bucket' picture.

Implications for ppb cyclotron frequency measurements are as follows. Small Rabi frequencies are needed for high resolution, and the resulting large loss-rates require that the excitation be accomplished in a time much shorter than the radiative damping time. Although this is expected from simple arguments, our explicit calculation provides the quantitative information required to walk the narrow path between 1 ppb frequency resolution (suggesting a weak driving force) and the need to beat spontaneous emission (suggesting a strong driving force).

Inhibiting the cyclotron damping rate by a factor of ten from the free space rate makes it easier to beat spontaneous emission and successfully excite the electron. Such inhibition has been observed using resonant trap cavities [17], and now can be controlled in a cylindrical Penning trap [12–14]. While detuning the cyclotron frequency away from all cavity modes will inhibit radiation, it may make the task of getting microwave power into the Penning trap cavity more difficult. However, the microwave drive may also have more power than was previously thought, if the cur-

rently observed cyclotron excitations are being limited by the quantum fluctuation loss model rather than lack of drive power.

In addition to decreasing the synchrotron damping rate, minimizing the length of the excitation process also enhances the probability of a weak driving force successfully exciting the electron. Two of the many possible excitation schemes, adiabatic passages and π-pulse sequences, have been incorporated into the master equation to optimize the compromise between speed of excitation and cyclotron frequency resolution. Predicted resonance curves for a series of Rabi frequencies exhibit shifts less than 1 ppb. Although a small Rabi frequency is required during the early stages of excitation, increasing the power after the electron reaches the typical $n = 50$ threshold does not compromise the resonance curve. This raises the question of how early during the excitation process the Rabi frequency can be increased. Time varying drive strengths and/or sweep speeds would certainly be another way to minimize the excitation time and are worth investigating further.

Stochastic fluctuation of the cyclotron frequency, due to thermal excitations of the axial motion, has for the first time been included in adiabatic passage calculations. This effective "noise" is Johnson noise, filtered by the electron's damped axial motion. The amplitude of stochastic cyclotron frequency fluctuations is thus determined by the axial temperature, and the bandwidth by the axial damping rate. Adiabatic passage excitations are hindered by such noise at the temperatures (4.2 K) and damping times (30 ms) most often encountered experimentally. Quantitative knowledge of these sensitivities will enable experimenters to vary either or both of these axial parameters into a less destructive region. The cyclotron frequency fluctuation would, for example, be negligibly small for the 50 mK electrons recently observed [35].

The relativistic cyclotron oscillator is a useful system for the study of quantum

dissipation. Although the discovered quantum coherence and revival effects are too fast to be detected experimentally, they are found to have a large impact on the stability of an excitation. The oscillator differs from ordinary, classical anharmonic oscillators in its large anharmonicity-to-damping ratio, and thus exhibits behavior different from the intuitive classical expectation. Now that the ensemble average behavior is understood, the Monte Carlo wave-function calculation developed should be used to explore the effects of spontaneous emission and/or noise on individual realizations. If the measurement operators are chosen correctly, this may give a better picture of what happens during a single experimental frequency sweep. Future work should also include an analytical study of the revival time-scales, as the empirical dependencies uncovered may have simple explanations in a dressed state basis. In addition, a better classical understanding of the phase-space 'bucket' spiral structure is needed to provide more insight into the quantum mechanical phase spreading loss mechanism.

This rich quantum mechanical system has already been realized as a single trapped electron in a Penning trap [1, 18, 19]. The current study, along with recent experimental work characterizing the cylindrical Penning trap cavity [12, 14] and developing axial "in-the-dark" detection techniques [18, 19] sets the stage for ppb cyclotron frequency measurements and the next generation of $g-2$ measurements to test QED. Currently, the electron magnetic moment is measured to a fractional accuracy of 4 parts in 10^9 [10]. The master equation solutions will aid experimenters in choosing system and drive parameters which allow 1 ppb cyclotron frequency resolution and accuracy.

Solution of the master equation for the damped anharmonic oscillator reveals several unexpected features of oscillators whose anharmonic shifts are large compared to damping widths for the lowest n-levels, but still tiny compared to harmonic level

spacings. It is likely that behavior similar to that presented here may express itself in other quantum oscillators with anharmonicity in this regime. Our study can provide new insight into the detailed physics behind maintaining stable excitations in these driven, damped nonlinear oscillators.

Appendix A

Conventions and Detailed Evolution Equations

This chapter is intended for those who are interested in the exact conventions and equations used for the various computer codes, particularly those who will be continuing the theoretical work. In total, four separate codes were used to solve the time dependent anharmonic oscillator equations: two classical and two quantum mechanical. The classical codes have nearly identical algorithms, and differ mostly in the ease with which they calculate phase-space maps versus phase-space trajectories versus evolution of probability distributions. The two will be distinguished by the computer languages in which they were written: C for probability distribution evolution and maps, Fortran for trajectories and more easily extracted maps. (I am indebted to Adam Lupu-Sax for generously supplying the C code.) The quantum codes each use one of the two approaches discussed in the text: the master equation solution or the MCWF technique.

All four codes, with separate histories spanning 5 years, miraculously use the same drive phase convention $\phi_d(0) = \pi$. The classical theory discussed in the main

text assumes $\phi_d(0) = 0$, so all phase-space trajectories and maps shown, as well as the superimposed Q-function contour of Fig. 4.15, have been rotated by 180° from the actual output data. In addition, the classical C code and the master equation code both output phase space points (or Q-functions) in terms of the real and imaginary parts of $\bar{\alpha}$ (or α). The classical Fortran code, however, uses the velocity variables u_x and u_y, so the sign of the u_y variable must be switched to match phase-space plots of the other two codes and the theory of Sec. 2.1, since $u_x = \sqrt{2\hbar\omega_c/m}\, Re[\bar{\alpha}]$ and $u_y = -\sqrt{2\hbar\omega_c/m}\, Im[\bar{\alpha}]$ (from Eq. 2.7). Finally, both quantum codes and the classical C code scale time by δ^{-1}, but the classical Fortran code scales time by $(\gamma_c/2)^{-1}$.

Similarities and differences between conventions in the two quantum codes are summarized as follows. First, the Hamiltonians are defined slightly differently. The master equation method uses the same Hamiltonian $H_{\rm aho}$ as in Eq. 3.25,

$$H_{\rm aho} = \hbar(\omega_c - \frac{\delta}{2})a^\dagger a - \frac{1}{2}\hbar\delta(a^\dagger a)^2. \tag{A.1}$$

but the MCWF code originated as a simple wave-function Schrödinger evolution which was simplified so that the $n = 0 \rightarrow 1$ transition frequency was called ω_c rather than the $\omega_c - \delta$ described in the text (see Fig. 3.2). Thus the MCWF anharmonic Hamiltonian is actually

$$H_{\rm aho} = \hbar(\omega_c + \frac{\delta}{2})a^\dagger a - \frac{1}{2}\hbar\delta(a^\dagger a)^2. \tag{A.2}$$

Second, different drive offsets are defined in the two codes: the MCWF code defines $\epsilon(t) = \omega_c - \omega_d(t) = \omega_{0\rightarrow 1} - \omega_d(t)$ whereas the master equation code defines $\epsilon(t) = \omega_d(t) - \omega_c = \omega_d(t) - \omega_{0\rightarrow 1} - \delta$.

The energy eigenbasis formulation of the master equation, as defined in Eq. 3.32 for the density operator in a frame rotating at ω_c is

$$\begin{aligned}
\frac{d\bar{\sigma}_{kl}}{dt} &= \left\{\tilde{\kappa}_{kl} + \frac{i\delta}{2}[k(k+1) - l(l+1)]\right\}\bar{\sigma}_{kl} \\
&+ \sqrt{(k+1)(l+1)}(\bar{n}+1)\gamma_c\,\bar{\sigma}_{k+1,l+1} + \sqrt{kl}\bar{n}\,\gamma_c\,\bar{\sigma}_{k-1,l-1} \\
&+ \frac{\Omega_R}{2}e^{i\lambda}[\sqrt{l}\bar{\sigma}_{k,l-1} - \sqrt{k+1}\bar{\sigma}_{k+1,l}] \\
&+ \frac{\Omega_R}{2}e^{-i\lambda}[\sqrt{k}\bar{\sigma}_{k-1,l} - \sqrt{l+1}\bar{\sigma}_{k,l+1}], \qquad \text{(A.3)}
\end{aligned}$$

where $\lambda = \int_0^t \epsilon(t')dt' = \int_0^t \{\omega_d(t') - \omega_{0\to 1} - \delta\}dt'$, and $\tilde{\kappa}_{kl}$ describes the finite basis effects in terms of the minimum and maximum n-levels min and max and in terms of $\bar{\delta}_{ab}$ defined below,

$$\begin{aligned}
\tilde{\kappa}_{kl} &= -\frac{\gamma_c}{2}\left\{(k\bar{\delta}_{k,min} + l\bar{\delta}_{l,min})(\bar{n}+1) + [(k+1)\bar{\delta}_{k,max} + (l+1)\bar{\delta}_{l,max}]\bar{n}\right\} \qquad \text{(A.4)} \\
\bar{\delta}_{ab} &= \begin{cases} 0 \text{ if } a = b \\ 1 \text{ if } a \neq b \end{cases}. \qquad \text{(A.5)}
\end{aligned}$$

Some checks were performed in an interaction picture which takes the unperturbed Hamiltonian as $H_0 = H_{\text{aho}}$ of Eq. A.1, rather than as $H_0 = \hbar\omega_c a^\dagger a$ defined in the text. We informally refer to the original as the "rotating frame" and the later as the "interaction picture". In this language, the "interaction picture" corresponds to a different rotating frame for each Landau level. The density operator elements $\tilde{\sigma}_{kl}$ in this new "interaction picture" are related to the "rotating frame" density operator elements $\bar{\sigma}_{kl}$ by

$$\tilde{\sigma}_{kl} = \bar{\sigma}_{kl}e^{-i[(k(k+1)-l(l+1)]\frac{\delta}{2}t} \qquad \text{(A.6)}$$

This completes the energy eigenbasis formulation of the master equation.

The MCWF evolution consists of two processes: the standard Schrödinger evolution, and the collapse. Schrödinger evolution is controlled by the effective Hamiltonian $H_{\rm eff} = H_{\rm aho} + H_{\rm drive} - i\hbar\frac{\gamma_c}{2}[(\bar{n}+1)a^\dagger a + \bar{n}aa^\dagger]$, where $H_{\rm aho}$ is defined by Eq. A.2, and $H_{\rm drive}$ is define as in the main text. The state vector is written as

$$|\Psi(t)\rangle = \sum_{n=min}^{max} C_n(t)|n\rangle = \sum_{n=min}^{max} D_n(t)e^{-i\omega_n t}|n\rangle, \tag{A.7}$$

where $\omega_n = (\omega_c + \frac{\delta}{2})n - \frac{1}{2}\delta n^2$ is defined by

$$H_{\rm aho}|n\rangle = \hbar\omega_n|n\rangle. \tag{A.8}$$

Then the Schrödinger equation $i\hbar(\partial/\partial t)|\Psi(t)\rangle = H_{\rm eff}|\Psi(t)\rangle$ gives the equation of motion for the wave-function coefficients

$$\begin{aligned} \dot{D}_n &= \frac{\Omega_R}{2}\left\{D_{n-1}\sqrt{n}e^{-i\delta(n-1)t+i\lambda} - D_{n+1}\sqrt{n+1}e^{i\delta nt-i\lambda}\right\} \\ &- \frac{\gamma_c}{2}(\bar{n}+1)\,D_n\,n\,\bar{\delta}_{n,min} - \frac{\gamma_c}{2}\,\bar{n}\,D_n\,(n+1)\,\bar{\delta}_{n,max} \end{aligned} \tag{A.9}$$

where $\lambda = \int_0^t \epsilon(t')dt' = \int_0^t\{\omega_{0\to1} - \omega_d(t')\}dt'$.

The coefficients after a collapse, but before renormalization, as determined by the measurement operators $\sqrt{\gamma_c dt(\bar{n}+1)}\,a$ and $\sqrt{\gamma_c dt\,\bar{n}}\,a^\dagger$, are

$$\text{Emission} \;:\; D_n(t+dt) = \sqrt{\gamma_c(\bar{n}+1)dt}\,D_{n+1}(t)\,\sqrt{n+1}\,e^{i\delta nt}\,\bar{\delta}_{n,max} \tag{A.10}$$

$$\text{Absorption} \;:\; D_n(t+dt) = \sqrt{\gamma_c\bar{n}dt}\,D_{n-1}(t)\,\sqrt{n}\,e^{-i\delta(n-1)t}\,\bar{\delta}_{n,min} \tag{A.11}$$

up to an overall phase. The collapse probability for each path is given by the sum of these new wave-function coefficients squared. This completes the wave-function evolution formulation.

Bibliography

[1] G. Gabrielse, H. Dehmelt, and W. Kells, Phys. Rev. Lett. **54**, 537 (1985).

[2] G. Milburn, Phys. Rev. A **33**, 674 (1986).

[3] G. Milburn and C. Holmes, Phys. Rev. Lett. **56**, 2237 (1986).

[4] V. Perinova and A. Luks, Phys. Rev. A **41**, 414 (1990).

[5] D. Daniel and G. Milburn, Phys. Rev. A **39**, 4628 (1989).

[6] B. Yurke and D. Stoler, Phys. Rev. Lett. **57**, 13 (1986).

[7] M. Mallalieu and C. R. Stroud Jr. , Phys. Rev. A **51**, 1827 (1995).

[8] M. Mallalieu and C. R. Stroud Jr. , Phys. Rev. A **49**, 2329 (1994).

[9] Z. D. Gaeta and C. R. Stroud Jr. , Phys. Rev. A **42**, 6308 (1990).

[10] R. S. Van Dyck Jr. , P. B. Schwinberg, and H. G. Dehmelt, Phys. Rev. Lett. **59**, 26 (1987).

[11] R. S. Van Dyck Jr. , P. B. Schwinberg, and H. G. Dehmelt, in *The Electron*, edited by D. Hestenes and A. Weingartshofer (Kluwer Academic Publishers, Netherlands, 1991), p. 239.

[12] J. Tan and G. Gabrielse, Phys. Rev. Lett. **67**, 3090 (1991).

[13] G. Gabrielse and J. Tan, in *Cavity Quantum Electrodynamics*, edited by P. Berman (Academic Press, New York, 1994), p. 267.

[14] J. Tan, Ph.D. thesis, Harvard University, 1992.

[15] L. Brown and G. Gabrielse, Rev. Mod. Phys. **58**, 233 (1986).

[16] I. I. Rabi, Z. f.Physik **47**, 507 (1928).

[17] G. Gabrielse and H. Dehmelt, Phys. Rev. Lett. **55**, 67 (1985).

[18] C. H. Tseng and G. Gabrielse, Appl. Phys. B **60**, 95 (1995).

[19] C. H. Tseng, Ph.D. thesis, Harvard University, 1995.

[20] Z. D. Gaeta, M. W. Noel, and C. R. Stroud Jr. , Phys. Rev. Lett. **73**, 636 (1994).

[21] C. Zener, Proc. R. Soc. London Ser. **A137**, 696 (1932).

[22] F. Haake, H. Risken, C. Savage, and D. Walls, Phys. Rev. A **34**, 3969 (1986).

[23] G. Milburn and D. Walls, Am. J. Phys. **51**, 1134 (1983).

[24] H. G. Oh, H. R. Lee, and T. F. George, Phys. Rev. A **39**, 5515 (1989).

[25] S. Chaturvedi and V. Srinivasan, J. of Mod. Opt. **38**, 777 (1991).

[26] W. Louisell, *Quantum Statistical Properties of Radiation* (John Wiley and Sons, New York, 1973).

[27] C. Cohen-Tannoudji, J. Dupont-Roc, and G. Grynberg, *Atom-Photon Interactions: Basic Processes and Applications* (John Wiley and Sons, New York, 1992).

[28] W. Press, B. Flannery, S. Teukolsky, and W. Vetterling, *Numerical Recipes in Fortran, Second Edition* (Cambridge University Press, New York, 1988).

[29] J. Dalibard, Y. Castin, and K. Mølmer, Phys. Rev. Lett. **68**, 580 (1992).

[30] K. Mølmer, Y. Castin, and J. Dalibard, J. Opt. Soc. Am. B **10**, 524 (1993).

[31] C. W. Gardiner, A. S. Parkins, and P. Zoller, Phys. Rev. A **46**, 4363 (1992).

[32] R. Dum, A. S. Parkins, P. Zoller, and C. W. Gardiner, Phys. Rev. A **46**, 4382 (1992).

[33] C. Cohen-Tannoudji, in *Frontiers in Laser Spectroscopy: Les Houches Session XXVII*, edited by R. Balian, S. Haroche, and S. Liberman (North-Holland Publishing Company, New York, 1977), session XXVII.

[34] R. Dum, P. Zoller, and H. Ritsch, Phys. Rev. A **45**, 4879 (1992).

[35] S. Peil and G. Gabrielse, private communication.